sciendo

Slovak Journal of Civil Engineering

Vol. 30, 2022, No. 1, 1 – 7
DOI: 10.2478/sjce-2022-0001

SPECIFIC DESIGN FEATURES OF PREFABRICATED FIRE-RESISTANT FLOOR SLABS MADE FROM LIGHTWEIGHT CONCRETE

Oleksandr KONOPLIANYK[1*], Nikolay KOTOV[1], Illia ILIEV[1]

Abstract

Reinforced concrete roof and floor structures have the highest heating temperatures and are exposed to the most difficult conditions during fires that occur in buildings and structures. The standardized fire resistance of hollow-core slabs made of heavy concrete from Portland cement is regulated as REI 45 or REI 60. The aim of the work is to develop a composition of lightweight fire-resistant concrete and architectural engineering for floor slab devices. The composition of lightweight fire-resistant concrete made from expanded clay aggregates and alumina cement was developed as a result of the work. The degree of fire resistance of the lightweight concrete composition with a bulk density of 1475 kg/m3 has been practically determined; i.e., REI 90. The structural solution of the floor slab has been improved; at the same time, we propose to develop a slab with a flat section made of lightweight fire-resistant concrete. Such floor slabs, along with an increase in the fire resistance limit, improve the heat-insulating ability of a floor due to a significant reduction in the coefficient of the thermal conductivity of lightweight concrete.

Address

[1*] Dept. of Construction Technology, Prydneprovska State Academy of Civil Engineering and Architecture, Dnipro, Ukraine

* ***Corresponding author:*** konoplianik.alexander@gmail.com

Key words

- Fire,
- Fire-resistant concrete,
- Floor slabs,
- Fire resistance limits.

1 INTRODUCTION

Significant damage to buildings and structures is caused by fires that periodically occur in buildings and structures. It is necessary to pay special attention to the correct determination of the actual fire resistance limit of the reinforced concrete structures used and to establish the possibility of the further operation of the structures after a fire, due to the constantly increasing number of fires.

Reinforced concrete roof and floor structures have the highest heating temperatures and are exposed to the most difficult conditions among all load-bearing structures. According to (DBN V.1.1-7-2002, 2002), for hollow-core slabs of buildings and structures of I-II degrees of fire resistance, the fire resistance limit is regulated as REI 45 or REI 60, which is significantly less than the limits for columns and walls in which the fire resistance limit is regulated as REI 120 – 150.

The value of the heating temperature of the concrete surface in the structure primarily depends on the temperature of the fire and on the location of the combustion site. When establishing the actual limit of fire resistance of reinforced concrete structures, it is necessary to know the intensity of the fire, since the normalized fire resistance of the structure will depend on the temperatures at which the combustion occurs and the duration of the fire.

2 SURVEY OF THE LITERATURE

According to (Milovanov, A. F., 1986), in the case of fires in residential and office buildings, the temperature on the premises rises to 1000-1100 ^{0}C with a fire duration of 1-2 hours. In industrial buildings, shops, and theater buildings, fires lasting 2-3 hours increase the temperature in the building to 1100-1200 ^{0}C.

According to (Yakovlev, A. I., 1985), the maximum temperatures that are reached during a fire are established according to a real regime of a “standard fire”. This temperature regime of a “standard fire” can be presented in the form of Tab. 1,

which determines the air temperature in °C for a certain duration of the fire.

Tab. 1 *Temperature values*

Time τ, min	Temperature t_6, °C
0	20
5	576
10	678
15	739
30	842
45	902
60	945
90	1006

In addition, the values of the maximum heating temperatures can be determined by the color of the concrete and some physical and mechanical effects of the material of structures (NIIŽB, 1987).

For the fire resistance limit of building structures, the duration in hours and minutes from the beginning of a standard fire test to the occurrence of one of the fire resistance limit states is considered the fire resistance limit of building structures. According to (DBN V.1.1-7-2002, 2002), building structures are classified according to their fire resistance and ability to spread fire.

The indicator of fire resistance is the fire resistance limit of a structure, which is determined by the duration (in minutes) from the start of the fire test according to the standard temperature regime to the onset of one of the limiting states of the structure:

- loss of bearing capacity (R);
- loss of integrity (E);
- loss of heat-insulating ability (I).

According to (Milovanov, A. F., 1986), integrity signs (E), which indicate the loss of a structure's ability to block the path of a fire, and the heat insulating ability (I), which indicates the loss of the ability to block the ignition of materials located on an unheated surface, do not require special consideration.

The characteristic of the bearing capacity (R), which indicates the degree of decrease in the strength characteristics of the structure, must be calculated according to (DSTU-N B EN 1992-1-2:2012, 2012) by zonal and tabular methods.

In addition to calculation methods for determining fire resistance, it is also necessary to consider the structural and technological requirements in relation to various reinforced concrete structures. When designing floor slabs according to (Phan, L. T. et al., (2010), it is necessary to consider the possible layer-by-layer explosive destruction of concrete, which can occur on a concrete surface from the flame side due to tensile stresses arising from the pressure of water in the pores, as well as from a decrease in the strength of the concrete after the loss of bound water.

An analysis of the literature on the effect of various factors on the fire resistance of structures leads us to believe that, along with the effect of high temperatures and the structural features of reinforced concrete elements, one of the factors that significantly affects the fire resistance of structures is the use of concrete component materials that have a high fire resistance.

3 MATERIALS AND METHODS

3.1 Consequences of a fire

Figs. 1-4 show the consequences of the damage to and destruction of hollow-core floor slabs in a room of a residential building during a fire that lasted for 35-40 minutes at a maximum temperature of 850 °C at the epicenter of the fire. The hollow-core floor slabs received significant damage, and their condition was assessed as unsuitable for normal use, although the maximum fire temperatures were not reached.

Fig. 1 *Two sections showing the complete destruction of the protective layer of concrete with a length of l = 2400 × 1360 mm and a width of a = 77 × 72 mm, respectively*

Fig. 2 *Explosive layer-by-layer destruction of the protective layer of concrete on the side of the flames. The through cracks in the concrete bridges between the voids have opening widths of a = 11.5 and 21.5 mm, respectively*

Fig. 3 *An area showing the falling off of the surface layer of the concrete (part of the concrete layer is hanging down), S_{area} = 0.32 m² (pink color of concrete). The crack in the protective layer of the concrete has a length of l = 1440 mm and a width of a = 2.6 mm*

Fig. 4 *Areas showing the destruction of the protective layer of the concrete, S_{area} = 0.04, 0.07 and 0.065 m², respectively, and the exposure of the working reinforcement (in the middle section, there are traces of soot on the reinforcement)*

As can be seen in Figs. 1-4, the floor slab underwent significant damage and destruction in the epicenter of the fire, where temperatures up to 850 °C occurred. As a result of the action of the flames and high temperatures, two sections of the slab were completely destroyed, i.e., the concrete collapsed, and through cracks appeared in the concrete lintels between the voids. At a distance from the epicenter of the fire, there are areas showing the falling off of the surface layer of the concrete with pink colored concrete and areas that expose the working reinforcement.

Such floor slabs need to be reinforced or replaced after exposure to a fire.

Our analysis of the consequences of the fire and destruction of the floor slabs allowed us to identify our main tasks, the implementation of which could lead to an increase in the normalized fire resistance of floor slabs. These tasks are:

1) The application of fire-resistant materials with a high degree of refractoriness for the manufacture of reinforced concrete structures;
2) Lightening the weight of floors, which will lead to an increase in their heat-insulating and sound-insulating capacity;
3) Improving the design of floor slabs.

1.2 Characteristics of lightweight fire-resistant concrete compositions and their test procedure

In our opinion, in order to increase the fire resistance and heat-insulating ability of concrete slabs, they should be made of lightweight fire-resistant concrete, the components of which are expanded clay, alumina cement, and water.

The choice of such components of the mixture is dictated primarily by the high fire resistance indicators of expanded clay and 26 mm alumina cement, namely, the refractoriness of expanded clay is 1000-1100 °C and that of alumina cement is 1480-1500 °C. In addition, alumina cement is able to harden when mixed with water without the presence of other active additives, due to the presence in its chemical composition of a significant amount of free oxide Al_2O_3.

The composition of the mixture components and their fractional composition are shown in Tab. 2, and their chemical composition is shown in Tab. 3.

Since the technical solutions for the compositions of lightweight fire-resistant concretes are new, and the copyright and intellectual property rights for these compositions belong to the authors, Tab. 2 does not list the content of the components of the concrete mixture.

As can be seen in Tab. 2, expanded clay aggregate is classified as light, since it has a poured bulk weight of 550 kg/m³, and its fractional composition is 1.25-20 mm. Alumina cement refers to powder additives, since it contains 83 % of a fraction less than 0.14 mm.

Tab. 3 indicates that silicon and aluminum oxides are the main chemical components that make up expanded clay, and its phase composition is mainly represented by aluminosilicates. Alumina cement is represented by aluminum and calcium oxides, and its phase composition is represented by calcium aluminates.

All the compositions of the lightweight fire-resistant concrete were made in the following order: first, the free-flowing components are thoroughly mixed for 2 minutes; then the resulting mixture and water are mixed for 2-3 minutes until a homogeneous mass is obtained.

The samples of the fire-resistant concrete were made by a vibration-compaction technique of mixtures on a laboratory vibrating platform. The air temperature was 18-20 °C, and the humidity reached 45-50 % during the manufacture and holding of the samples.

Tab. 2 *The composition of the components of the concrete mixture and their characteristics*

Component name	Poured Bulk Weight, kg/m³	Total residue in % in a sieve with a mesh size in the clear, mm								
		20	10	5	2.5	1.25	0.63	0.315	0.14	less 0.14
Expanded clay	550	6.0	63.8	22.2	5.0	3.0	-	-	-	-
Alumina cement	1200	-	-	-	-	-	-	3.2	13.8	83.0
Water	-	-	-	-	-	-	-	-	-	-

Tab. 3 *Chemical composition of lightweight fire-resistant concrete components*

Component names	Chemical composition, %						
	SiO_2	Al_2O_3	Fe_2O_3	CaO	MgO	$Na_2O + K_2O$	$\Delta m_{прк}$
Expanded clay	69.5	14.7	6.2	3.7	2.25	1.6	2.05
Alumina cement	3.5	45.0	13.4	36.8	0.3	0.5	0.5

The samples of the concrete mixes were kept for 24 hours before stripping. The concrete compositions on the alumina cement were kept for 4 days under normal conditions after stripping and then dried to a constant weight at a temperature of 105-110 °C.

The physical-mechanical and fire characteristics of the lightweight fire-resistant concrete were investigated. Its physical and mechanical characteristics included its volumetric weight, volumetric shrinkage, thermal conductivity coefficient, cubic and prismatic strength, and modulus of elasticity. These characteristics were determined after drying the samples to a constant weight. The fire characteristics included the strength of the samples and the integrity of the concrete after heating it at a temperature of 1000 °C for 90 min, as well as the thermal conductivity coefficient and bulk density after similar heating.

Concrete specimens with a size of 70 × 70 × 70 mm were produced to study their volumetric weight, shrinkage, and compressive strength. Prisms were produced with a cross-sectional size of 100 × 100 mm and a height of 400 mm to study the prismatic strength and elasticity modulus of the concrete. Samples with dimensions of 140 × 160 × 40 mm were produced to determine the thermal conductivity coefficient and assess the integrity of the concrete when exposed to high temperatures

The compressive strength of the concrete MPa was determined according to the normative document (DSTU B V.2.7. - 214: 2009, 2009) on samples dried to a constant weight. The samples were brought to failure on a 10-ton UMM-20 press with a load lifting speed of 10 kgf per second. The compressive strength was determined by the ratio of the breaking load to the cross-sectional area of the sample.

The volumetric shrinkage in percentages was determined by fixing the change in the volume of the samples according to the formula:

$$\varepsilon_v = \frac{V_2 - V_1}{V_1} \times 100 \qquad (1)$$

where V_1 was the initial volume of the sample after stripping;
V_2 was the volume of the sample after storage for a specified number of days and drying.

The shrinkage of the concrete samples was determined after drying them after they were stripped.

The thermal conductivity of the concrete after drying and heating to a temperature of 1000 ^{0}C (and subsequent cooling) was determined by a surface transducer in accordance with the source (DSTU B.V.2.7 - 41-95, 1995). Samples with dimensions of 140 × 160 × 40 mm were produced; they had smooth flat surfaces for placing the primary transducer and ensuring thermal contact between them.

To determine the prismatic strength and modulus of elasticity of the concrete, the nature of the dependence of the stresses on the concrete deformations was investigated when the prisms were loaded with a stepwise load (DSTU B.V.2.7 - 41-95, 1995). Dial indicators were installed on the four opposing faces of the prisms, and the prism was loaded with a load of 6.25 kN in stages on a P-125 press. The values of the indicators were recorded, and the average deformations of the concrete were determined after each stage of the loading. The load was brought to a destructive level.

The average elastic moduli, which were used in the calculations at loads that were 30 % of the destructive ones, were determined.

The compressive strength of the concrete after heating was determined in accordance with the source (DSTU B.V.2.7 – 217:2009, 2009). The samples were heated in an electric heating furnace to a temperature of 1000 ^{0}C according to the temperature rise mode in accordance with the normative document (GOST 20910-90, 1990). After heating to temperatures of 1000 ^{0}C, the samples were kept for 90 min and then cooled, together with the furnace.

To assess the integrity of the concrete, the samples were placed in a heated furnace in such a way as to provide one-sided heating of one of the surfaces. The temperature from the side of the heated surface was raised to 1000 ^{0}C according to the temperature rise mode in accordance with the normative document (Standard GOST 20910-90, 1990), and then the sample was kept at the given temperature for 90 min. Fig. 5 shows a general view of the furnace and the sample after the one-sided heating in the inside of the furnace to a temperature of 1000 ^{0}C.

Fig. 5 *General view of the furnace and the sample after one-sided heating in the inside of the furnace to a temperature of 1000 ^{0}C*

The integrity of the samples was assessed by the presence of through cracks and the presence of flames on the unheated surface of the sample, which could arise from the penetration of fire through these cracks. In addition, 9 characteristic points were distinguished on the surface of the sample heated in accordance with the requirements of the normative document (DSTU B V.1.1-4-98, 1998), according to which the deformations after heating were measured. The general view of the sample after the integrity test is shown in Fig. 6.

Fig. 6 *General view of the concrete specimen after the integrity test*

3.3 Design features of the floor slab

Currently, most of the floors of residential and public buildings are made of precast hollow-core slabs. These slabs are manufactured in precast factories and delivered directly to construction sites. Hollow core slabs are manufactured up to 9.0 m long and could have widths of 1.0, 1.2, 1.5, and 1.8 m.

The use of such concrete floor slabs is technologically advanced, since it permits the exclusion of the assembly process, i.e., dismantling of the formwork and the process of monitoring the concrete with respect to gaining the necessary strength in a certain climatic period of the year.

Fig. 7 shows a cross-section of a 6.0 m long and 1.5 m wide hollow-core floor slab.

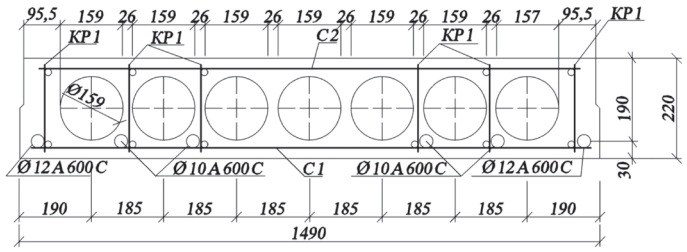

Fig. 7 *Cross-section of a hollow-core floor slab with a width of 1.5 m*

According to the calculations for the first and second groups of limit states, a floor slab for office buildings is reinforced with 6 rods (two rods with a diameter of 12 mm and four rods with a diameter of 10 mm) of prestressed class A600C reinforcement. In addition to the prestressed reinforcement, the slab is reinforced with C1 and C2 reinforcement meshes made of a Bp-I class reinforcement with a diameter of 3-4 mm, which are located in the lower and upper parts of the slab, as well as 6 Kr1 reinforcement cages made of a class A240C reinforcement with a diameter of 6-8 mm. The total mass of the slab is 2.56 tons; the volume of concrete is 1.125 m^3; and the consumption of steel is 89.1 kg.

The standardized fire resistance of such a hollow-core slab, as determined by the source (DSTU-N B EN 1992-1-2:2012, 2012), is REI 60.

The weakest structural points of such plates are:
- relatively small sections of concrete from the lower and upper surfaces of the slab to the voids, which are 30.5 mm;
- the thickness of the wall between the voids, which is 26 mm;
- the composition of the concrete from a binder made of Portland cement in monolithic reinforced concrete structures is limited by the maximum temperature applied, which is 1100 ^{0}C (DSTU B V.1.1-6-2001, 2002).

The listed disadvantages of the hollow-core floor slabs are practically confirmed after examining the slabs exposed to the fire (Fig. 1-4).

Considering the above design disadvantages of hollow-core floor slabs when exposed to fire, we put forward the following assumptions:
- structurally, a slab can be made of a solid section without voids, which is much more technologically advanced in its manufacture;
- due to the use of lightweight concrete components with a high degree of refractoriness, the normalized fire resistance of slabs can be increased;
- due to the use of lightweight concrete, the heat-insulating and sound-insulating ability of slabs and floors as a whole can be improved.

4 RESULTS AND DISCUSSION

4.1 Study results of lightweight fire-resistant concrete characteristics

The study results of the physical and mechanical characteristics of the lightweight fire-resistant concrete are given in Tab. 4, and the fire characteristics are in Tab. 5.

Tab. 4 *Basic physical and mechanical characteristics of lightweight fire-resistant concrete (DBN V.1.1-7-2002, 2002)*

Product name	Name of indicators						
	Bulk weight kg/m^3	Volume shrinkage, %	Thermal conductivity coefficient, W/m·K	Cubic strength, MPa	Prismatic strength, MPa characteristic / estimated	Elastic modulus, MPa	Concrete class, C(B)
Lightweight fire-resistant concrete	1475	0.58	0.68	18.36	12.0 / 9.25	$14.2 \cdot 10^3$	C16/20 (B15)

Tab. 5 *Fire characteristics of lightweight concrete*

Product name	Name of indicators							
	After heating to 1000 °C							
	Bulk weight kg/m^3	Volume shrinkage, %	Thermal conductivity coefficient, W/m · K	Cubic strength, MPa	Through cracks	Cracks and other defects	Deflections	Fire resistance limit
Lightweight fire-resistant concrete	1400	0.86	0.62	14.58	No	Mesh of cracks in depth to 2.5 mm and width a_{max} = 0.15-0.2 mm	0.1 – 0.2	REI 90

As can be seen in Tab. 4, the composition of the lightweight fire-resistant concrete developed has a volumetric weight of 1475 kg/m^3, which is significantly less than the volumetric weight of the heavy concrete (2200-2300 kg/m^3) that is used for the manufacture of hollow-core slabs; it has a relatively small volumetric shrinkage of 0.58 % and a thermal conductivity coefficient of 0.68 W/m · K versus 1.86 W/m · K for heavy concrete.

In terms of its strength and deformation characteristics, this concrete has a cubic strength of 18.36 MPa, a prismatic strength of 12.0 MPa, and a modulus of elasticity of 14.2 · 10^3 MPa.

Based on the strength and deformability characteristics of this fire-resistant concrete, it can be classified as C16/20 (B15).

As can be seen in the Tab. 5, the volumetric weight of the lightweight fire-resistant concrete C decreases to 1400 kg/m^3 after heating to 1000 °C, and the volumetric shrinkage increases to 0.86 %, which is associated with the evaporation of the physically bound water and compaction of the concrete structure. There is also a decrease in the strength of the concrete to 14.52 MPa and the thermal conductivity coefficient to 0.62 W/m · K. There are no through cracks in the samples after the one-sided heating of the concrete samples to 1000 ^{0}C, which means that there is no flame on the unheated surface of the sample. A network of cracks along the binder with a depth of 2.5 mm and a maximum width of 0.1-0.2 mm was observed after cooling the samples from the side of the heated concrete surface.

The deformations of the concrete specimens, which were measured at characteristic points on the heated surface, indicate the presence of deflections, which amounted to 0.1-0.2 mm, and which are less than the maximum allowable deflections equal to 1.07 mm, determined according to the source (Nekrasov, K. D., 1957).

Thus, according to the fire characteristics, which were investigated after heating the lightweight concrete to a temperature of 1000 °C, the fire resistance limit of the concrete, i.e., REI 90, was practically determined.

4.2 Design engineering of a lightweight fire-resistant concrete floor slab

Considering the characteristics of the composition developed of the lightweight fire-resistant concrete of a binder made of alumina cement and having a fire resistance limit of REI 90, we consider it possible to use floor slabs on a large section with a height of 200 mm.

Such slabs are much less labor-intensive to manufacture, since they do not require the use of hollow formers, and the weight of a 6.0 x 1.5 m slab will be 2.73 tons, which slightly exceeds the weight of a hollow-core slab, which is 2.56 tons.

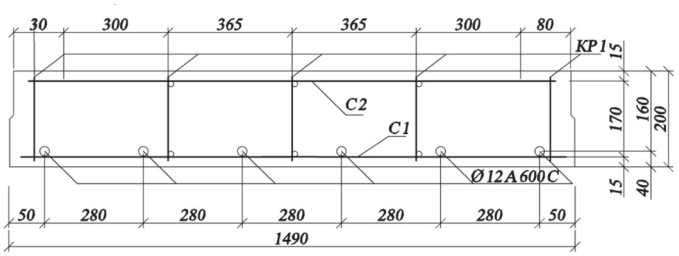

Fig.8 Cross-section *of a solid floor slab with a length of 6.0 m and a width of 1.5 m*

As a result of the selection of the lightweight fire-resistant concrete composition and the calculation and design of a solid floor slab with dimensions of 6.0 × 1.5 m, the following results were achieved:

– to reduce the labor intensity of the slab due to the use of a solid cross-section of the slab instead of a hollow section;
– to exclude the destruction of thin concrete walls between the voids in the case of a fire;
– to increase the distance to the axis of the prestressed reinforcement to 40 mm instead of 30 mm for hollow-core slabs and thereby increase the thickness of the concrete cover to 35 mm;
– to increase the normalized fire resistance of the slabs to REI 90, which is 30 minutes higher than the fire resistance of hollow-core floor slabs due to the use of components with a high degree of refractoriness in the composition of fire-resistant concrete;
– to significantly increase the heat-insulating ability of the slab, since the thermal conductivity coefficient of the concrete of a light fire-resistant slab is λ = 0.68 W/(m · K), which is significantly less than the thermal conductivity coefficient of heavy concrete equal to λ = 1.86 W/(m · K);
– in addition, to significantly improve the sound-insulating properties of the structure of the floor slab developed.

5 CONCLUSIONS

The article analyses the impact of fire on the structures of buildings and other constructions. It has been established that floor slabs, the standardized fire resistance of which is REI 45-60, are the most vulnerable to fire.

The main disadvantages of the use of hollow-core floor slabs made of heavy concrete from Portland cement when exposed to fire include the limitation of the maximum temperature applied for concrete compositions with a binder made of Portland cement, which is 1100 ^{0}C; the thinness of the wall between the voids, which is 26 mm, and which is destroyed even at temperatures below 1000 ^{0}C; the relatively small thickness of the areas of the concrete from the lower and upper surfaces of the slab to the voids, which are 30.5 mm, and in which the reinforcement is placed; and the insufficient thickness of the concrete's protective layer to reliably protect the reinforcement from fire.

The noted disadvantages of hollow-core floor slabs incentivize discussing the possibility of increasing the fire-retardant properties of concrete due to the use of light materials with a high degree of refractoriness and of a constructive solution whereby solid floor slabs can be used.

To solve the above problems, a composition of lightweight fire-retardant concrete with a bulk density of 1475 kg/m^3 has been developed, where expanded clay is used as a filler; alumina cement is used as a binder; and water is the grout. The normalized fire resistance of such concrete, which was REI 90, has been practically investigated, it is higher than the fire resistance of hollow-core slabs, which is REI 60.

In a construction sense, manufacturing such solid floor slabs, without any voids, is proposed. In this case, due to the use of lightweight concrete, the weight of the solid floor slabs will be minimally different from the weight of hollow-core slabs. The use of solid floor slabs will eliminate the destruction of thin concrete walls (as occurs in hollow-core slabs) and will increase

the thickness of the protective concrete layer to reliably protect the reinforcement from fire. In addition, the heat-insulating and sound-insulating ability of the solid floor slabs will be significantly improved, since the thermal conductivity coefficient of the lightweight concrete developed is 2.74 times lower than the thermal conductivity coefficient of the heavy concrete of the hollow-core floor slabs.

Since the concrete composition developed has good fire resistance, it can be recommended for construction devices for various fire barriers, such as walls, partitions and doors.

REFERENCES

DSTU B.V.2.7 - 41-95 (1995) *Building materials. Method for determining thermal conductivity by a surface transducer,* (ДСТУ Б.В.2.7 – 41-95. *Материалы строительные. Метод определения теплопроводности поверхностным преобразователем*), Ukrainian National Standard, Entered into force from 01-01-1996, Ministry of Regional Development, Construction, and Housing Services (Buildings standards of Ukraine), 14 pp.

DSTU B V.1.1-4-98 (1998) *Fire protection. Building construction. Fire resistance test methods. General requirements* (ДСТУ Б В.1.1-4-98. *Защита от пожара. Строительные конструкции. Методы испытания на огнестойкость. Общие требования*), Ukrainian National Standard, Entered into force on 28-10-1998, Ministry of Regional Development, Construction, and Housing Services (Buildings standards of Ukraine), 19 pp.

DSTU B V.1.1-6-2001 (2002) *Fire protection. Doors and gates. Fire resistance test methods (ДСТУ Б В.1.1-6-2001. Защита от пожара. Двери и ворота. Методы испытания на огнестойкость*), Ukrainian National Standard, Entered into force on 30-11-2001, Gosstroy of Ukraine (Buildings standards of Ukraine), 14 pp.

DBN V.1.1-7-2002 (2002) *Fire protection – Fire safety of construction objects. (ДБН В.1.1-7-2002 Защита от пожара. Пожарная безопасность объектов строительства.)*, Ukrainian National Standard, Entered into force on 01-05-2003, Ministry of Regional Development, Construction, and Housing Services, (Buildings standards of Ukraine), 2003, 44 pp.

DSTU B V.2.7. - 214: 2009 (2009) *Concrete. Methods for evaluating the quality of control tests,* (ДСТУ Б В.2.7. – 214:2009. *Бетони. Методи визначення міцності за контрольними зразками*), Ukrainian National Standard, Entered into force on 22-12-2009, Ministry of Regional Development, Construction, and Housing Services (Buildings standards of Ukraine), 43 pp.

DSTU B.V.2.7 – 217:2009 (2009) *Concrete. Methods for evaluating prism power, spring modulus and Poisson coefficient, (ДСТУ Б.В.2.7 – 217:2009. Бетони. Методи визначення призмової міцності, модуля пружності і коефіцієнта Пуассона*), Ukrainian National Standard, Entered into force on 01-09-2010, Ministry of Regional Development, Construction, and Housing Services (Buildings standards of Ukraine), 16 pp.

DSTU-N B EN 1992-1-2:2012 (2012) *Eurocode 2: Design of concrete structures - Parts 1-2: General rules - Structural fire design* (ДСТУ-Н Б EN 1992-1-2:2012. *Єврокод 2. Проектування залізобетонних конструкцій. Частина 1-2. Загальні положення. Розрахунок конструкцій на вогнестійкість*), Ukrainian National Standard, Entered into force on 08-06-2008, Authority: The European Union Per Regulation 305/2011, Directive 98/34/EC, Directive 2004/18/EC, 97 pp.

GOST 20910-90 (1990) *Heat-resistant concretes. Specifications* (ГОСТ 20910-90. *Бетоны жаростойкие. Технические условия*), Ukrainian National Standard, Entered into force on 01-07-1991, Ministry of Regional Development, Construction, and Housing Services (Buildings standards of Ukraine), 1991, 17 pp.

Milovanov, A. F. (1986) *Fire resistance of reinforced concrete structures*, Construction publishing house, 224 pp.

Nekrasov, K. D. (1957) *Heat-resistant concrete*, Promstroyizdat, 1957. – 283 pp.

Phan, L. T. - McAllister, P. M. - Gross, J. L. - Hurley, M. J. (2010) *Best practice guidelines for structural fire resistance design of concrete and steel buildings*. NIST Technical note 1681 – Nov. 2010, 217 pp.

Yakovlev, A. I. (1985) *Calculation of fire resistance of building structures*, Construction publishing house, 141 pp.

NIIŽB (1987) *Recommendations for the inspection of buildings and structures damaged by fire*, (Научно-исследовательский Институт Бетона и Железобетона (ниижб) ГОССТРОЯ СССР - *Рекомендации по обследованию зданий и сооружений, поврежденных пожаром*), Research, Design and Technological Institute of Concrete and Reinforced Concrete of The Ussr State Construction, 57 pp.

NIIŽB (1989) *A manual for the design of concrete and reinforced concrete structures intended for operation under conditions of exposure to high temperatures (to SNiP 2.03.04-84)* (Научно-исследовательский Институт Бетона и Железобетона (ниижб) ГОССТРОЯ СССР - *Пособие по проектированию бетонных и железобетонных конструкций, предназначенных для работы в условиях воздействия повышенных и высоких температур* (к СНиП 2.03.04-84)), Design and Technological Institute of Concrete and Reinforced Concrete 1989, 184 pp.

sciendo

Slovak Journal of Civil Engineering

Vol. 30, 2022, No. 1, 8 – 20
DOI: 10.2478/sjce-2022-0002

A NEW APPROACH FOR DETERMINING THE CURVATURE DUCTILITY OF REINFORCED CONCRETE BEAMS

Saeid FOROUGHI[1*], S. Bahadir YUKSEL[1]

Abstract

This paper presents a numerical parametric study of the moment-curvature and curvature ductility of doubly-reinforced beams with different parameters. The effects of the strength of the concrete and the amount of the reinforcement, including the tensile and compression reinforcement on the complete moment-curvature behavior and the curvature ductility factor of the beam sections, have been studied. A new predictive formula for the ductility factor of beam sections that considers the different parameters has been developed. In a continuation of the study, the flexural ductility of beams designed with different parameters according to the ductility factor proposed by different researchers was investigated. Based on the results of the numerical analysis, the proposed predictions for the curvature ductility factor were verified by comparisons with other predictive formulas. The proposed formula offers fairly accurate and consistent predictions for the curvature ductility factor of beam sections. It is shown that the concrete's compression strength and the amount of reinforcing steel, including the compression reinforcement ratios, have an effect on the curvature ductility factor of beam sections.

Address

[1] Dept. of Civil Engineering, Faculty of Engineering and Natural Sciences, Konya Technical University, Konya, Turkey

[*] ***Corresponding author:*** saeid.foroughi@yahoo.com

Key words

- Numerical analysis,
- Moment-curvature,
- Ductility,
- Flexural,
- Reinforced concrete beam,
- Reinforcement.

1 INTRODUCTION

Ductility can be defined as the ability of a material to undergo large deformations without any rupture before failure (Zareef and Madawy, 2018). The ductility of reinforced concrete (RC) beams is very important since it is essential to avoid the brittle failure of the structure by ensuring adequate curvature at the ultimate limit state (Arsalan and Cihanli, 2010). The ductility of RC beams is the property that allows structures to dissipate energy under seismic loading; consequently, the brittle failures of RC structures can be avoided (Haytham and Amar, 2017). The ductility performance of a RC member does not increase or decrease in direct proportion to the ductility of the concrete used; it is also dependent of other parameters such as the reinforcement details (Kwan et al., 2002). In the flexural design of RC beams, the strength and deformability, which are interrelated, need to be considered simultaneously. However, in current design codes, the design of a beam's strength is separated from its deformability, and an evaluation of its deformability is independent of some key parameters, such as the concrete's strength, the steel's yield strength, and the confinement content (Adari, 2017). Several researchers (Bai and Au, 2011; Ho et al., 2004; Debernardi and Taliano, 2002; Pecce and Predictions, 1999) have reported that the values of the curvature ductility for beam sections with normal and high strength concrete are different. Also, it has been determined that the flexural ductility of RC beam sections is dependent not only on the amount of the reinforcement, including the compression reinforcement, but also on the concrete's compressive strength and the steel's yield strength (Lee, 2013).

The factors affecting the nonlinear behavior of RC beams are the tensile and compression reinforcement ratio and the compressive strength of the concrete. The aim of this study is to examine

the effects of factors such as the tensile reinforcement ratio, the compression reinforcement ratio, and the concrete's compressive strength, which affect the moment- curvature relationships and ductility of RC beam sections. Rectangular beam section models with an equal cross-sectional area having different parameters were designed. In this study, the effects of the concrete's compression strength, and the amount of reinforcement, including the tensile and compression reinforcement, on the complete moment-curvature and the curvature ductility factor of doubly-reinforced beams have been evaluated. A new predictive formula for the curvature ductility factor of doubly-reinforced beam sections that considers the different parameters has been developed. In a continuation of the study, the flexural ductility of doubly-reinforced beam models designed with different parameters according to the relations proposed by different researchers was investigated analytically. The final results obtained were examined by comparing them according to different parameters and models.

2 FLEXURAL DUCTILITY OF REINFORCED CONCRETE BEAMS

In the case of a flexural member, its sectional ductility based on the curvature and/or the member's ductility based on deflection is usually considered (Park and Paulay, 1975). Moment- curvature relationships are a useful resource for the solution of a variety of inelastic and geometrically non-linear structural problems involving elements under a combined axial load and bending (Liew, 2017; Simao et al., 2016). Determining the moment and curvature response of a cross-section is an important step in fulfilling strength and serviceability design requirements (Dhakal and Moustafa, 2019). Yield moment (M_y), ultimate moment (M_u), yield curvatures (φ_y), ultimate curvatures (φ_u) and curvature ductility (μ_φ) values are calculated from the moment-curvature relationships. The curvature ductility factor is obtained by the ratio between the curvature determined at the ultimate limit state and the curvature determined at the first yield ($\mu_\varphi = \varphi_u/\varphi_y$).

2.1 Previous Research on the Curvature Ductility Factor

A considerable amount of studies on the ductility and flexural behavior of normal and high- strength concrete elements under a static load can be found in the literature (Lee, 2013; Au et al., 2011; Bai and Au, 2011; Arslan and Cihanli, 2010; Lam et al., 2009a, 2009b; Jang et al., 2008; Rashid and Mansur, 2005; Ho et al., 2004). The ultimate states in each research work are defined in different forms. In this part of the study, the flexural ductility of doubly-reinforced beam models designed with different concrete strengths and compression and tensile strength ratios according to the relations proposed by the different researchers was investigated analytically. The bending ductility of doubly-reinforced beams was obtained by using the relations suggested from (Lee, 2013; Kwan and Ho, 2010; Kwan et al., 2002; Pam et al., 2001a, 2001b). The equations defining the curvature ductility of doubly-reinforced beam elements are summarized below. Pam et al., (2001a) derived the predictive equation (1) based on the results of designing beam sections with the concrete strength f_{cc} from 30MPa to 100MPa, a steel yield strength f_y = 400~460MPa, the tensile reinforcement ratio ρ' from 1%-5%, and the compression reinforcement ratio ρ' from 0%-1.5%. The ductility factor has been correlated with the concrete grade, and the tensile and compression steel ratios by regression analysis; the following formula is given for a direct evaluation of the flexural ductility derived: ρ is the tensile reinforcement ratio; ρ_b is the balanced reinforcement ratio; ρ' is the compression reinforcement ratio; and f_{ck} is the concrete compressive strength:

$$\mu = 10.7\left(f_{ck}\right)^{-0.45}\left[\left(\rho-\rho'\right)/\rho_b\right]^{-1.25}\times\left[1+95.2\left(f_{ck}\right)^{-1.1}\left(\rho'/\rho\right)^3\right] \quad (1)$$

Replacing the last term in Equation (1) by unity, a simplified equation (2) for the ductility factor was proposed by Kwan et al. (2002):

$$\mu = 10.7\left(f_{ck}\right)^{-0.45}\left[\left(\rho-\rho'\right)/\rho_b\right]^{-1.25} \quad (2)$$

Kwan and Ho (2010) obtained the μ values that are correlated to the various structural parameters using regression analysis to produce Equation (3) to enable a direct evaluation of the flexural ductility of beams without conducting any nonlinear moment-curvature analysis. In Equation (3), λ is the degree of reinforcement, and f_r is the confining compression. Herein, the degree of reinforcement is denoted by λ and explicitly defined as $\lambda = (\rho - \rho')/\rho_b$. In order to study the effects of the various structural parameters, i.e., f_{ck} = 40-100 MPa, f_y = 250-600MPa, f_r = 0-4MPa, ρ'= 0-2%, and ρ = 0.4 ρ_b – 2ρ_b are considered:

$$\begin{aligned} &\mu = 10.7m\left(\lambda\right)^{-1.25n}\left(f_{ck}\right)^{-0.45}\left(f_y/460\right)^{-0.25} \\ &m = 1+2.5\left(f_{ck}\right)^{-0.5}\left(f_r/f_{ck}\right), \quad n = 1+5.0\left(f_r/f_{ck}\right) \end{aligned} \quad (3)$$

Lee (2013) studied the effects of concrete strength, steel yield strength, and the amount of reinforcement, including compression reinforcement on the complete moment-curvature behavior and the curvature ductility factor of doubly-reinforced beam sections. For the parametric study, f_{ck} = 30-100MPa to cover both normal and high-strength concretes, f_y = 300- 600MPa, $E_s = 2\times10^5 Mpa$, $\rho = 0.1\rho_b$-ρ_b and ρ'= ρ are considered. In doubly-reinforced beam sections, considering the influence of parameters such as the material strength, reinforcement ratio, and stress of the compression reinforcement, the predictive equation of the curvature ductility factor can be offered based on the previous parametric study as Equation (4). f_{sc} is the stress of the compression reinforcement, which is calculated at the ultimate stage (Lee, 2013).

$$\begin{aligned} &\mu_\varphi = \left[\left(\rho-\rho'\frac{f_{sc}}{f_y}\right)/\rho_b\right]^{-1.283}\left(f_y\right)^{-0.230}\left[-0.6\left(f_{ck}\right)^2+95.2\left(f_{ck}\right)+2506.2\right]\times10^{-3} \\ &\theta_p = \left(\varphi_u-\varphi_e\right)L_p = \left[\varphi_u-\left(\frac{M_u}{M_y}\right)\varphi_y\right]L_p \end{aligned} \quad (4)$$

3 PLASTIC ANALYSIS FOR BEAMS

Methods based on a plastic analysis should only be used for the inspection at the ultimate limit state. The ductility of the critical sections should be sufficient for the envisaged mechanism to be formed. The plastic analysis should be based either on the lower bound (static) method or on the upper bound (kinematic) method. Plastic analysis without any direct inspection of the rotation capacity may be used for the ultimate limit state if the conditions

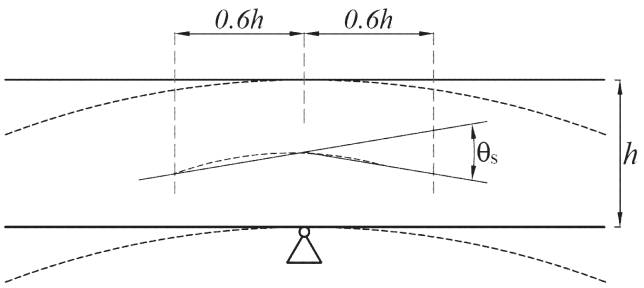

Fig 1. *Plastic rotation (θ_s) of reinforced concrete sections for continuous beams (Eurocode 2, 2004; Model Code, 2010)*

of the ductility of the critical sections are met (Eurocode 2, 2004; Model Code, 2010).

3.1 Rotation Capacity

The simplified procedure for continuous beams is based on the rotation capacity of the beam over a length of approximately 1.2 times the depth of the section. It is assumed that these zones undergo plastic deformation (formation of yield hinges) under the relevant combination of actions. The verification of the plastic rotation in the ultimate limit state is considered to be fulfilled if it is shown that under the relevant combination of actions, the calculated rotation, θ_s, is less than or equal to the allowable plastic rotation (Fig. 1).

In the region of yield hinges, x_u/d should not exceed the value of 0.45 for concrete strength classes less than or equal to C50/60 and 0.35 for concrete strength classes greater than or equal to C55/67. x_u is the neutral axis depth, and d is the effective depth of a cross-section. The rotation θ_s should be determined on the basis of the design values for the actions and materials and on the basis of the mean values for prestressing at the relevant time. In the simplified procedure, the allowable plastic rotation may be determined by multiplying the basic value of the allowable rotation ($\theta_{pl,d}$) by correction factor k_λ, which depends on the shear slenderness. The recommended values for steel Classes B and C and concrete strength classes less than or equal to C50/60 and C90/105 are given in Fig. 2 (the values apply to a shear slenderness of λ=3.0). The values for concrete strength classes C 55/67 to C 90/105 may be interpolated accordingly. The values apply for a shear slenderness of λ=3.0. For different values of the shear slenderness, $\theta_{pl,d}$ should be multiplied by $k_\lambda = \sqrt{\lambda/3}$, where λ is the ratio of the distance between the zero point and the maximum moment after redistribution. As a simplification, λ may be calculated for the concordant design values of the bending moment and shear ($\lambda = M_{sd}/(V_{sd} \cdot d)$) (Eurocode 2, 2004; Model Code, 2010).

The plastic hinge rotation (θ_p), of RC beams depends on a number of parameters, including the definition of the yielding and ultimate curvatures, section geometry, material properties, tension and compression reinforcement ratios, transverse reinforcement, cracking and tension stiffening, the stress-strain curve for the concrete, the stress-strain curve for the reinforcement, the bond-slip characteristics between the concrete and the reinforcing steel, the support conditions and the magnitude and type of loading, the axial force, the width of the loading plate, the influence of the shear, and the presence of a column. The moment-curvature relationship of a typical beam subjected to a uniform load are shown in Fig. 3. It is recommended to estimate the plastic rotational capacity that

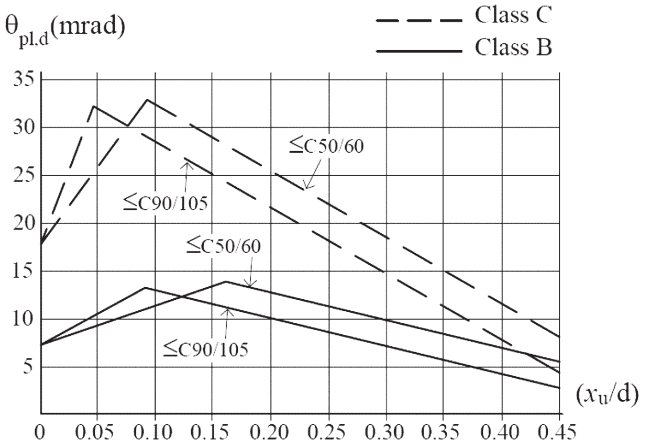

Fig. 2 *Basic value of the allowable rotation ($\theta_{pl,d}$), of the reinforced concrete sections for Class B and C reinforcements (Eurocode 2, 2004; Model Code, 2010)*

can be achieved at potential plastic hinge sections by utilizing the moment-curvature relationships of the sections. The value of the plastic hinge rotation at the ultimate stage can be easily calculated by the following Equation (5), where φ_u refers to the maximum curvature, and φ_y refers to the yield curvature, as shown in Fig. 3. The length of the plastic deformation region, which is called the plastic hinge length (L_p), is taken as half of the section length in the active direction ($L_p = 0.5h$).

$$\theta_p = (\varphi_u - \varphi_e) L_p = \left[\varphi_u - \left(\frac{M_u}{M_y} \right) \varphi_y \right] L_p \tag{5}$$

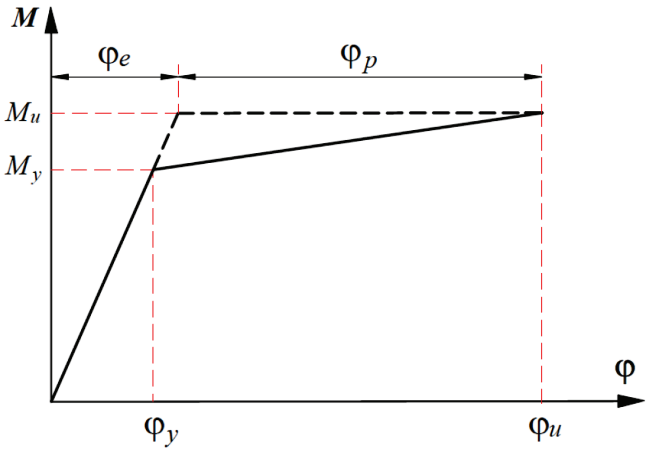

Fig. 3 *Moment-curvature relationship for reinforced concrete beams*

4 MATERIALS AND METHOD

Many variables influence the curvature ductility with the nonlinear behavior of RC beams, and the numerical analysis presented was performed on models designed by considering variable parameters. The effect of the different parameters was studied by varying one parameter at a time and keeping the value of the other parameters fixed. The summary of the designed RC beam cross-section properties is given in Tab. 1. A typical beam section has a width of b_w = 300mm , and a total depth of h = 600mm was designed. The compression and tensile reinforcement is provided at depth d′ = 50mm and d = 550mm (d = h − d′) from the top, respectively. For all the

RC members, C25, C30, C35, C40, C45 and C50 were chosen as the concrete grade, and B420C was selected as the reinforcement for the reinforcement behavior model. Concrete with a strength lower than C25 cannot be used in all RC buildings to be built within the scope of the Turkish Building Earthquake Code (TBEC, 2018) regulations. In moment-curvature analyses, the material models given in Tab. 2 were used for the unconfined concrete and reinforcement steel. Due to its insignificant effect, the tensile strength of the concrete has been ignored in the moment-curvature analyses.

The most important issue to be considered when calculating and designing an RC beam section is to ensure that the reinforcement ratio obtained is smaller than the balanced reinforcement ratio. The limit values given in TS500 (2000) are taken into consideration in this study. The ratio of the tensile reinforcement (ρ) in the beams should not be less than the minimum values given in Equation (6). In TS500 (2000), the reinforcement ratio is limited to Equation (7) in order to provide ductile behavior in the RC beams. The ratio of the tensile reinforcement in the RC beams should not be more than the maximum value given in Equation (7) and not more than 2%. The difference between the tensile and compression reinforcement ratios in the beams should not exceed 0.85 of the balanced reinforcement.

$$\rho = \frac{A_s}{b_w d} \geq \rho_{\min} = 0.8\frac{f_{ctd}}{f_{yd}} \tag{6}$$

$$(\rho - \rho') \leq \rho_{\max} = 0.85\rho_b$$

$$\rho_b = 0.85k_1\left(\frac{f_{ctd}}{f_{yd}}\right)\left(\frac{700}{700+f_{yd}}\right) \tag{7}$$

The k_1 value is provided should not be less than 0.70 and not greater than 0.85 (TS500, 2000).

$$\begin{aligned} k_1 &= 0.85 - 0.006(f_{ck} - 25) < 0.85;\ f_{ck} > 25\ \text{MPa}\alpha \\ k_1 &= 0.85 \qquad\qquad\qquad\qquad ;f_{ck} \leq 30\ \text{MPa}\alpha \end{aligned} \tag{8}$$

A total of 66 RC beam models with different concrete strengths and different tensile and compression reinforcement ratios have been designed (Tab. 1). The provisions in TBEC (2018) and TS500 (2000) have been taken into consideration in the design of the RC beam models. In the RC beam models designed in different parameters, i.e., $\rho_{max} = 0.85\rho_b$ as the ratio of tensile reinforcement and the values of $\rho' = 0.0$, $0.1\rho_{max}$, $0.2\rho_{max}$, $0.3\rho_{max}$, 0.4ρ, $0.5\rho_{max}$, $0.6\rho_{max}$, $0.7\rho_{max}$, $0.8\rho_{max}$, 0.9, and ρ_{max}, as the compression reinforcement ratio are taken into account. In the RC beam models, six different concrete classes i.e., C25, C30, C35, C40, C45 and C50 were taken into account. In the beam models, the tensile reinforcement ratio for each concrete strength was kept constant with $\rho_{max} = 0.85\rho_b$. By changing the compres-

Tab. 1 *Details for the RC beam cross-sections designed*

ρ'/ρ	Material: C25		Material: C30		Material: C35		Material: C40		Material: C45		Material: C50	
	ρ	ρ'	ρ	ρ'	ρ	ρ'	ρ	ρ'	ρ	ρ'	ρ	ρ'
0.0		0.0		0.0		0.0		0.0		0.0		0.0
0.1		0.0018		0.0021		0.0024		0.0026		0.0028		0.0030
0.2		0.0037		0.0043		0.0048		0.0053		0.0057		0.0061
0.3		0.0055		0.0064		0.0072		0.0079		0.0085		0.0091
0.4		0.0074		0.0085		0.0096		0.0105		0.0114		0.0121
0.5	0.0184	0.0092	0.0213	0.0107	0.0240	0.0120	0.0263	0.0132	0.0285	0.0142	0.0303	0.0152
0.6		0.0111		0.0128		0.0144		0.0158		0.0171		0.0182
0.7		0.0129		0.0149		0.0168		0.0184		0.0199		0.0212
0.8		0.0147		0.0171		0.0192		0.0211		0.0228		0.0243
0.9		0.0166		0.0192		0.0216		0.0237		0.0256		0.0273
1.0		0.0184		0.0213		0.0240		0.0263		0.0285		0.0303

Tab. 2 *Material parameters for the concrete and reinforcement (TBEC, 2018)*

Standard Strength	Parameters	Values
Concrete: C25-C50	Strain at maximum stress of unconfined concrete (ε_{co})	0.002
	Ultimate compression strain of concrete (ε_{cu})	0.0035
	Characteristic standard value of concrete compressive strength (f_{ck})	25-50MPa
Reinforcement: B420C	Yield strain of reinforcement (ε_{sy})	0.0021
	Strain hardening value of reinforcing steel (ε_{sp})	0.008
	Strain in reinforcing steel at ultimate strength (ε_{su})	0.08
	Characteristic yield strength of reinforcement (f_{yk})	420MPa
	Ultimate strength of reinforcement (f_{su})	550MPa

sion reinforcement ratios, the moment-curvature relation of the RC beams were obtained. The analytically investigated parameters were calculated from different relations and moment-curvature relationships. Events such as how the stiffness and strength of the sections change and the ductility state of the cross-sectional behavior can also be observed through the moment-curvature relationship. The moment-curvature relationship is essential for the inelastic analysis of structures to predict section strengths, flexural stiffness, and section ductility. For the moment-curvature relations, SAP2000 software [20] was used to consider the different parameters. The curvature ductility was calculated from the established moment-curvature relationships. The major factors affecting the curvature ductility of a doubly-reinforced beam section were investigated. In the continuation of the study, a new predictive formula for the curvature ductility factor of the doubly-reinforced beam sections has been developed considering the different parameters. Based on the numerical analysis results, the proposed predictions for the curvature ductility factor were verified by comparisons with other predictive formulas.

5 RESEARCH FINDINGS AND DISCUSSION

5.1 Nonlinear Moment-Curvature Analysis

In this part of the study, the moment-curvature relations of the RC beam elements designed with different parameters were obtained, and the curvature ductility was calculated. The moment-curvature relationships were obtained by SAP2000 software, which takes the nonlinear behavior of materials into consider-

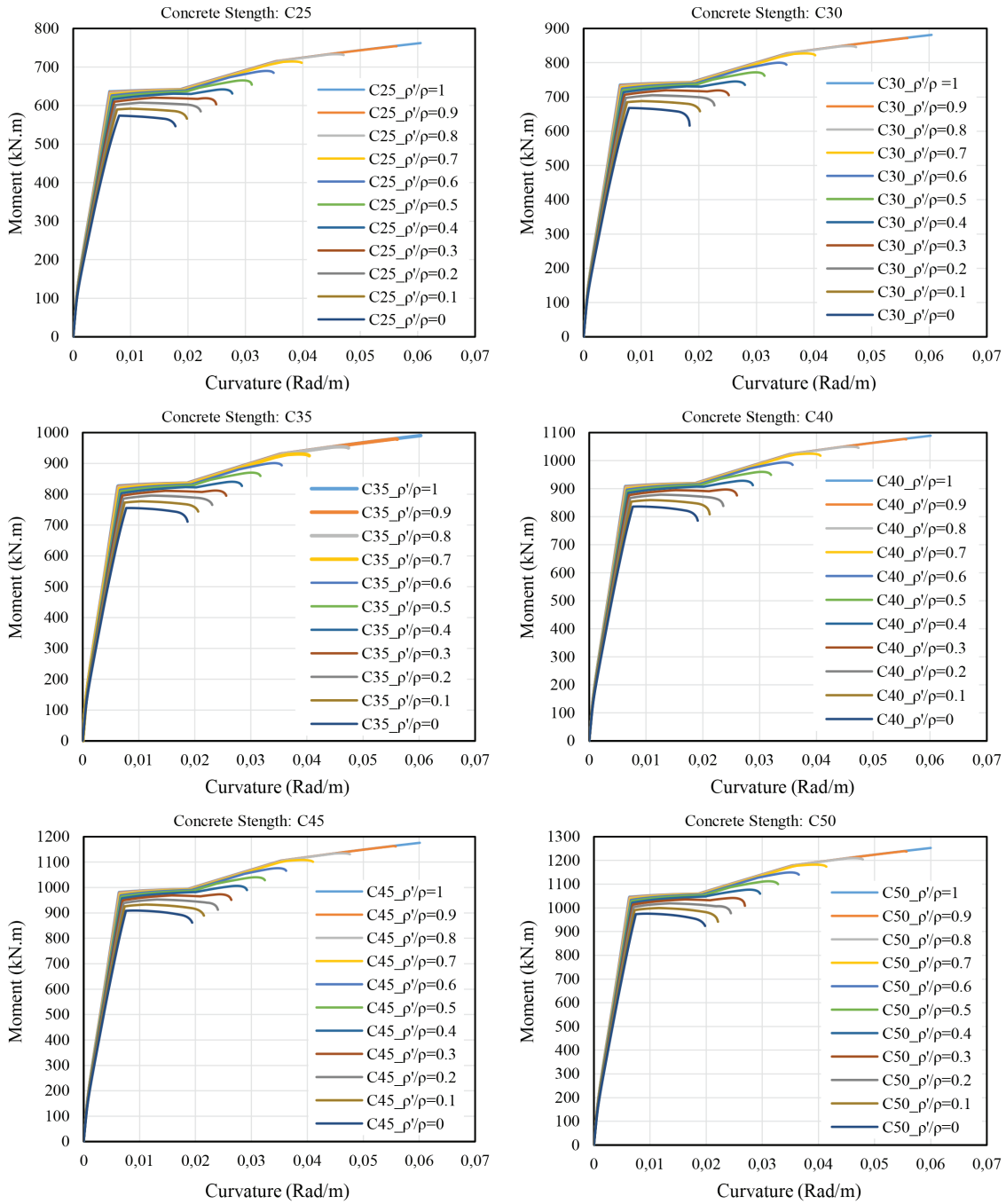

Fig. 4 *Comparative moment-curvature relations for doubly-reinforced beam sections with different compressive reinforcement ratios*

ation. The moment-curvature relationships of the rectangular RC beams for different longitudinal reinforcements (tensile and compression) and concrete strengths were obtained. The behavioral effects of the parameters examined were evaluated by the curvature ductility and moment-carrying capacity of the cross-section. The moment- curvature relationships obtained from the analytical results are presented in graphic form. The essential factors influencing the local ductility of the RC beams are the concrete strength, the yield strength of the steel, and the ratio of the tensile and compression reinforcement (ρ and ρ'). A comparison of the moment-curvature relationships of the RC beams for different concrete strengths, i.e., ρ'/ρ, is given in Fig. 4. The effect of the ρ'/ρ and concrete strength on the yield, ultimate moment, and curvature are given in Figs. 5 and 6. Since the maximum value of the axial load in the RC beams is limited to $N = 0.10A_c f_c$, $N = 0$ is considered in these analyses.

With the increase in the compression reinforcement ratio for the constant compressive strength of the concrete and tensile reinforcement ratio in the RC beams, the yield moment, ultimate moment, and ultimate curvature values obtained from the moment-curvature relationships increase, but the yield's curvature values decrease. With the increase in the compression reinforcement ratio, the maximum moment carrying capacity and ductility of the beam sections increase. It can be seen that the tensile reinforcement ratio for the RC beam sections basically affects both the shape of the moment-curvature curve and the ductility of a beam section. With the increase in the concrete's compressive strength in the RC beams with the constant compression and tensile reinforcement ratio, the yield and ultimate moment values increase.

5.2 Plastic Rotation Capacity of Reinforced Concrete Beams

The plastic rotation capacity that can be achieved in the plastic hinge regions of reinforced concrete beams is calculated from the moment-curvature relations of the sections, according to the relations defined in Eurocode 2 (2004) and Model Code (2010). In order to calculate the rotational capacity of the RC beams, moment and curvature values were obtained from the moment-curvature relations by considering the non-linear behavior of the materials (Equation 5). By using the values recommended for the reinforcement and concrete strength classes in Eurocode (2004) or Model Code (2010), the rotation capacity values were obtained and compared with the values calculated from Equation (5). The rotation capacity values suggested in Eurocode (2004) or Model Code (2010) can be calculated according to the ultimate neutral axis depth and the effective depth of the cross-section values. A comparison of the rotational capacities of the plastic hinges calculated from the moment-curvature relations and according to Eurocode 2 (2004) are shown in Fig. 7.

The analytical results for the 66 RC beams with different tensile and compressive reinforcement ratios are compared with the various formulations given in Eurocode (2004), and calculated from the non-linear behavior relationships of the beams. According to the results obtained from the non-linear behavior of the RC beams, it was concluded that the reinforcement index and the concrete compressive strength have a significant effect on the plastic hinge's rotation capacity (θ_p). The plastic rotation capacity value increases with the increase in the ρ'/ρ ratio and concrete compressive strength. With the increase in the $\lambda = (\rho - \rho')/\rho_b$ value, the plastic rotation capacity value

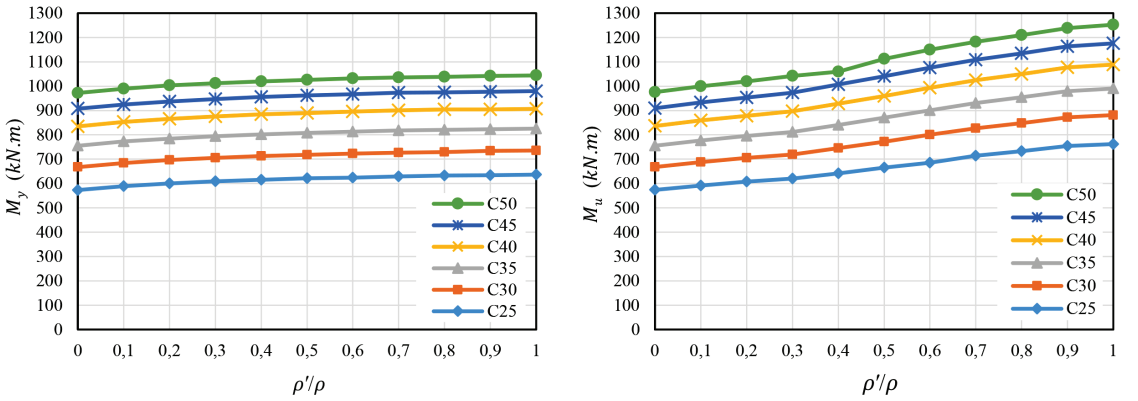

Fig. 5 *Effect of ρ'/ρ and the concrete's strength on the yield and ultimate moment*

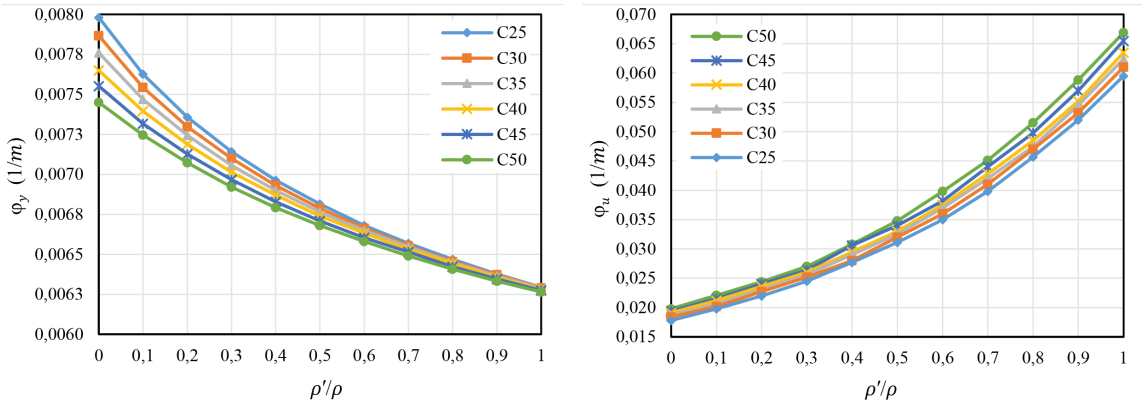

Fig. 6 *Influence of ρ'/ρ and the concrete's strength on the yield and ultimate curvature*

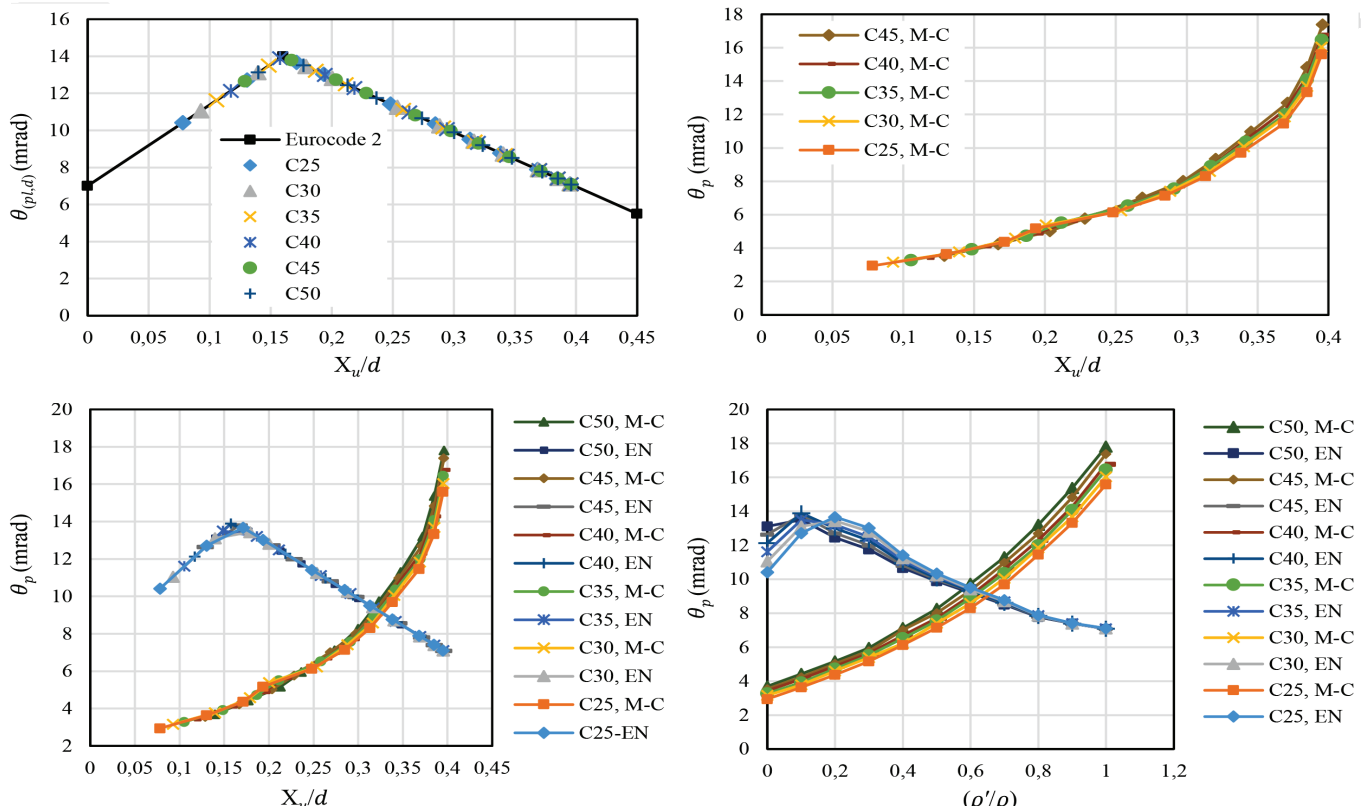

Fig. 7 *Comparison of the rotational capacities of plastic hinges calculated from the moment- curvature relations and according to Eurocode 2 (2004)*

decreases. With the increase of X_u/d value, the plastic rotation capacity value increases.

In Eurocode 2 (2004) or Model Code (2010), limit values are defined for the allowable plastic hinge capacity of RC elements according to different steel classes and concrete strength classes. In the simplified procedure, the allowable plastic rotation may be determined by multiplying the basic value of the allowable rotation ($\theta_{pl,d}$) by a correction factor (k_λ) that depends on the shear slenderness. For B class reinforcement and $f_{ck} \leq 50$MPa, when the x_u/d value is zero, the $\theta_{pl,d}$ value is 7. It can be calculated as $\theta_{pl,d} = 14$ for $x_u/d = 0.16$ and $\theta_{pl,d} = 5.5$ for $x_u/d = 0.45$. The limit values are defined for normal strength and high strength concrete.

In this study, since the concrete strength class is less than 50MPa, the plastic rotation capacity value calculated according to Eurocode 2 (2004) does not change. Since the reinforcement class is fixed in the reinforced concrete beams, the plastic rotation capacity value can still be calculated as constant. The change in the tensile reinforcement ratio, compression reinforcement ratio, and concrete compressive strength in the RC beams affects the plastic rotation values due to their effect on the neutral axis depth in the sections. As can be seen from the comparison of the results obtained, the plastic rotation values calculated according to the values obtained from the nonlinear behaviors are affected by all the design parameters. The values calculated according to Eurocode 2 (2004) or Model Code (2010) are greatly affected by the neutral axis depth and effective depth of a cross-section.

5.3 Curvature Ductility Obtained from the Moment-Curvature

Fig. 8 shows the relation of the curvature ductility (μ_φ) for the doubly-reinforced beam sections with different compression reinforcement ratios and concrete compressive strengths. In the RC beams, with the increase in the compressive reinforcement ratio for the concrete's constant compressive strength and tensile reinforcement ratio, the curvature ductility values calculated from the moment-curvature relationships increase. Under the same tensile and compression reinforcement ratios, the curvature ductility almost linearly decreases with the increased concrete compressive strength. This indicates that the ductility of the doubly-reinforced beam sections increases with an increase in the compressive reinforcement ratios. The compression reinforcement ratio in the section of a doubly-reinforced beam has certain effects on the moment-curvature relations and ductility of the RC beam sections.

5.4 Derivation of an Alternative Curvature Ductility Equation for a Doubly-Reinforced Beam

From the results of the numerical analyses, the essential factors influencing the ductility of doubly-reinforced beams are f_{ck}, ρ and ρ'. In the doubly-reinforced beams, the effect of f_{ck} has been found to be dependent on the amounts of ρ and ρ', which determine the degree of reinforcement ($\lambda = (\rho - \rho')/\rho_b$) of the section. Thus, based on the numerical analyses results, it can be observed that the use of the two significant variables λ and f_c should be incorporated to develop an alternative equation for the curvature ductility of doubly-reinforced beam sections. The basic formation of the curvature ductility factor equation for doubly-reinforced beams can be expressed as follows:

$$\mu_\varphi = f\left\{\left(\lambda = \frac{(\rho - \rho')}{\rho_b}\right), f_{ck}\right\} \tag{9}$$

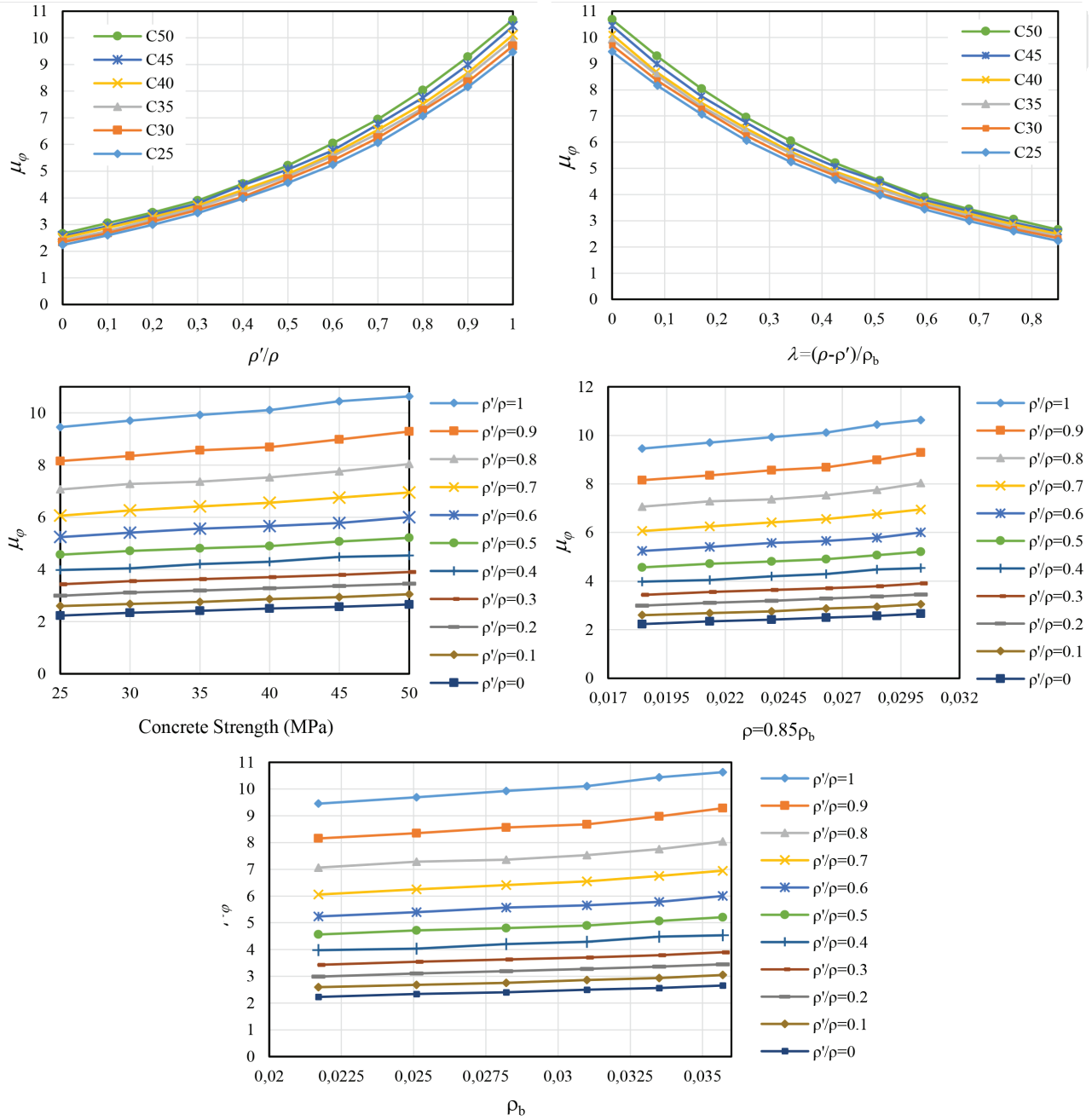

Fig. 8 *Effect of different parameters on the curvature ductility*

The results of the numerical analyses for f_{yk} = 420 MPa, f_{yk} = 25MPa to 50MPa, and ρ'/ρ= 0 to 1 indicate that the curvature ductility increases as ρ'/ρ increases for the doubly-reinforced beam sections. The curvature ductility decreases as λ increases for the doubly-reinforced beam sections. A regression analysis is undertaken to identify the effect of λ on the curvature ductility using the results of the numerical analyses. The effect of λ on the curvature ductility is illustrated in Fig. 9, which shows that the proposed equation closely matches the numerical results of the curvature ductility. The λ has a pronounced effect on the curvature ductility. The results of the numerical analyses show that the curvature ductility decreases with an increase in λ, though not proportionally. Based on the numerical analysis results, the relations of the curvature ductility factor and parameter λ can be obtained by regression analysis as follows:

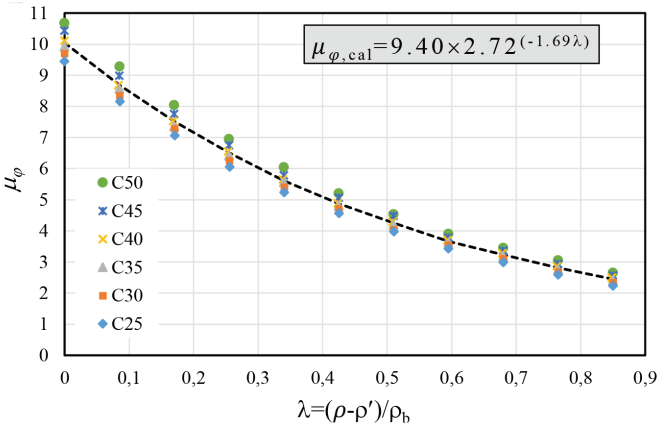

Fig. 9 *Effect of parameter λ on the curvature ductility factor*

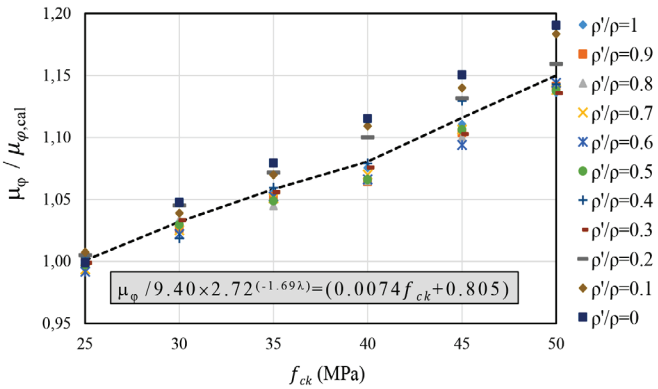

Fig. 10 *Effect of f_{ck} on the ratio of curvature ductility factor to* $9.40 \times 2.72^{(-1.69\lambda)}$

$$\mu_{\varphi,cal} = 9.40 \times 2.72^{(-1.69\lambda)} \tag{10}$$

Equation (10) clearly shows that the curvature ductility factor of doubly-reinforced beam sections can be expressed as a function of $9.40 \times 2.72^{(-1.69\lambda)}$. The effect of the concrete's compressive strength on the ratio of the curvature ductility factor μ_{φ} to $9.40 \times 2.72^{(-1.69\lambda)}$ is shown in Fig. 10. The numerical analysis results indicate that the curvature ductility factor increases with the increase in the concrete's compressive strength. Through regression analysis, the relationship between the ratio of the curvature ductility factor μ_{φ} to $9.40 \times 2.72^{(-1.69\lambda)}$ and the compression strength of the concrete and reinforcement can be obtained as follows:

$$\frac{\mu_{\varphi}}{\mu_{\varphi,cal}} = \left(0.0074 f_{ck} + 0.80\right) \tag{11}$$

Considering the effect of parameters such as the material strength and reinforcement ratio, the predictive equation of the curvature ductility factor in the doubly-reinforced beam sections can be offered based on the parametric study. The proposed curvature ductility ($\mu_{\varphi,prop}$) can be expressed as Equation (12). The effect of f_{ck}, ρ'/ρ and λ on the ratio of the curvature ductility factor $\mu_{\varphi,prop}$ is given in Fig. 11.

$$\mu_{\varphi,prop} = \left[9.40 \times 2.72^{(-1.69\lambda)} \times \left(0.0074 f_{ck} + 0.80\right)\right] \tag{12}$$

5.5 Verification of the Proposed Predictive Equation for the Curvature Ductility Factor

In this part of the study, the flexural ductility of doubly-reinforced beam models designed with different concrete strengths and compression and tensile strength ratios according to the relations by the proposed curvature ductility equation (Equation 12) was calculated analytically. A comparison of the curvature ductility provided by the proposed Equation (12) with the numerical analysis results for the various f_{ck}, ρ'/ρ and λ is given in Fig. 12. Fig. 13 shows a comparison of the curvature ductility factors obtained numerically with the proposed equation. The proposed predictions show excellent agreement as evident from the correlative coefficient R^2, which is well above 0.99. Also, the maximum mean value and the standard deviation for the ratio of the proposed curvature ductility factor obtained by Equation (12) to the numerical results are 1.02 and %2.139, respectively.

When examining the ratio of the results obtained from Equation (12) to the numerical results effected by the changes in f_{ck}, ρ'/ρ and λ, it can be seen that the proposed predictions agree well with the numerical results within all the ranges of the parameters. The discrepancy between the numerical results and the results obtained from Equation (12) increases with the increasing f_{ck} and ρ'/ρ ratios and decreases with the increasing λ ratios. The curvature ductility obtained from the moment-curvature relations, the Kwan et al. (2002) equation, the Lee (2013) equation, the Pam et al. (2001a) equation, the Kwan and Ho (2010) equation, and the proposed predictive equation for the curvature ductility have been compared with the results of the numerical analyses. The relationship of the ductility factor variations with the degree of reinforcement and confining compression are given in Fig. 14. Fig. 15 shows the relations of the ductility factor variations with the ρ'/ρ and concrete strength.

According to the results obtained from the relations proposed for the curvature factor by Pam et al. (2001a) and Kwan et al. (2002), it can be seen that at a given concrete compressive strength, the ductility factor decreases with the tensile reinforcement ratio but increases with the compression reinforcement ratio. For constant ρ'/ρ, as the concrete's compression strength increases, the ductility decreases. The ductility factor values calculated according to the minimum ductility factor specified by Kwan et al. (2002)

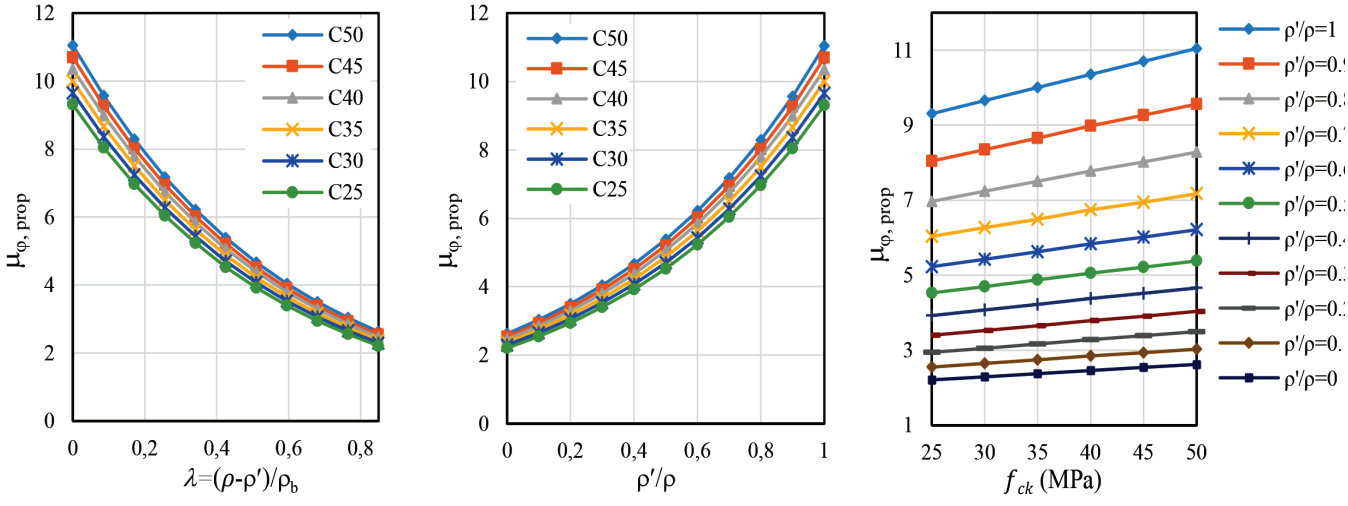

Fig. 11 *Effect of f_{ck}, ρ'/ρ and λ on the ratio of the curvature ductility factor $\mu_{\varphi,pop}$*

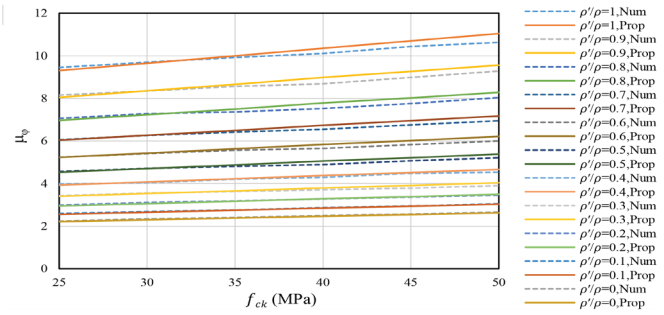

Fig. 12 *Comparison of the curvature ductility for the proposed Equation (12) with the numerical analysis results for the various* f_{ck}*,* ρ'/ρ*, and* λ*.*

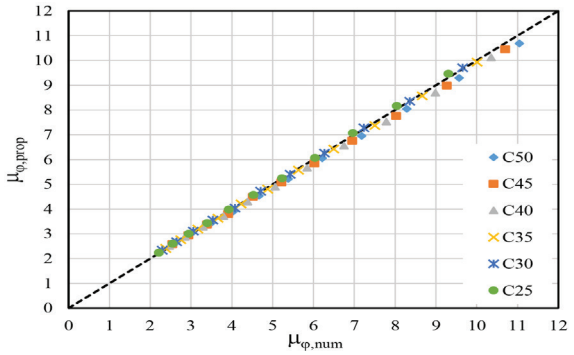

Fig. 13 *Comparison of predicting the* $\mu_{\varphi,prop}$ *and numerical results*

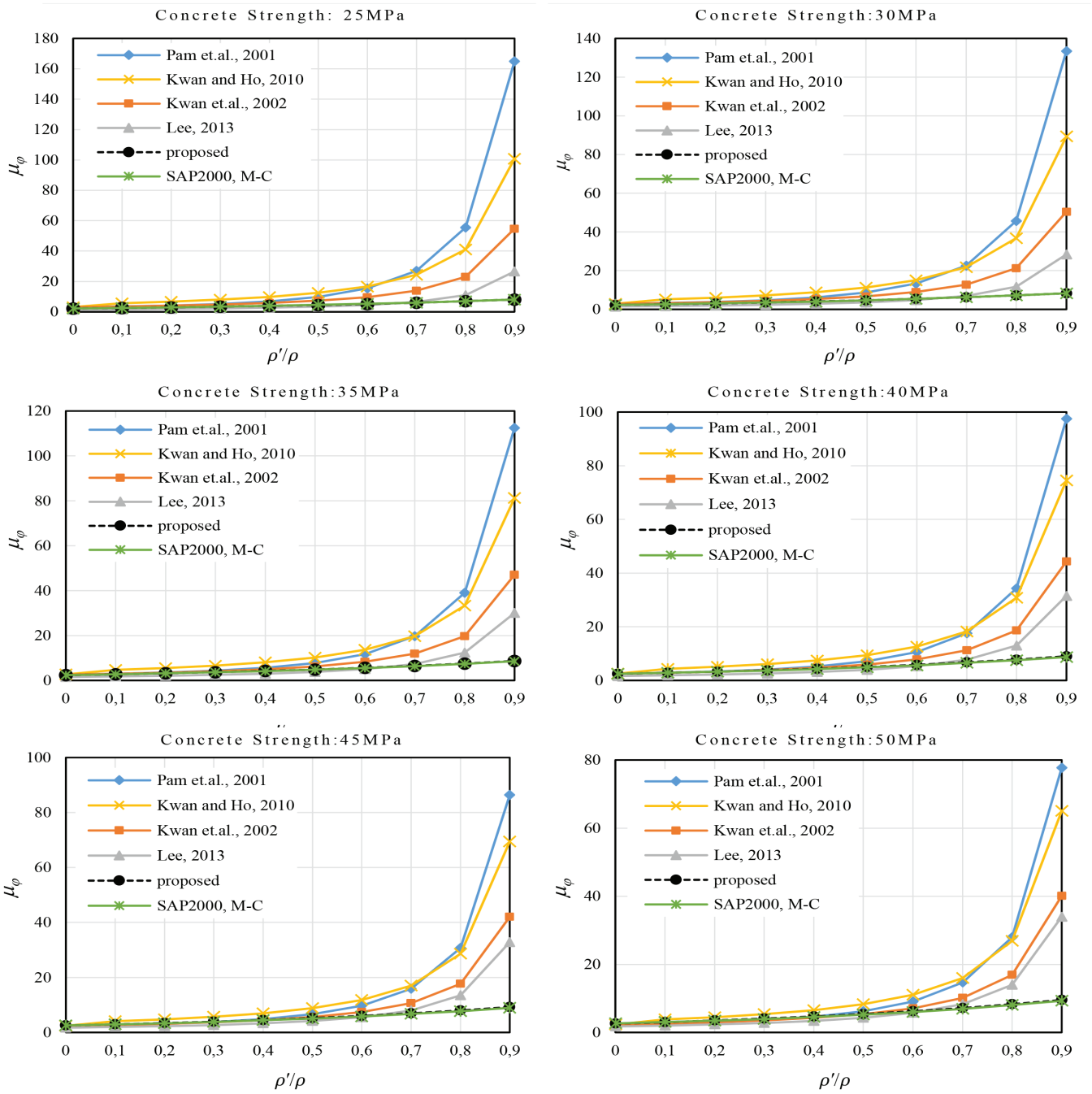

Fig. 14 *Ductility factor* (μ_{φ}) *of the doubly-reinforced beam sections versus the compression reinforcement ratio* (ρ'/ρ)

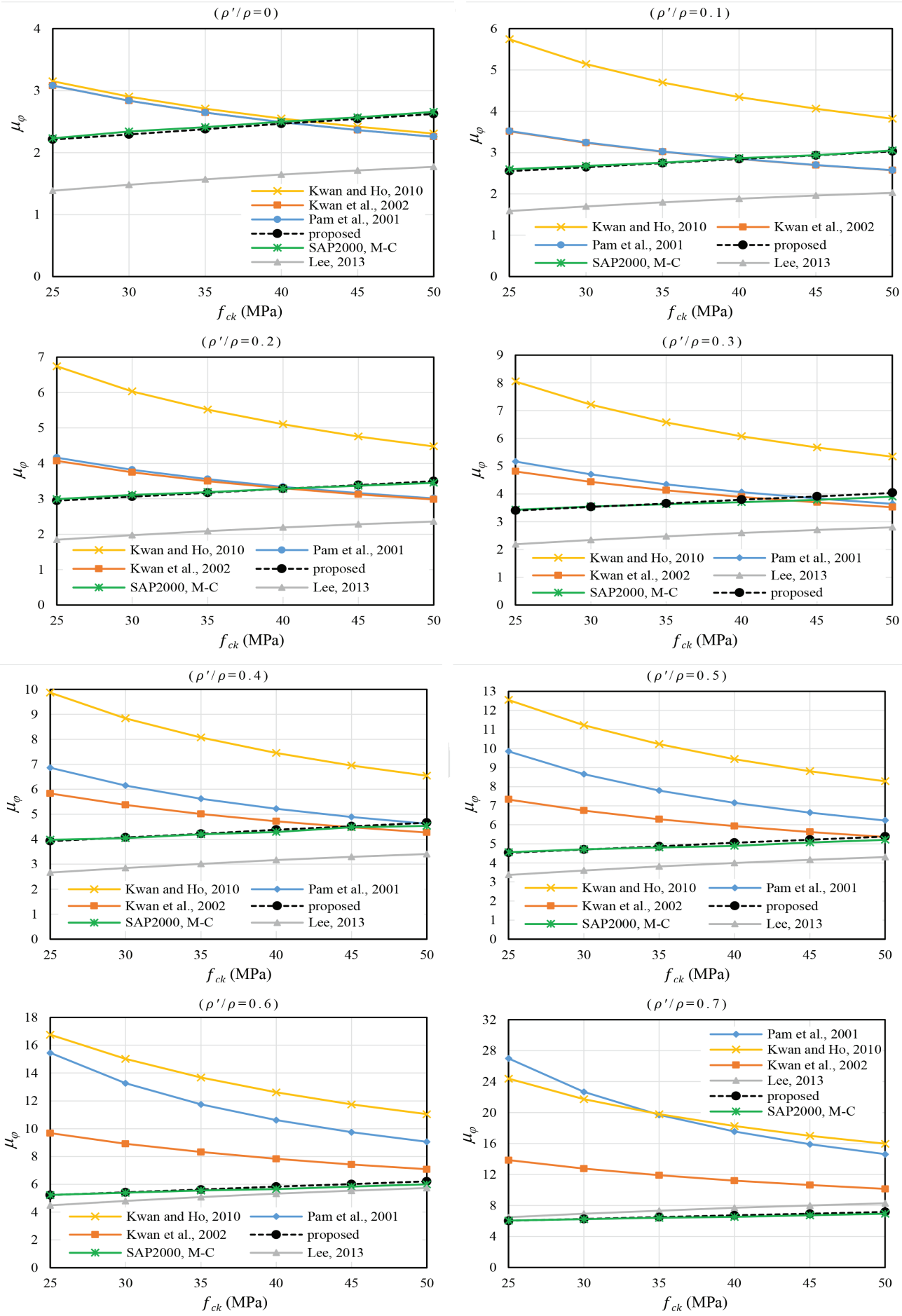
(ρ′/ρ=0)
(ρ′/ρ=0.1)
(ρ′/ρ=0.2)
(ρ′/ρ=0.3)
(ρ′/ρ=0.4)
(ρ′/ρ=0.5)
(ρ′/ρ=0.6)
(ρ′/ρ=0.7)
μφ
fck (MPa)
Kwan and Ho, 2010
Kwan et al., 2002
Pam et al., 2001
proposed
SAP2000, M-C
Lee, 2013

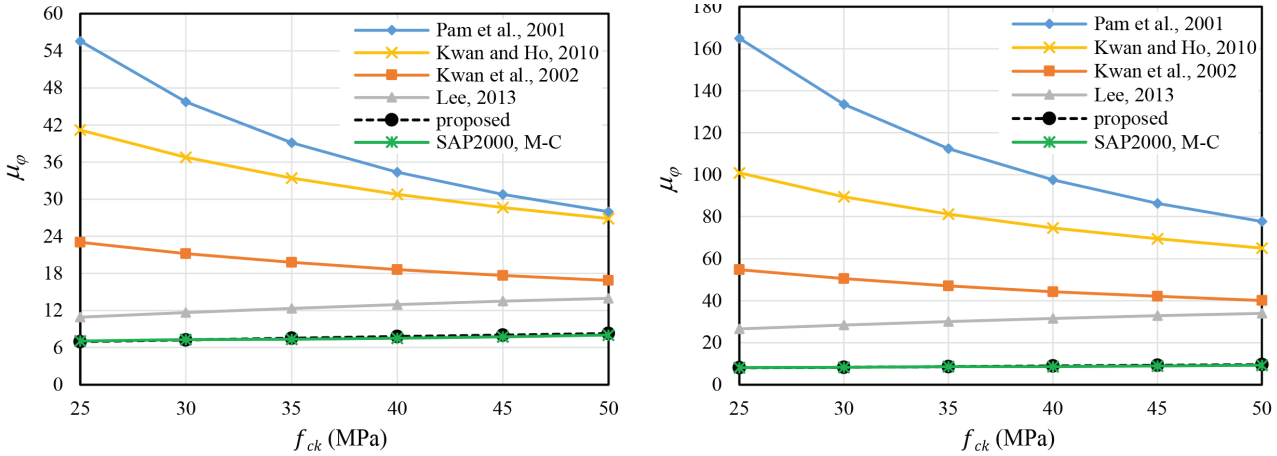

Fig. 15 *Ductility factor (μ_φ) of the doubly-reinforced beam sections versus the concrete's compression strength*

yield small values according to the Pam et al. (2001a) equation. This is because the second term of the equation proposed by Pam et al. (2001a) is taken as 1.0. From the analysis of the results obtained from the relations proposed for the curvature factor proposed by Kwan and Ho (2010), the effect of the concrete's compressive strength has been found to be dependent on the ratios of the tensile and compression reinforcement, which determine the degree of reinforcement of the RC beams. It can be seen that as the concrete's compressive strength or tensile reinforcement ratio increases, the ductility decreases until it reaches a relatively low and constant value when the section becomes overly reinforced. It can also be seen that at the same degree of reinforcement (λ=0), the ductility factor is lower at a higher concrete strength. This is because of the gradual reduction in material ductility as the concrete's compressive strength increases. However, at the same tensile reinforcement ratio, the ductility factor is lower at a higher concrete strength. The concrete's compressive strength increases, and the balanced reinforcement ratios also increase, thereby leading to a decrease in the degree of reinforcement and an increase in the ductility factor. From an analysis of the results obtained from the relations proposed for the curvature factor by Lee (2013), the curvature ductility factor in doubly-reinforced beam sections may be affected by the tensile reinforcement ratio, the compression reinforcement ratio, and the concrete's strength. This indicates that the ductility factor of doubly-reinforced beam sections increases with an increase in the compressive steel ratio. Under the same tensile reinforcement ratio, the ductility factor almost linearly decreases with the increase in the concrete's strength. The curvature ductility factor decreases with increasing λ ratios. It can be seen that the compression reinforcement ratio is the most effective factor. The effect of the concrete's strength and λ on the ratio of the curvature ductility factor $\mu_{\varphi,\text{prop}}$ according to the proposed predictive equation for curvature ductility is given in Figs. 12 and 13. The results of the analyses indicate that the curvature ductility decreases as λ increases for the doubly-reinforced beam sections. The curvature ductility increases as ρ'/ρ increases for the doubly-reinforced beam sections. The ductility increases with the increasing of the concrete's compressive strength concrete. The discrepancy between the numerical results and the results obtained from Equation (12) increases for the increase of f_{ck} and ρ'/ρ. The inconsistency between the results obtained from Equation (12) increases with the decreasing λ value. From a comparison of all the numerical results, almost the same curvature ductility values are obtained from the moment- curvature relations and the proposed equation (Equation 12).

For the ductility factor, f_{ck}, ρ, ρ' and ρ_b were considered as the main factors of the relations proposed by different researchers. In addition to these parameters, some researchers have taken into account the parameters of the stress of the compression reinforcement, the reinforcement yield strength, and the confining compression. In the relations suggested by the researchers, the limit values considered for the parameters are different. The parameters considered in the relations between Pam et al. (2001a) and Kwan et al. (2002) are the same, but the Kwan et al. (2002) relation suggested an economical formula to achieve the required ductility by modifying the Pam et al. (2001a) relation. Accordingly, it is natural that the values obtained for the two models are different. As can be seen from the results of the analysis, the values obtained from the Pam et al. (2001a) relation are higher than the value obtained from the Kwan et al. (2002) relation. The relationships proposed by the different researchers can be calculated up to $\rho'/\rho = 0.9$. In this study, $\rho'/\rho = 0$ to $\rho'/\rho = 1$ has been taken into consideration, but other researchers have considered $\rho'/\rho = 0.75$ in their relations.

6 CONCLUSION

The flexural ductility of different parameters of concrete beams has been studied extensively by parametric studies according to the ductility factor relation suggested by various researchers and using a nonlinear moment-curvature analysis. They have proposed different relations for the ductility factor, which were discussed in detail in the Research Findings and Discussion Section, where the results obtained from these relations differ from each other. The results are different because the various researchers use factors such as different regulations, different material properties, different parameters, and different limit values for the tensile and compression reinforcement ratios. Based on the results of the numerical analyses, a simple equation is proposed for the prediction of the curvature ductility considering λ and the concrete's compressive strength. The proposed predictive Equation (12) is derived based on the results of sections with the concrete's strength (f_{ck}) from 25MPa to 50MPa, the steel's yield strength f_y =420 MPa, the tensile reinforcement ratio from $\rho = 0.85\rho_b$, and the compression reinforcement ratio from $\rho' = 0$ to $\rho' = \rho$. The proposed predictions show excellent agreement as evident from the correlative coefficients R^2, which is well above 0.99. Also, the maximum mean value and the standard deviation

for the ratio of the proposed curvature ductility factor obtained by Equation (12) to the numerical results are 1.0% and 2.1%, respectively. Based on the results of the numerical analysis, the proposed predictions for the curvature ductility factor, considering the concrete's strength and degree of reinforcement, is accurate to within an error of 2.19% for practical applications. The proposed formula was verified by comparisons of its predictions with the numerical results and other predictions. The proposed formula offers fairly accurate and consistent predictions of the curvature ductility factor for doubly-reinforced beam sections. The curvature ductility can be conveniently and simply predicted using the proposed Equation (12).

REFERENCES

Adari, M. P. (2017) *Influence of Curvature Ductility on Reinforced Concrete Beams under the Effect of Confinement*. International Journal for Research in Applied Science and Engineering Technology, 5, 246-255.

Au, F.- Leung, C. C. Y. - Kwan, A. (2011) *Flexural ductility and deformability of reinforced and prestressed concrete sections.* Computers and Concrete, 8, 473-489.

Arslan, G. - Cihanli, E. (2010) *Curvature ductility prediction of reinforced high-strength concrete beam sections*. Journal of Civil Engineering and Management, 16, 462–470.

Bai, B. Z. Z. - Au, F. (2011) *Flexural ductility design of high-strength concrete beams*. The Structural Design of Tall Special Buildings, 22, 521-542.

CEB-FIP. (2010) Fib Model Code for Concrete Structures.

Debernardi, P. G. - Taliano, M. (2002) *On evaluation of rotation capacity for reinforced concrete beams*. ACI Structural Journal, 99, 360-368.

Dhakal, S. - Moustafa, M. (2019) *Moment–curvature analysis for beams with advanced materials*, Software X, 9, 175-182.

Eurocode 2. (2004) Design of Concrete Structures - Part 1: General Rules and Rules for Buildings, Brussels, EN 1992-1-1 (2004).

Jang, I. Y.- Park, H. G. - Kim, S. S. (2008) *On the ductility of high-strength concrete beams.* International Journal of Computing Science and Mathematics, 2, 115-122.

Haytham, B. - Amar, K. (2017) *Curvature Ductility of High Strength Concrete Beams.* Journal of Materials and Engineering Structures, 4, 155-167.

Ho, J. C. M.- Kwan, A. - Pam, H. J. (2004) *Minimum flexural ductility design of high strength concrete beams*. Magazine of Concrete Research, 56, 13-22.

Kwan, A. - Ho, J. C. M. (2010) *Ductility design of high-strength concrete beams and columns*, Advances in Structural Engineering, 13, 651-664.

Kwan, A. K. H.- Ho, J. C. M. - Pam, H. J. (2002) *Flexural strength and ductility of reinforced concrete beams*. Proceedings of the Institution of Civil Engineers - Structures and Buildings, 152, 361-369.

Liew, A.- Gardner, L. - Block, P. (2017) *Moment-Curvature-Thrust Relationships for Beam- Columns*, Structures, 11, 146-154.

Lee, H. J. (2013) *Predictions of curvature ductility factor of doubly-reinforced concrete beams with high strength materials*. Computers and Concrete, 16, 831-850.

Lam, J. Y. K.- Ho, J. C. M. - Kwan, A. (2009a) *Maximum axial load level and minimum confinement for limited ductility design of concrete columns*. Computers and Concrete, 6, 357-376.

Lam, J. Y. K.- Ho, J. C. M. - Kwan, A. K. H. (2009b) *Flexural ductility of high-strength concrete columns with minimal confinement*, Materials and Structures, 42, 909-921.

Pam, H. J.- Kwan, A. - Ho, J. C. M. (2001a) *Post-peak behavior and flexural ductility of doubly-reinforced normal- and high-strength concrete beams.* Structural Engineering and Mechanics, 12, 459-474.

Pam, H. J.- Kwan, A. - Islam, M. S. (2001b) *Flexural strength and ductility of reinforced normal- and high-strength concrete beams.* Proceedings, Institution of Civil Engineers, Structures and Buildings, 146, 381-389.

Pecce, M. - Fabbrocino, G. (1999) *Plastic rotation capacity of beams in normal and high- performance concrete*. ACI Structural Journal, 96, 290-296.

Park, R. - Paulay, T. (1975) *Reinforced Concrete Structures*. Wiley, NY, U.S.A: 800, 1975.

Rashid, M. A. - Mansur, M. A. (2005) *Reinforced high-strength concrete beams in flexure*, ACI Structural Journal, 102, 462-471.

Simão, P. D.- Barros, H. - Ferreira, C. C. (2016) *Losed-form moment-curvature relations for reinforced concrete cross sections under bending moment and axial force.* Engineering Structures, 129, 67-80.

SAP2000. Structural Software for Analysis and Design. Computers and Structures, Inc, USA.

TBEC. (2018) Specifications for Building Design Under Earthquake Effects. Turkish Building Earthquake Code, Ministry of Public Works and Housing, Ankara.

TS500. (2000) Requirements for Design and Construction of Reinforced Concrete Structures", Turkish Standards Institute, Ankara, Turkey.

Zareef, M. A. E. - Madawy, M. E. E. (2018) *Effect of glass-fiber rods on the ductile behavior of reinforced concrete beams*. Alexandria Engineering Journal, 57, 4071-4079.

sciendo

Slovak Journal of Civil Engineering

Vol. 30, 2022, No. 1, 21 – 32
DOI: 10.2478/sjce-2022-0003

THEORETICAL CORRELATIONS BETWEEN THE CUMULATIVE ABSOLUTE VELOCITY AND PERFORMANCE POINT FOR A SEISMIC ANALYSIS OF FRAMED STRUCTURES

KAHIL Amar[1*], HANNACHI Naceur Eddine[1], HAMIZI Mohand[1] and MEBARKI Ahmed[2]

Abstract

The present paper investigates the effect of the harmfulness of a potential earthquake on structural and seismic risks. It takes into account the magnitude, epicentral distance, and pseudo depth at the hypocenter as well as the soil classification in order to generate synthetic seismic motions to be considered as signal inputs for a structural seismic analysis. The most typical typology of dwellings and buildings that are widely existing in Algeria, i.e., a reinforced concrete frame structure, is considered for the case study. The results show that the theoretical models developed in this study are able to predict the performance point (spectral displacement) according to the cumulative absolute velocity. They also show that(CAV-S_d) (S_d being the spectral displacement of the performance point defined by a pushover analysis) is slightly influenced by the value of the ultimate displacements of the structures and the soil parameters (shear velocity Vs).

Address

[1*] University Mouloud Mammeri Tizi-Ouzou, Civil Engineering Department, Faculty of Construction Engineering, B.P.17, Tizi-Ouzou, 15000, Algeria.

[2] Paris-Est University, Laboratory of Multi-Scale Modeling and Simulations, MSME UMR 8208 CNRS, 5 bd Descartes, 77454, Marne-la-Vallee, France.

* ***Corresponding author:*** Kahil Amar (amar.kahil@yahoo.com)

Key words

- Artificial motions,
- Pushover,
- Performance,
- Harmfulness of earthquake,
- Cumulative absolute velocity.

1 INTRODUCTION

Many reinforced concrete framed (RCF) structures have shown inadequate capacity during past quakes (ASCE, 2017; Korkmaz et al., 2015). For the sake of the simplified and rapid performance of seismic analyses, it seems worthwhile to investigate the correlation existing between ground displacements (indicators of harmfulness) and the performance point that defines the seismic capacity of RCF.

The harmfulness of a potential earthquake ultimately depends on the intensity of the ground motion. This may concern the peak values of any displacement, velocity or acceleration, the spectral response, or integral parameters such as the Arias intensity (Arias, 1970; Fabio et al., 2021). It corresponds to the ground duration time (Dashti et al., 2010) and the cumulative absolute velocity (CAV), (EPRI,1988).

The correlation between the seismic ground motions and structural damage has been widely investigated in civil engineering (Noura et al., 2017). Consequently, the spectral displacement, which defines the performance point, is considered the key parameter in RCF seismic analysis and estimations of damage (Xia et al., 2014).

Furthermore, an inelastic structural response is found to be strongly correlated with the spectral acceleration of the input signals for specific periods (Shome et al., 1998). However, none of the potential harmfulness of an earthquake or ground motion intensity (GMI) can entirely be considered as being the unique and best governing parameter of a seismic signal. For instance, the CAV has effects during the entire course of the motion that cannot be caught by the peak values of the displacement, velocity or acceleration and the corresponding spectral response. Therefore, the present study will focus on the CAV, whereas RCF damages will be considered as being correctly defined by the performance point on the capacity curve (Du and Wang, 2013).

Capacity curves will be established for a set of six RCF structures with different ductilities that are assumed to be wide enough to match the most commonly existing typologies. For this purpose, artificial earthquakes will be generated by adopting the Sabetta & Pugliese method (Sabetta and Pugliese, 1996). The correlation between the performance point and the CAV will be investigated and modeled.

2 CORRELATION BETWEEN THE CAV AND THE SPECTRAL DISPLACEMENT (SD)

2.1 Cumulative absolute velocity (CAV)

A ground motion intensity measure such as peak ground acceleration (Paul and Vacareanu, 2020) is used for describing the severity of an earthquake's ground motion. A new intensity measure called cumulative absolute velocity (CAV) was proposed (EPRI, 1991). Unlike peak ground acceleration, which only relates to the maximum acceleration of the time history, CAV is dependent on the whole duration. Fig. 1 is a diagram illustrating CAV (Min et al., 2020), and its mathematical expression is as follows:

$$CAV = \int_0^{t_f} |a(t)|\, dt \quad (1)$$

where:

$|a(t)|$ = the absolute motion acceleration [in $m.s^{-2}$]

t_f = duration of the total seismic motion [in s]

The CAV is equivalent to the global absolute momentum carried by a seismic motion. Investigating the possible correlation between the CAV and the structural seismic damage is considered to be a significant issue (Campbell and Bozorgnia, 2010).

The ground motion prediction equation (GMPE) for CAV developed in this paper is based on a multidisciplinary study that was sponsored by the Pacific Earthquake Engineering Research Center (PEER) (Douglas, 2021) to develop next generation attenuation (NGA) relationships for shallow crustal earthquakes in active tectonic regions (Kenneth et al., 2010).

For the present study, the GMPE adapted for CAV corresponds to the attenuation law developed by Sabetta and Pugliese (Sabetta and Pugliese, 1996). The relation given in Equation 2 is the most suitable one for our work for the following reasons:

- The large quantity of data used by Sabetta and Pugliese (generation of non-stationary artificial earthquakes according to an empirical method based on the regression of attenuation relations of a collection of earthquakes measured in Italy with around 95 accelerograms of 17 earthquakes of magnitudes of 4.6 to 6.8).
- The fact that it allows us to include information on the state of the soil (compact and hard soil, deep alluvial deposits, and shallow alluvial deposits).
- Using the magnitude scale (Ms), magnitudes are included in the interval [4.6 to 6.8] and up to distances of 100 km (Sabetta and Pugliese, 1996).

$$\log_{10}(y) = a + bM + c\log_{10}(R^2+h^2)^{1/2} + e_1S_1 + e_2S_2 \pm \sigma \quad (2)$$

with:

a,b,c = constant parameters, where a=0.133, b=0.328 and c = -1;

M = magnitude; R= epicentral distance [in Km]; = standard deviation;

h = pseudo depth at the hypocenter [in m]; it is obtained by a fitting process and results from various effects such as motion near the source and directivity (Joyner and Boore, 1981);

y = motion parameter (pseudo velocity ($m.s^{-1}$));

e_1, e_2 = constant parameters where $e_1 = 0.262$ and, $e_2 = 0.096$;

S_1, S_2 = coefficients of the site classification (see Tab. 1).

Tab .1 *Coefficients of the site classification*

Site classification	Shear velocity Vs (m/s)	S_1	S_2
Compact and hard soil	Vs ≥ 750	0	0
Deep alluvial deposits	360 ≤ Vs ≤ 750	1	0
Shallow alluvial deposits	180 ≤ Vs ≤ 360	0	1

2.2 Database collection of synthetic signals

As the realization of a database of natural earthquakes is a sensitive issue, it was decided to create a database of artificial seismic signals generated by a synthetic method.

2.3 The calculation code

A code developed by Sabetta and Pugliese in 1996 was used to generate the synthetic signals. It is based on the stochastic method; its principle is to build the spectrogram of the simulated signals by analogy with the spectrograms of a natural database.

An existing code was adapted in order to generate synthetic motions, which are considered as signal inputs for structural seismic analysis. Further details about the operational procedure for this synthetic generation can be found in the technical note DEI/SARG/2005-035 (Rey and Berge, 2005).

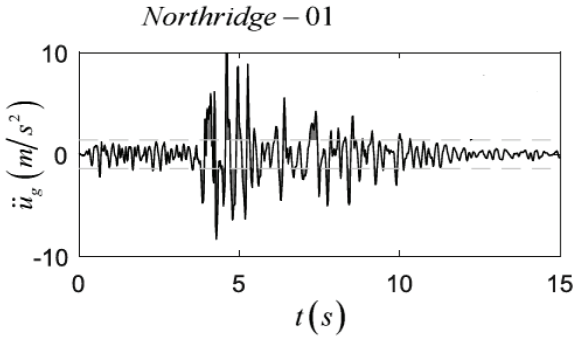

a-Northridge-01 earthquake record

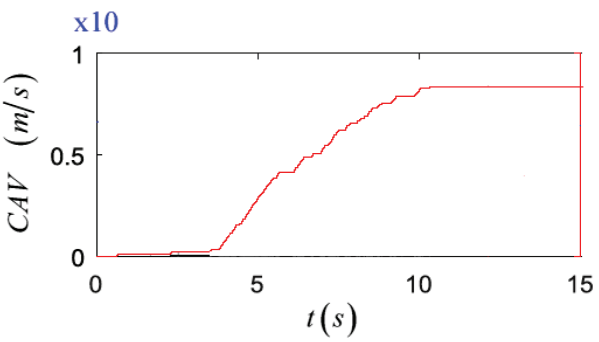

b-Cumulative absolute velocity of the Northridge- 01 earthquake record

Fig. 1 *Example of the cumulative absolute velocity of the Northridge-01 earthquake record (Anastasios and Elias, 2018).*

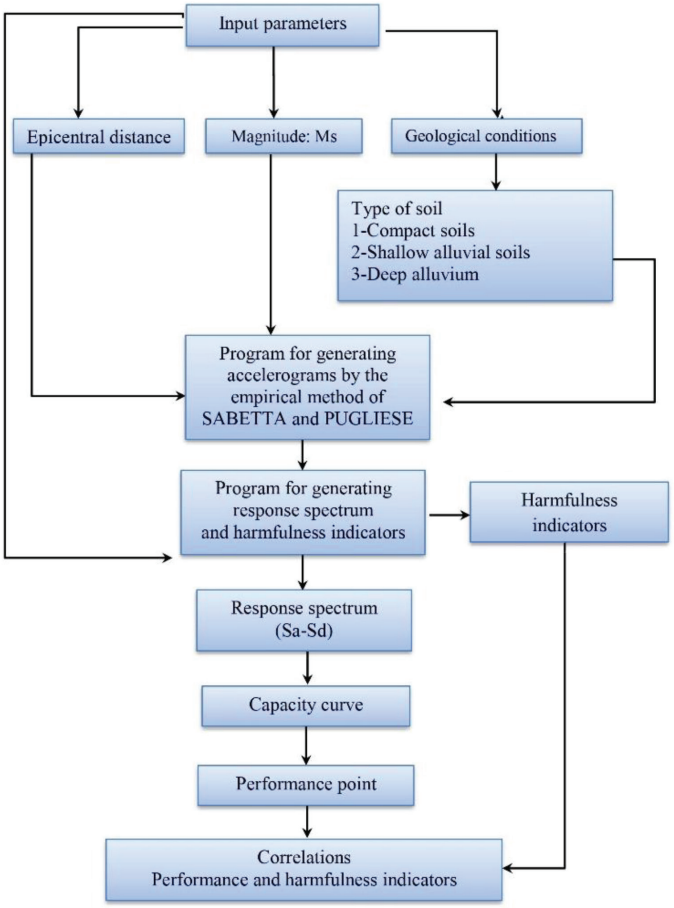

Fig. 2 *Structure of the Matlab procedure followed*

2.4 Matlab procedure

In this article, we present an overview of the Matlab procedure followed (Matlab, 2019). The difficulty in understanding this procedure is related to the fact that the numerical data are extremely numerous and that some classification logic must therefore be kept in mind (Fig. 2).

The program gathers all the procedures and permits, with seven magnitudes for three classes of soils and an epicentral distance, which varies from 0 to 100 Km with a step of 05 Km, to obtain a database of artificial earthquakes of 693 accelerograms.

3 NON-LINEAR STATIC ANALYSIS (PUSHOVER)

A static analysis conducted by progressive monotonic loading (Pushover) has been adopted in order to study the structural response (Melina et al., 2015), i.e., the top lateral displacement according to the shear effort at structure's base (ATC 40, 1996; Chopra and Goel, 1999), whereas the constitutive materials are considered as having non-linear behavior (Lenza et al., 2017).

The static pushover procedure has been widely presented, developed, and investigated over the past forty years (Saiidi and Sozen, 1981; Fajfar, 1999).

This method is also described and recommended as a tool for design and assessment purposes by the U.S. National Earthquake Hazard Reduction Program (NEHRP) (FEMA 273,1997) guidelines, and ASCE 7-16 (ASCE, 2017) for the seismic rehabilitation of existing buildings.

Moreover, the technique is accepted by the Structural Engineer's Association of California (SEAOC) (Rey and Berge, 2005), among other analytic procedures with various levels of complexity.

This procedure has been selected for its applicability to performance-based seismic design approaches, as it can be used at different design levels to verify the performance targets.

Plastic mechanisms and hinges (Fig. 3), as well as plastic adaptation and local damage, can be considered as described in the FEMA 273 guidance document (FEMA 273,1997) and the ACI 318-95 standard (ACI, 1995).

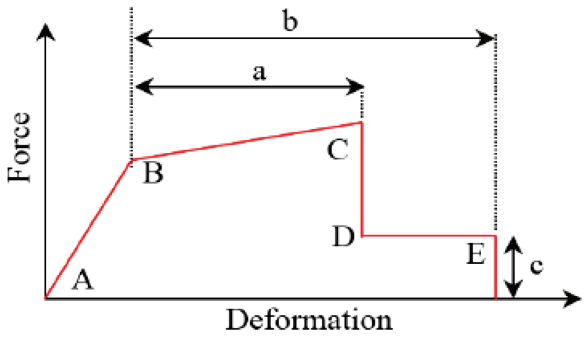

Fig. 3 *Idealized non-linear behavior of beams and columns (FEMA 273, 1997).*

The idealized bi-linear structural behavior described in Fig. 3 starts with the elastic part (branch AB) followed by the branch "BC", the slope values of which typically range within the interval

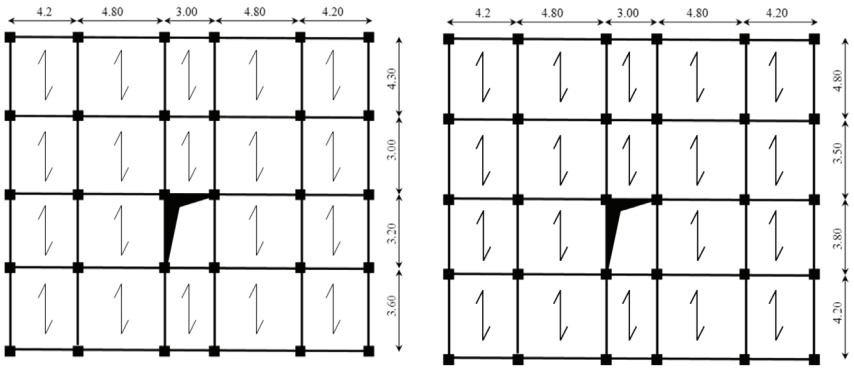

a- Structural models b- Structural models

Fig. 4 *Horizontal layouts, structural components*

0 up to 10% of the initial elastic slope, while ignoring the effects of the gravity loads acting through the lateral displacements.

Point C expresses the maximal carrying capacity of the component, beyond which a significant degradation in strength begins. The parameters 'a' and 'b' refer to the post-yield behavior phases, whereas 'c' expresses the residual bearing capacity in the "CD" branch prior to rupture (FEMA 273,1997).

4 SELECTION OF CASES STUDIED

Typical typologies of some existing Algerian RCF buildings have been selected as the study cases, i.e., 6-storey model buildings (SM_i) with a 3.06 m height (a total height of 18.36 m). The horizontal layouts and cross-sections of the structural components are detailed in Fig. 4 and Tab. 2 respectively. The properties and the behavioral law of the concrete and the reinforcement of the elements are detailed in Tab. 3 and Fig. 5 respectively. They were chosen so that they cover the whole range of expected ductility and semi-ductile behavior.

Tab .2 *Cross-sections and reinforcements*

Structural models	Cross-sections (cm²)		
	Columns	Beams	
		Principal	Secondary
SM_1	30 x 30	30 x 35	25 x 30
SM_2	35 x 35	30 x 35	25 x 30
SM_3	30 x 30	25 x 30	25 x 30
SM_4	35 x 35	25 x 30	25 x 30
SM_5	30 x 30	30 x 35	25 x 30
SM_6	35 x 35	30 x 35	25 x 30
Reinforcements	8HA12 (9.05 cm²)	6HA12 (6.79 cm²)	6HA12 (6.79 cm²)

Tab .3 *Properties of the materials*

Concrete		Reinforcement	
Compression stress (MPa)	Elasticity module (MPa)	Elasticity module (MPa)	Elastic limit (MPa)
25	32164	200000	400

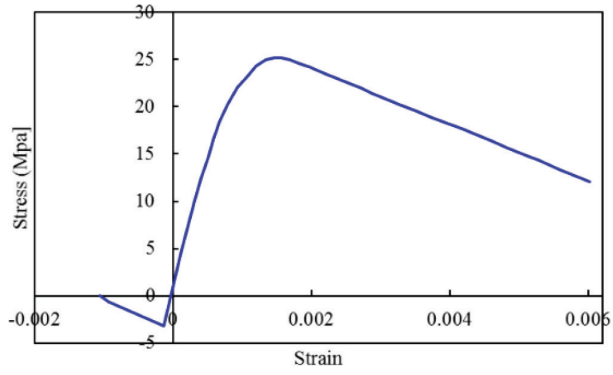

a-Concrete

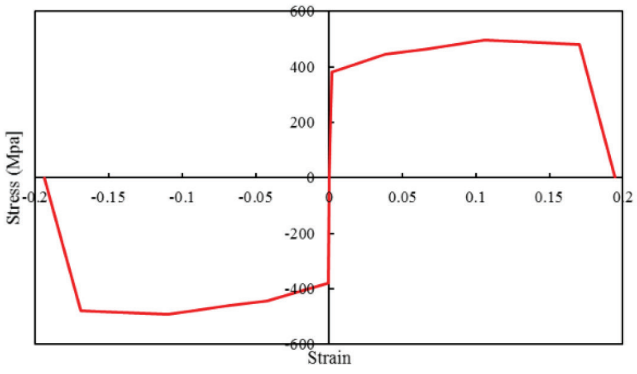

b- Reinforcement

Fig. 5 *Stress-strain curve of the reinforcement and concrete*

4.1 Data assumed for the structures studied

The six RCF buildings studied have the same plan views. The total dead and live loads on the floor slabs are assumed to be 5.1 and 2.5 kN/m², respectively; for the roof slab, they are assumed to be 5.8 and 1.0 kN/m². The frames were designed according to reinforced concrete code BAEL 91 (BAEL, 1992) and the Algerian seismic code RPA99/version2003 (RPA99, 2003), with the following parameters: zone of high seismicity: zone III, importance class group 2, soil type S3 (soft soil), quality factor Q=1, and viscous damping ration ξ=7 %. The analysis will be performed for the zone acceleration factor A=0.25. A seismic behavior factor of R=5 was taken into consideration for RCF without any masonry infill.

4.2 Modeling approach for the inelastic analyses

The analyses were performed using the ETABS program (ETABS 18, 2019), which is a general-purpose structural analysis program for static nonlinear analyses of structures. In this study, the ETABS nonlinear version 18 has been used. A three-dimensional model of each frame structure was created to carry out the nonlinear static analyses. The beam and column elements were modeled as nonlinear frame elements with lumped plasticity by defining plastic hinges at both ends of the beams and columns, where the bilinear moment rotation relationships were assigned (ATC-72-1, 2010).

4.3 Analysis of the pushover results

The pushover analysis consisted of applying monotonically increasing, constant shape lateral load distributions to the structure under consideration. The frame model can be either 2D or 3D. The nonlinear pushover procedure in Eurocode 8 (Eurocode 8, 2003) follows the approach developed by Fajfar (Fajfar, 1999). It considers two load distributions, i.e., a uniform distribution and a modal load distribution.

The two load distributions are shown in Fig. 6. The lateral load distributions applied were increased, and the response was plotted in terms of the base shear versus the top displacement. This is the so-called pushover curve (see Fig. 6).

The pushover curve was then transformed into the response of an equivalent single degree of freedom system (SDOF) (see Fig. 7).

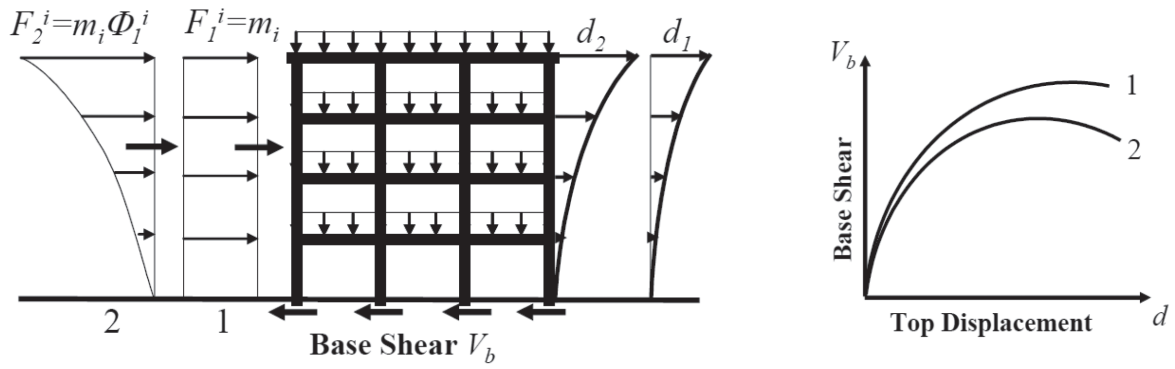

Fig. 6 *Load distributions for the pushover analysis according to Eurocode 8 and the pushover response curves*

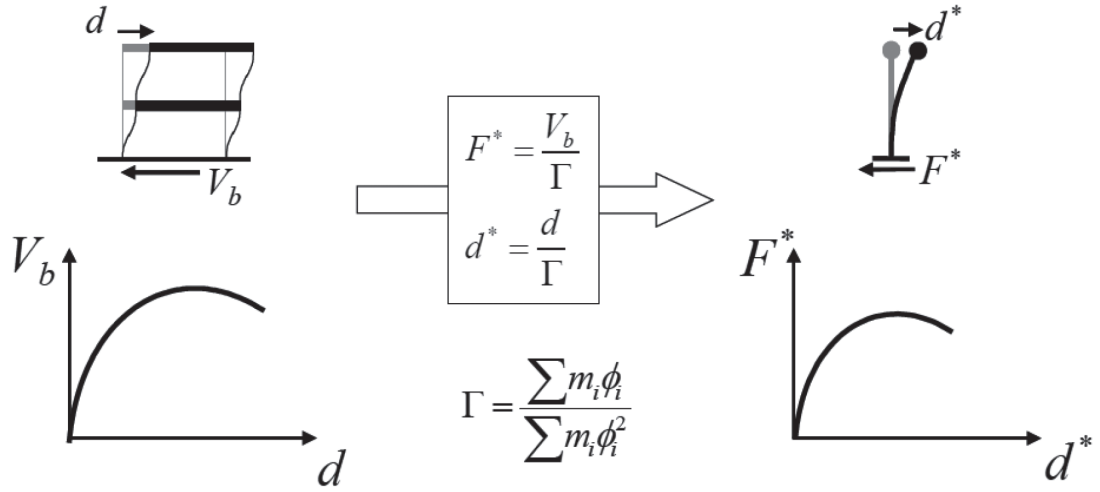

Fig. 7 *Transformation of the pushover curve into the SDOF response*

The capacity curves are classical shear force displacement representations, whereas the spectral capacity curve is derived by applying multipliers (α_1 / w) and 1/(P_{f1}.φ_{1s}) to the shear force V [in KN] and the lateral displacement δ [in m] respectively. Whereas α_1 is the mass modal coefficient, P_{f1} is the first mode participation factor, and φ_{1s} is the top amplitude (Sang et al., 2014; Fawad, 2018).

4.4 Bilinear representation of the capacity curve

The bilinear representation (Fig. 8) of the capacity curve allows us to calculate the elastic and ultimate limits in terms of the acceleration and spectral displacement for arriving at the ductility ratio μ. This defines the ratio between the ultimate lateral displacement and the yield (elastic) lateral displacement.

The equivalent bilinear curve is based on an energy equivalence criterion. For the maximum displacement value $S_{du,}$ the area under the capacity diagram must be equal to that under the bilinear curve; in other words, the areas Ω_1 and Ω_2 are equal (João and Estêvão, 2019).

In Fig. 8, S_{ay} and S_{dy} represent the spectral acceleration and spectral displacement respectively, there by corresponding to the elastic limit (Neeva and Ningthoukhongjam, 2021).

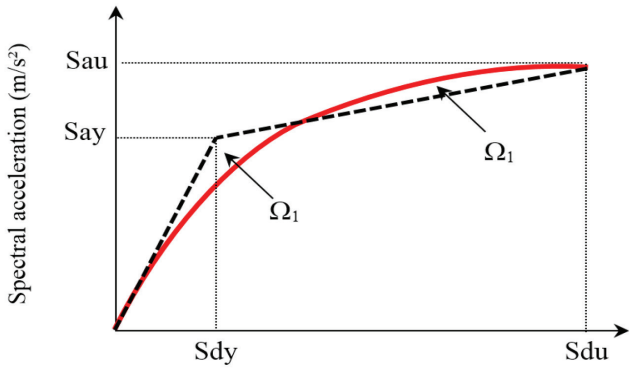

Fig. 8 *Bilinear representation of the capacity curve*

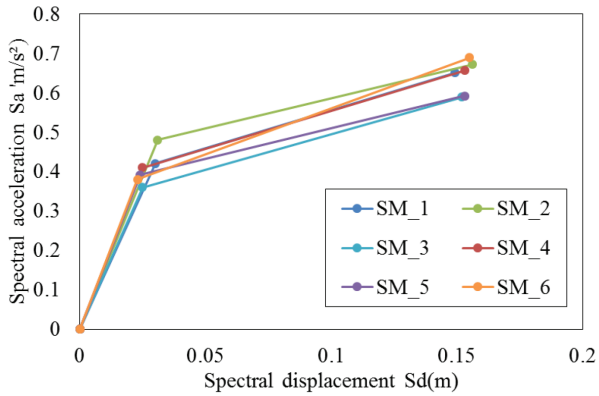

Fig. 9 *Pushover analysis results for the 6 buildings studied.*

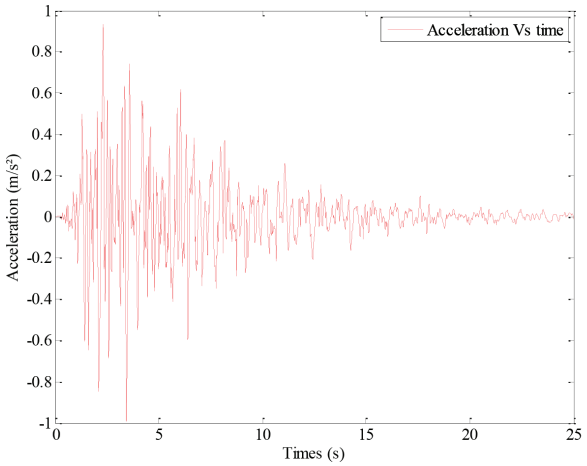

Fig. 10 *Spectral representation of the artificial demand curve.*

The pushover analysis was applied to the structures adopted as study cases (Tab. 4 and Fig. 9), as described above. The ductility factors obtained (Giuseppe et al.,2004; Chikh et al., 2017) are summarized in Tab. 4.

Tab. 4 *Pushover analysis and ductility results for the 6 buildings studied*

Structural models	S_d (m)	S_a (m/s²)	$\mu = \frac{S_{dy}}{S_{du}}$
SM_1	0	0	4.97
	0.03	0.42	
	0.149	0.65	
SM_2	0	0	5.03
	0.031	0.48	
	0.156	0.672	
SM_3	0	0	6.08
	0.025	0.36	
	0.152	0.589	
SM_4	0	0	6.12
	0.025	0.41	
	0.153	0.656	
SM_5	0	0	6.38
	0.024	0.392	
	0.153	0.592	
SM_6	0	0	6.74
	0.023	0.38	
	0.155	0.689	

5 PERFORMANCE POINT

The capacity spectrum method, which is widely adopted and known as acceleration, displacement, and response spectra (ADRS), was used to identify the performance point (Golafshar et al., 2020; Amin et al., 2020). It requires that both the demand curve and capacity curve have spectral representations, see Figs. 10 and 11.

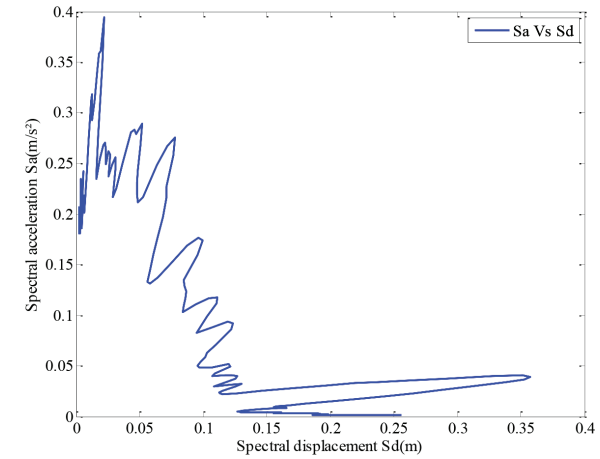

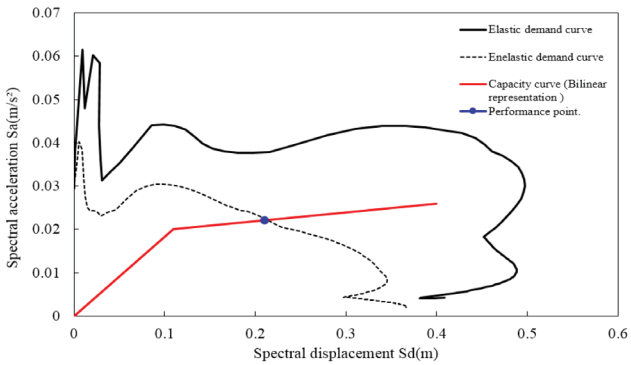

Fig. 11 *Determination of the performance point.*

The seismic demand curve (Fig. 10) was established with a linear elastic response spectrum (Tiziana et al., 2016; Amin et al., 2020). This spectrum was then transformed into an inelastic demand curve, i.e., the so-called reduced spectrum by adopting a damping ratio assumed to be equal to 5% (FEMA 440, 2004). The intersection between the capacity and the demand spectra (Fig. 11) defines the performance point.

6 EFFECT OF THE CUMULATIVE ABSOLUTE VELOCITY (CAV) ON THE PERFORMANCE POINT

The effects of the CAV on the performance point for various soil categories ($180 \leq V_S \leq 360$, $360 \leq VS \leq 750$ and $Vs \geq 750$ m / s (where Vs is the wave velocity, see Tab. 1); was investigated (Fig. 15).

The correlation between the CAV and the spectral displacement S_d is slightly influenced by the ultimate spectral displacement value (S_{du}). However, it is also greatly affected by the soil parameters (see Fig. 15).

The scattering (variability) actually depends on the wave velocity Vs: the larger the velocity, the lower the scattering.

It is therefore challenging to develop a theoretical relationship between the CAV and the spectral displacement at the design point. The results obtained show that the point cloud obtained was approximated by two functions: the first describes the ascending branch, which is similar to the power function, and the second branch is described by a linear function (an asymptote).

6.1 A theoretical relationship between CAV and S_d at the performance point

According to the results observed (Fig. 15), the most adequate relationship seems to be of the general form (see Fig. 12) at its ascending branch, where X is the decimal logarithm of CAV and whereas Y is the spectral displacement at the performance point, 'a' and 'b' being the fitting parameters (Figs. 13 and 14).

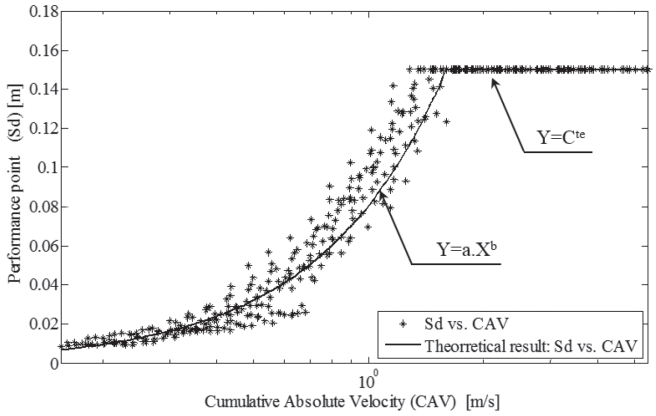

Fig. 12 *General relation between the performance point (spectral displacement) and the CAV.*

6.2 Theoretical (fitted) model and correlation between CAV and S_d

The optimal fitting corresponds to the parameters obtained by:

$$b = \frac{\overline{Ln(S_d).Ln(CAV)} - \overline{Ln(S_d)}.\overline{Ln(CAV)}}{\overline{(Ln(S_d))^2} - \overline{(Ln(S_d))}^2} \quad (3)$$

$$a = e^{\overline{(Ln(CAV)} - b.\overline{Ln(S_d)}} \quad (4)$$

The corresponding linear correlation coefficient between CAV and S_d then becomes:

$$R = \frac{\overline{(Ln(S_d).Ln(CAV)} - \overline{Ln(S_d)}.\overline{Ln(CAV)}}{\sqrt{\left[\overline{Ln(S_d)^2} - \overline{(Ln(S_d))}^2\right].\left[\overline{(Ln(CAV)^2} - \overline{(Ln(CAV))}^2\right]}} \quad (5)$$

In equations 3,4, and 5, 'Ln' is the niparian logarithm.

6.3 Theoretical models to predict the spectral displacement S_d at the performance point vs. CAV

The best fitted theoretical models that predict the spectral displacement S_d at the performance point according to the ductility and the CAV, as well as the threshold CAV_{se}, are summarized in Tabs. 5 to 7, where CAV_{se} is the transition point of the ascending branch and the line defined by the ultimate displacement of the structure.

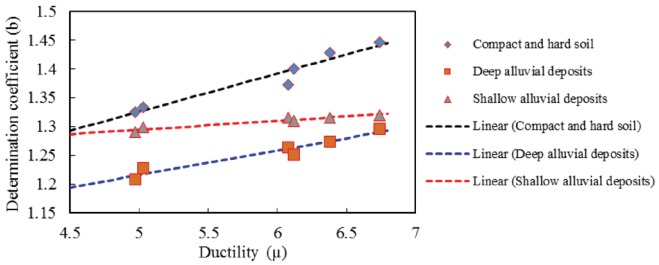

Soil category	Best fitted relationship	Correlation coefficient 'R'
Compact and hard soil	S_d=0.0029 $\log_{10}$(CAV)+0.066	0.96
Shallow alluvial deposits	S_d=0.0426 $\log_{10}$ (CAV)+1.0028	0.96
Deep alluvial deposits	S_d=0.0154 $\log_{10}$ (CAV)+1.2174	0.96

Fig. 13 *Effect of the soil category on the fitting parameters (b coefficient).*

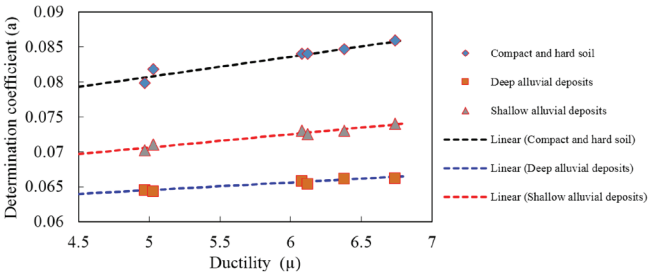

Soil category	Best fitted relationship	Correlation coefficient 'R'
Compact and hard soil	S_d=0.0029 $\log_{10}$(CAV)+0.066	0.96
Shallow alluvial deposits	S_d=0.0011 $\log_{10}$(CAV)+0.059	0.97
Deep alluvial deposits	S_d=0.0019 $\log_{10}$(CAV)+0.061	0.97

Fig. 14 *Effect of the soil category on the fitting parameters (a coefficient).*

6.4 Fitted models and results observed: S_d vs. CAV

The fitted theoretical models ''Spectral displacement S_d at the performance point''vs. "CAV" in Fig. 15 show that these (CAV-S_d) are highly correlated with coefficient R ranging from:

- 0.95 up to 0.96 for compact soil (Vs>750 m/s);
- 0.92 up to 0.98 for shallow and deep alluvial deposits.

Tab .5 *Relationship of the spectral displacement S_d at the performance point vs. CAV: case of deep alluvial deposits*

Deep alluvial deposits ($180 \le V_s \le 360$ m/s)	Ductility (μ)	CAV_{se}
$S_d = \begin{cases} (0.0019\mu + 0.0061)CAV^{(0.0154\mu+1.217)} \\ S_{du} \end{cases}$ $\begin{matrix} \text{if } CAV \le CAV_{se} \\ \text{if } CAV \ge CAV_{se} \end{matrix}\Big\}$	4.97	1.888
	5.03	1.971
	6.08	1.926
	6.12	1.971
	6.38	1.926
	6.74	1.971

Tab .6 *Relationship of the spectral displacement S_d at the performance point vs. CAV: case of shallow alluvial deposits*

Deep alluvial deposits ($180 \le V_s \le 750$ m/s)	Ductility (μ)	CAV_{se}
$S_d = \begin{cases} (0.0019\mu + 0.0061)CAV^{(0.0154\mu+1.217)} \\ S_{du} \end{cases}$ $\begin{matrix} \text{if } CAV \le CAV_{se} \\ \text{if } CAV \ge CAV_{se} \end{matrix}\Big\}$	4.97	2.0482
	5.3	2.0482
	6.8	2.0482
	6.12	2.0482
	6.38	2.0482
	6.74	2.0482

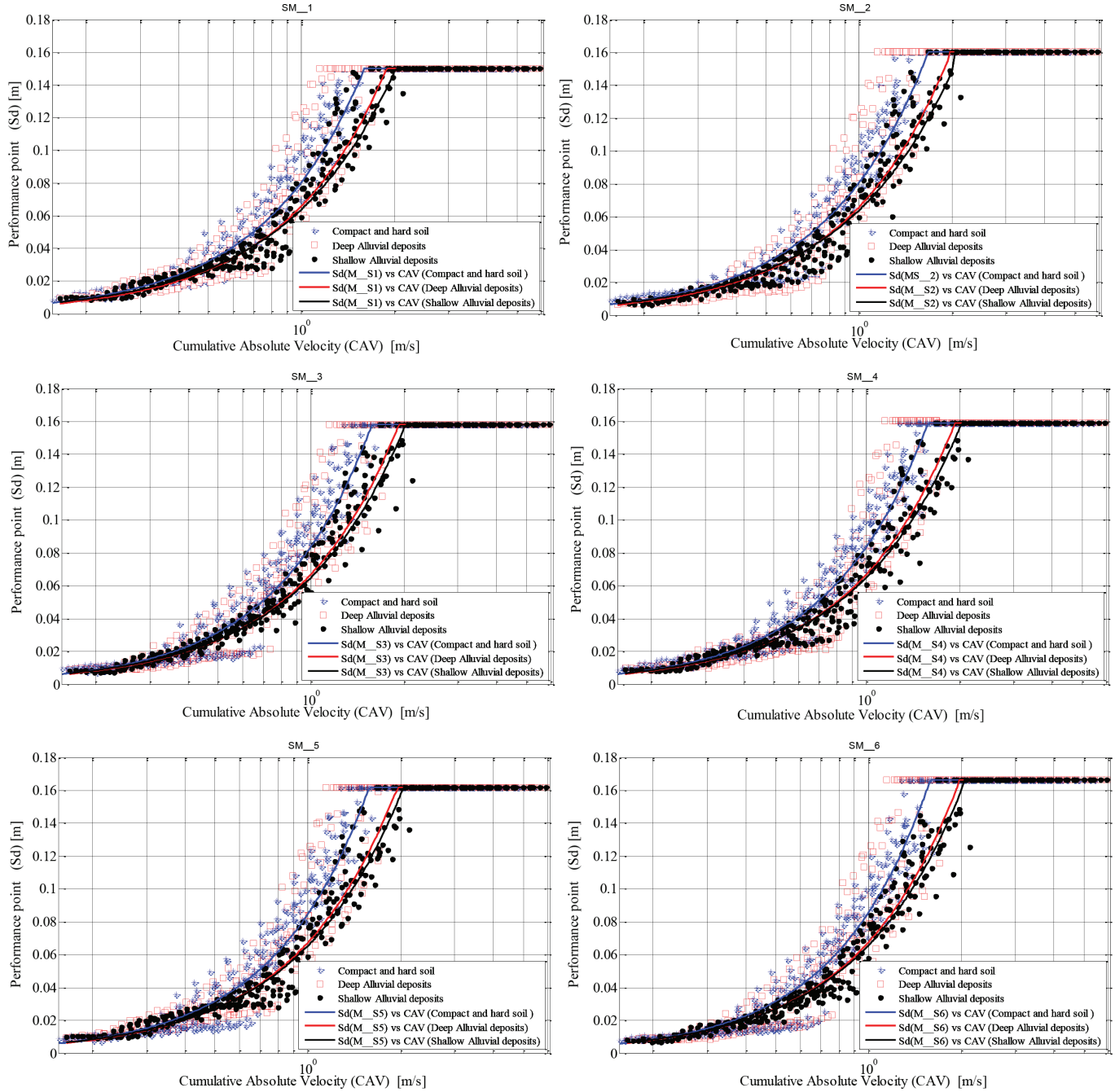

Fig. 15 *Theoretical and observed results: S_d vs. CAV.*

Tab .7 *Relationship of the spectral displacement S_d at the performance point vs. CAV: Case of compact and hard soil*

Compact and hard soil ($V_s \leq 750$ m/s)	Ductility (μ)	CAV_{sc}
$S_d = \begin{cases} (0.0029\mu+0.0662)CAV^{(0.0661\mu+0.9953)} \\ S_{du} \end{cases}$ if $CAV \leq CAV_{sc}$ if $CAV \geq CAV_{sc}$	4.97	1.599
	5.03	1.682
	6.08	1.599
	6.12	1.599
	6.38	1.599
	6.74	1.599

In order to confirm the correlation coefficients R and to ensure that the residues follow a normal distribution, a residual normality test was carried out on the whole model. The residuals were calculated at the point of performance as follows (Fig. 16):

$$\varepsilon = S_{d,model} - S_{d,simulation} \quad (6)$$

The results of the variation of the residuals are shown in Fig. 16, and the maximum and minimum residuals are shown in Figs. 17 and 18.

The results presented in Tabs. 8 and 9 show that there are not too many values outside the interval [(Mean - 2σ): (Mean + 2σ)], where σ is the standard deviation (see Fig. 16), except for the

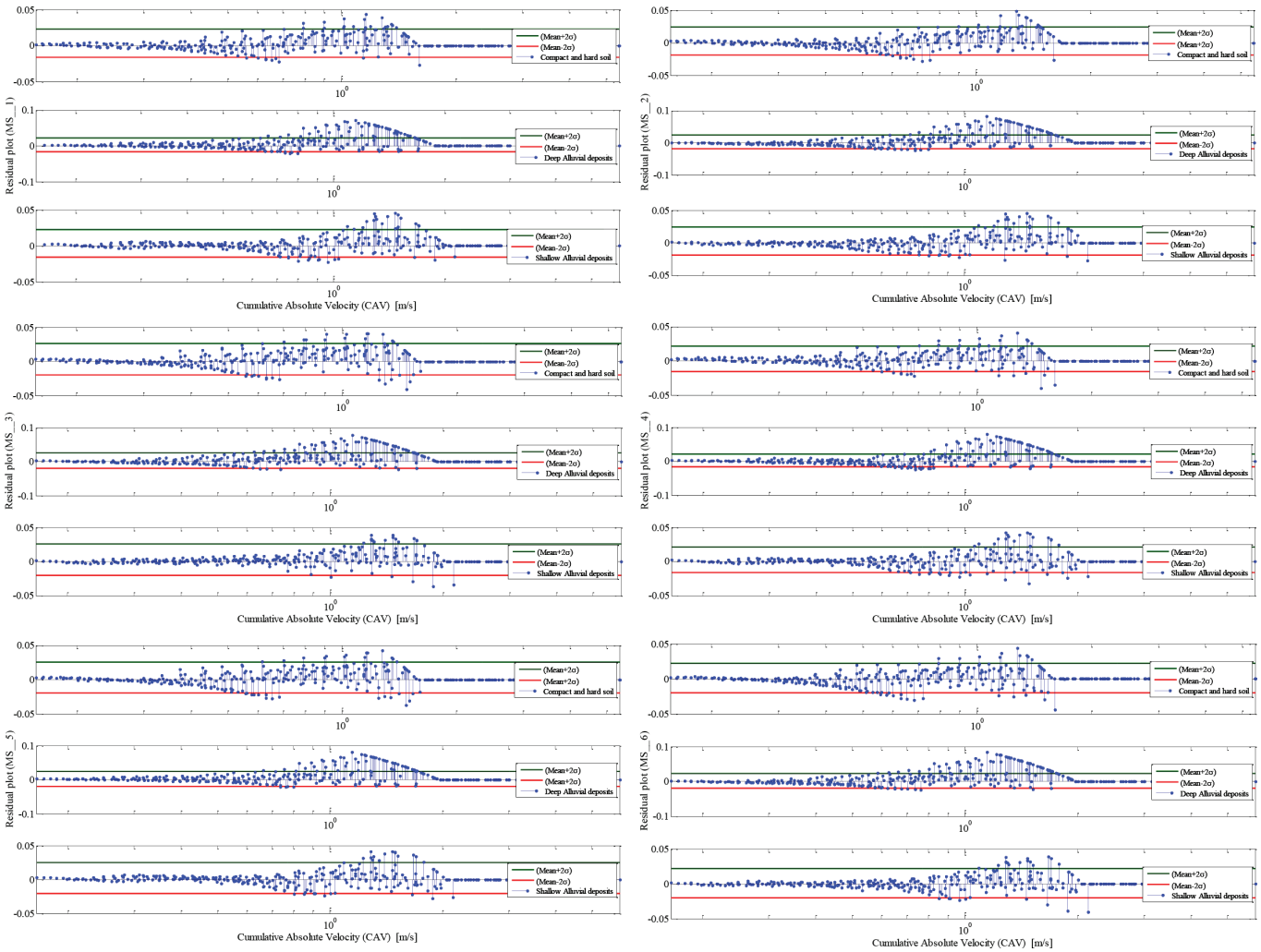

Fig. 16 *Variation of residuals at the performance point according to the CAV*

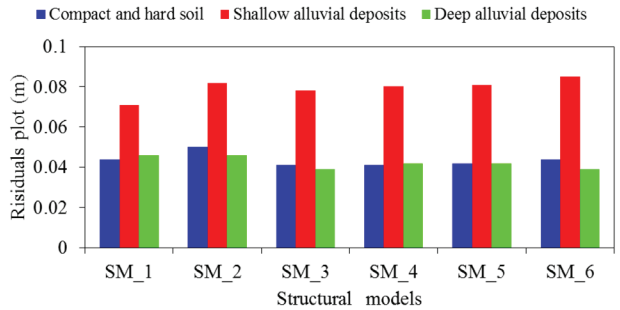

Fig. 17 *Variation of residuals at the performance point according to the CAV.*

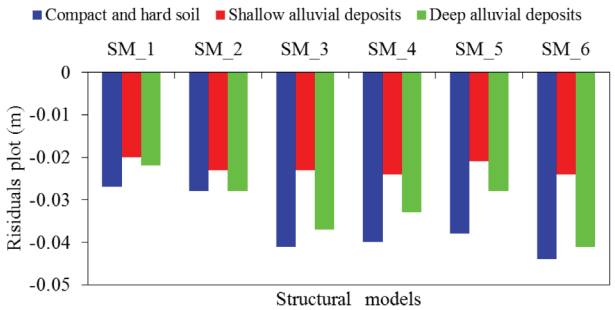

Fig. 18 *Maximum residuals at the performance point: effect of the ductility.*

SM_1 model. The difference between the mean value and the median value must be small; the observed values range from 0.01 to 0.03. It can also be noted that the distribution is symmetrical with the coefficients lying between 0.35 and 0.94, except for the SM_1. Through these test results (a normality test), it can be concluded that the proposed models are quite suitable for structural ductilities having values higher than 5.00.

7 CONCLUSION

This study has proposed a theoretical relationship between the CAV and the structural performance point (S_d). The case studies represent the existing structural typology in Algeria (reinforced concrete frame structures).

This typology of structure is taken into consideration in the present work through its ductility, which is defined by the ratio between the ultimate and elastic displacement. In order to study this typical and dominant typology in Algeria, six classes of ductility were tested numerically, and the capacity curve that reflects their behaviors was established.

In order to find a correlation between the seismic demand and the performance point, the collection of a natural earthquake database is not easy, particularly in the case of Algeria. An artificial earthquake database was created to remedy this lack based on existing mathematical models of seismic attenuation.

The results of the correlation thus obtained show the great influence of the ascending branch and the singular point for which the structural behavior reaches its asymptotic horizontal part defined by the ultimate displacement of each structural model.

The proposed models, which were obtained after adequate fitting, and the observed S_d vs. CAV results, are slightly influenced by the ultimate displacement of the structures, but are strongly influenced by the soil variability (shear velocity 'Vs') and the structural ductility. The correlation coefficient corresponding to the three categories of soils considered is between 0.92 and 0.98.

The models developed in this study allow us to obtain the point of performance of a specific structure by knowing its ductility at a given site (soil) and its shear velocity Vs. For an earthquake characterized by CAV, these models will be of great importance in a study of the large-scale vulnerability of an urban area subject to a lack of natural seismic data.

Acknowledgements

The authors are grateful to the academic institutions (University Mouloud Mammeri of Tizi-Ouzou, Algeria, and University Paris-Est, France) that partly supported the research work and the international scientific exchanges.

Tab .8 *Normality test parameters*

Structural models	Mean	Standard deviation (σ)	Mean - 2σ	Mean + 2σ	Abnormal headcount (lower)	Abnormal headcount (upper)
SM_1	0.003	0.010	-0.016	0.023	8	19
SM_2	0.002	0.011	-0.019	0.024	9	21
SM_3	0.003	0.011	-0.020	0.026	13	15
SM_4	0.002	0.009	-0.016	0.021	11	15
SM_5	0.002	0.011	-0.020	0.025	15	14
SM_6	0.001	0.011	-0.020	0.022	12	10

Tab .9 *Normality test parameters and interpretation*

Structural models	Outsized proportion	Values	Asymmetry	Flattening
SM_1	There are not too many non-standard	0.07	1.07	2.04
			The distribution is not symmetrical	The curve is pointed
SM_2		0.08	0.94	2.69
			Correct	The curve is pointed
SM_3		0.08	0.39	2.28
			Correct	The curve is pointed
SM_4		0.07	0.50	2.85
			Correct	The curve is pointed
SM_5		0.08	0.37	2.04
			Correct	The curve is pointed
SM_6		0.06	0.35	2.19
			Correct	The curve is pointed

REFERENCES

American Concrete Institute (ACI). (1995) *Building code requirements for reinforced concrete.* ACI 318-95, Mechanics and Design, 3d ed. American Concrete Institute, Detroit, MI, U.S.A.

Algerian seismic design code (RPA99/Version 2003). (2003). *National Center of Appliced Research in Earthquake Engineering,* Algeria.

Amin Saleh, A.- Amr Hussein, Z.- Gilane Abdel Hady, R. (2020) *The reliability of capacity designed components in seismic resistant systems,* International Journal of Scientific & Engineering Research, Vol 11, No 11, Nov.2020, ISSN 2229-5518.

Anastasios, I.G.- Elias, G. D. (2018) *In Quest of Optimal Intensity Measures of Rocking Behavior,*16th European Conference on Earthquake Engineering, June 2018.

Arias, A. (1970) *A measure of earthquake intensity. In Seismic Design for Nuclear Power Plants.* R. Hansen, Ed., MIT Press, Cambridge, MA, USA. pp. 438 – 483.

American Society of Civil Engineers (ASCE 7-16). (2017). *Minimum Design Loads for Buildings and Other Structures Commentary.* American Society of Civil Engineers. doi:10.1061/9780784412916.

Applied Technology Council (ATC 40). (1996). *Seismic evaluation and retrofit of concrete buildings.* ATC 40, Redwood City, CA, USA.

Applied Technology Council (ATC-72-1). (2010). *Modeling and acceptance criteria for seismic design and analysis of tall buildings.* Redwood City, CA, USA.

BAEL 91. (1992). *Règles Techniques de Conception et de Calcul des Ouvrages et Constructions en 1992,* **Béton armé suivant la méthode des é**tats limites. Edition Eyrolles.

Campbell, K.- Bozorgnia, Y. (2010) *Analysis of Cumulative Absolute Velocity (CAV) and JMA Instrumental Seismic Intensity (IJMA) Using the PEER-NGA Strong Motion Database.* PEER Report 2010/102. http://peer.berkeley.edu.

Chikh, B. - Mebarki, A. - Laouami, N. - Leblouba, M.- Mehani, Y. -Hadid, M. -Kibboua, A. - Benouar, D. (2017) *Seismic structural demands and inelastic deformation ratios: a theoretical approach.* Earthquake and Structures, 12 (4): 000-000, DOI:https://doi.org/10.12989/eas.2017.12.4.000.

Chopra, AK. - Goel, RK. (1999) *Capacity-demand-diagram methods based on inelastic design spectrum.* Earthquake Spect., 15(4):637–56.

Dashti, S. -Bray, JD. -Pestana, JM. -Riemer, M. - Wilson, D. (2010) Centrifuge *testing to evaluate and mitigate liquefaction-induced building settlement mechanisms.* Journal of geotechnical and geoenvironmental engineering, 136(7): 918–29.

Douglas, J. (2021) *Ground motion prediction equations 19642020,* http://www.gmpe.org.uk.

Du, W. - Wang, G. (2013) *A simple ground-motion prediction model for cumulative absolute velocity and model validation.* Earthquake Engineering Structural Dynamics. 42(8): 1189-1202.

Electrical Power Research Institute (EPRI). (1988). *A criterion for determining exceedance of the operating basis earthquake.* Report No. EPRI NP-5930, Palo Alto, CA, USA, 1988.

Electrical Power Research Institute (EPRI). (1991). *Standardization of Cumulative Absolute Velocity, EPRI Report RP3096- 1,* Electric Power Research Institute, Palo Alto, CA, USA,1991.

ETABS 18. (2019). *Three dimensional static and dynamic finite element analysis and design of structures V18.* Computers and Structures Inc, Berkeley, CA, USA,2019.

Eurocode 8. (2003). *Design of Structures for Earthquake Resistance,* European Committee for Standardization, 2003.

Fabio, S.-Antonio, P. - Gabriele, F.-Giovanni, L.-Lucia, L., (2021) *Simulation of non-stationary stochastic ground motions based on recent Italian earthquakes,* Bulletin of Earthquake Engineering, https://doi.org/10.1007/s10518-021-01077-1.

Fajfar, P. (1999) *Capacity spectrum method based on inelastic demand spectra.* Earthquake Engineering and Structural Dynamics. 28: 979-93.

Fawad, A. N. (2018) *Nonlinear Static Analysis Procedures for Seismic Performance Evaluation of Existing Buildings–Evolution and Issues.* Springer International Publishing AG 2018H. Rodrigues et al. (eds.). Facing the Challenges in Structural Engineering, Sustainable Civil Infrastructures, DOI 10.1007/978-3-319-61914-9_15.

Federal Emergency Management Agency (FEMA 273). (1997). *NEHRP Commentary on the Guidelines for Seismic Rehabilitation of Buildings. FEMA 273 Report, prepared by the Building Seismic Safety,* Council and the Applied Technology Council for the Federal Emergency Management Agency, Washington, D.C, USA.

Federal Emergency Management Agency (FEMA 440). (2004). *Improvement of nonlinear static seismic analysis procedures (draft) (Report ATC and FEMA).* Applied Technology Council (ATC-55 Project) and Federal Emergency Management Agency.

Giuseppe, F. - Aldo G. - Marco M. (2004) *Definition of suitable bilinear pushover curves in nonlinear static analyses,* 13th World Conference on Earthquake Engineering, Vancouver, B.C., Canada Aug. 1-6, 2004, Paper No. 1626.

Golafshar, A. - Saghafi, M. H- Eshaghi, F. (2020) A *New Method for Drawing the Capacity Spectrum for Seismic Analysis and Structural Rehabilitation,* Journal of Rehabilitation in Civil Engineering 8-3 (2020) 109-123, DOI: 10.22075/JRCE.2020.19106.1360.

João, M.- Estêvão, C. (2019). *An Integrated Computational Approach for Seismic Risk Assessment of Individual Buildings,* Applied Sciences, 2019, 9, 5088; doi:10.3390/app9235088, www.mdpi.com/journal/applsci.

Joyner, W. B. - Boore, D. M. (1981) Peak *horizontal acceleration and velocity from strong-motion records including records from the 1979 Imperial Valley, California earthquake.* Bull. Seismol. Soc. Am., 71(6): 2011–2038.

Kenneth, W. -Campbell, A.- EERI, M.- Bozorgnia, Y. (2010) A *Ground Motion Prediction Equation for the Horizontal Component of Cumulative Absolute Velocity (CAV) Based on the PEER-NGA Strong Motion Database.* Earthquake Spectra, Vol 26, No. 3, pp. 635–650, Aug. 2010; © 2010, Earthquake Engineering Research Institute.

Korkmaz, F. D.-Tugce, Y. (2015) *Earthquake Performance investigation of R/C residential buildings in Turkey.* Computers and Concrete, An Int'l Journal., 15 (6):2015.

Lenza, P., Ghersi, A., Marino, E. M., & Pellecchia, M. (2017) A *multimodal adaptive evolution of the N1 method for assessment and design of R.C. framed structures.* Earthquakes and Structures, 12(3), 271–284. https://doi.org/10.12989/EAS.2017.12.3.271.

MATLAB. (2019). Version 9.7.0.1296695 (r2019b). Natick, MA, USA. The Math Works Inc.

Melina, B- Giovanna, A.F.- Ferrara, A.- Ghersi, E.- Marino, M. – Paolo, R. P. (2015) *Seismic assessment of existing R.C. framed structures with in-plan irregularity by nonlinear static methods.* Earthquakes and Structures, An Int'l Journal., Vol. 8 No. 2, 2015.

Min,H.W.- Wangb, J.P.- Chiang, P-E.(2020) *Cumulative absolute velocity (CAV) seismic hazard assessment for Taiwan,* Journal of Earthquake Engineering, https://doi.org/10.1080/13632469.2020.1803161.

Neeva, A - Ningthoukhongjam, S. S. (2021) Development *of Fragility Curves for Different Types of RC Frame Structures.* Advances in Structural Technologies, Lecture Notes in Civil Engineering 81, https://doi.org/10.1007/978-981-15-5235-9_671.

Noura, H. - Mebarki, A. - Abed, M. (2017) *Post-quake structural damage evaluation by neural networks: theory and calibration.* European Journal of Environmental and Civil Engineering. DOI: 10.1080/19648189.2017.1304277.

Paul, O.- Vacareanu, R. (2020) *Ground Motion Model for Spectral Displacement of Intermediate-Depth Earthquakes Generated by Vrancea Seismic Source,* Geosciences 2020, 10, 282; doi:10.3390/geosciences10080282, www.mdpi.com/journal/geosciences.

Rey, J. – Berge, C. (2005) ***Étude de la variabilité de signaux synthétiques générés par trois codes de calcul et de la pertinence des indicateurs du mouvement sismique calculés sur ces signaux.*** Note technique de l'Institut Français de Radioprotection et de Sûreté Nucléaire (IRSN), DEI/SARG/2005-035.

Sabetta, F. - Pugliese, A. (1996) *Estimation of response spectra and simulation of no stationary earthquake ground motions.* Bull. Seismol. Soc. Am., 86(2):337–352.

Saiidi, M. - Sozen, M.A. (1981) *Simple Nonlinear Seismic Analysis of RC Structures.* Journal of Structural Division ASCE., 107, 937-952.

Sang, W.H.- Sung, J.H.- Hoon, K. M. - Myoungsu, S. (2014) *Improved capacity spectrum method with inelastic displacement ratio considering higher mode effects.* Earthquakes and Structures, An Int'l Journal., Vol. 7, No. 4, 2014.

Shome, N. C.- Bazzurro, P. - Carballo, JE. (1998) *Earthquakes, records, and nonlinear responses.* Earthquake Spectra, 14(3):469–500.

Tiziana, R. – Gehl, P- Stylianos, M.- Galasso, C.- Duffour, P. -Douglas, J. – Cook, O. (2016) *FRACAS: A capacity spectrum approach for seismic fragility assessment including record-to-record variability*. Engineering Structures Journal, http://dx.doi.org/10.1016/j.engstruct.2016.06.0430141-0296/Ó, 2016.

Xia, J. C- Huang, Z.J.- Yang, J. - Wu, P. (2014) Comparison *of the cumulative absolute velocity and acceleration peak value based on Wenchuan earthquake data.* Geodesy and Geodynamics. 5(3): 46–54.

sciendo

Slovak Journal of Civil Engineering

Vol. 30, 2022, No. 1, 33 – 41
DOI: 10.2478/sjce-2022-0004

THE IMPACT OF CLIMATE CHANGE ON STOCHASTIC VARIATIONS OF THE HYDROLOGY OF THE FLOW OF THE INDUS RIVER

Muhammad YONUS[1], Syed Ahmad HASSAN[2*]

Abstract

Pakistan's agricultural economy is reliant on the Indus River's irrigation system, which is fed by the water coming from the great Himalayas-Karakoram Glacier Mountains. Because of hilly terrain areas, the climatic variations have an intense effect on the river flow, especially during the winter and monsoon months. Consequently, significant variations, which are observed annually, result in flooding situations in the monsoon months and reduced flows in the winter season. Thousands of people have lost their lives and massive property destruction has taken place due to disastrous floods that occurred during 2010 and 2016. Past studies have focused on proper water resources and the management of extreme events such as floods and droughts; however, modelling and forecasting based on the various climatic factors and stochastic variations are rare. This paper attempts to forecast Indus River flows using multiple linear regression (MLR), the stochastic time series, the seasonal autoregressive integrated moving average (SARIMA), and its reduced heteroscedasticity model, i.e., SARIMA-GARCH (generalized autoregressive conditional heteroscedasticity) methods at the Kalabagh station. The results show that MLR is best over the short-term; SARIMA is better over the long-term, and SARIMA-GARCH may be superior for a very long-term forecast.

Address

[1] Dept. of Computing, Indus University Karachi, Pakistan
[2] Dept. of Mathematics, University of Karachi, Karachi, Pakistan

* ***Corresponding author:*** ahmedhassan@uok.edu.pk

Key words

- Multiple regression,
- Flood,
- Time series,
- SARIMA,
- Temperature,
- Rainfall.

1 INTRODUCTION

The Indus is the world's twenty-first largest river in its annual flow, and it is the longest river in Pakistan (Fowler and Archer, 2005) with a total drainage area of 605×105 km^2 (Hassan and Ansari, 2010). It passes through the great Himalayan-Karakoram Glacier, a mountainous region of China, India and the hilly Upper Indus basin (it contains 13% of Pakistan's 13,680 km^2 total glacier cover). It further goes in a southerly direction and finally drains into the Arabian Sea (Fowler and Archer, 2005; Shakir *et al*., 2010; Khalid *et al*., 2013). Because of the complex terrain's glaciered area, the climatic variations have an intense impact on the river flow, especially during the winter and monsoon months (Shakir *et al*., 2010). During the monsoon period, the Indus River experiences flooding situations, while in the winter season, the flow shrinks greatly. Sometimes, the floods are disastrous, leading to the death of thousands of people and the destruction of millions of hectares of croplands and built-up areas. Some major catastrophic floods occurred between 2010 and 2016 in Pakistan.

The water resources (Kiem *et al*., 2016) and hydrology of the Indus River is significantly influenced by climatic parameters such as the precipitation, temperature, humidity, and wind speed. Predicted climate change may result in the possibility of extreme events (Thevakaran *et al*., 2019) such as droughts and floods, which may disturb the usual distribution of water resources (Khan, 2001). All these features of the Indus River make it difficult to analyse its dynamics, particularly in view of possible climate change (Hassan and Ansari, 2015; 2010). An investigation of the

river dynamics along with the precise modelling and forecasting of its stream flow is very important, especially for the management of extreme events and the optimal design of water storage structures. Predicting future flow rates and the related availability of water in the Indus River needs a proper investigation of the relationship between hydrological processes and climate change. Ahmad *et al*. (1993) used time series modelling of the Indus River's annual maximum flow at the Sukkur station. Eldaw *et al*. (2003 and the references therein) utilised the principle of component analysis based on multiple linear regression (MLR) models for forecasting the flow of the Nile River. Kwon *et al*. (2009) developed a predictive model based on the hierarchical Bayesian technique to forecast the annual maximum and seasonal flows of the Yangtze River in China. Moreover, Al-Masudi (2011) obtained a forecasting model for the Dokan reservoir inflow in Iraq using ARIMA models. Some researchers (Khatibi *et al*., 2014; Adenan *et al*., 2014; Hassan and Ansari, 2010) use nonlinear prediction (NLP) methods for river flow predictions. The NLP method is a data-driven technique based on embedding flow data with suitable time delays. Hassan and Ansari (2010) compared the seasonal autoregressive integrated moving average (SARIMA) model and the nonlinear prediction (NLP) method to predict the monthly flow of the Indus River at the Tarbela station and found that the NLP forecasting was better than SARIMA. The NLP results were favourable due to the existence of the possible nonlinearity in the river flow at the Tarbela station. Moreover, the GARCH model provides a suitable framework to encompass the possible nonlinear behaviour of the second order moment (due to the effect of the exogenous variables) of a hydrological time series (Modarres and Ouarda, 2013a). This paper introduces SARIMA–GARCH modeling methods based on the possible Autoregressive conditional heteroscedasticity (ARCH) effect indicated in the residuals of the SARIMA method.

Furthermore, to improve the understanding of the local climate on the Indus River flow at the Kalabagh station, this study also analyses a stepwise technique based on the MLR method. This paper conclusively analyses and compares the SARIMA, SARIMA–GARCH and MLR methods to forecast the Indus River flow at the Kalabagh station. The results are very promising when using all three methods; additionally, the indication of nonlinearity of the second order moment in the residual of SARIMA is eliminated using the SARIMA–GARCH model. However, the SARIMA–GARCH forecasts are not a more successful improvement than the SARIMA method. Nevertheless, when comparing the forecast with different time spans, the SARIMA-GARCH outcomes have the unique feature of increasing with higher rates. The study is divided into different sections: Section 2 explains the data description and methodology concerning the modelling procedure and forecasting performance of the MLR, SARIMA and SARIMA–GARCH models. Section 3 shows the results and discussion, whereas, section 4 provides the conclusion of the study.

2 METHODOLOGY

The mean monthly river flow data of the Indus River at the Kalabagh station (from January 1976 to December 2013; i.e., 38 years; 456 data points), and the temperature and monthly total rainfall data of six (6) different meteorological stations (Sialkot, Murree, Chitral, Lahore, Balakot and Kotli) of the same time frame are considered for this study (Fig. 1). The first 360 data points (Jan., 1976 to Dec., 2005) are used for estimating the parameters, and the remaining 96 (Jan., 2006 to Dec., 2013) are used for a comparison of the forecasts. The seasonal plots show the summer peaks (Jun.-Aug.) of the river's flow (Figure 2a) and the temperature (Figure 2b). The seasonal plot of the rainfall (Figure 2c) represents the two major sources, i.e., the summer monsoon and winter (Dec.-to-Feb.) (Jamil and Khan, 2012).

Tab. 1 *Correlation between mean Monthly River flow at Kalabagh station with Rainfall and Temperature of the selected cities shows a stronger correlation with the temperature than the rainfall (1976-2013)*

Correlation coefficient	Kotli	Lahore	Murree	Sialkot	Chitral	Balakot
Rainfall/Flow	0.600	0.669	0.563	0.679	-0.402	0.522
P-Values	0.000	0.000	0.000	0.000	0.000	0.000
Temp /Flow	0.737	0.718	0.742	0.728	0.852	0.789
P-Values	0.000	0.000	0.000	0.000	0.000	0.000

2.1 MLR Modelling method

The Pearson correlation is initially analysed to find the linear relationship between the climate and hydrological data series (Naheed *et al*., 2013). Table 1 shows a significant positive correlation between the rainfall and river flow of five cities (Kotli, Lahore, Murree, Sialkot and Balakot) and the negative correlation (-0.402) between the rainfall and river flow of the Chitral. The significant positive correlation of the five cities shows the strong seasonal impact of the rainfall on the river flow (Table 1), whereas, the negative values appeared because Chitral only has a winter rainfall season (Figure 2c), and the monsoon depression does not reach it because it is far away from the conventional (historical) monsoon depression tracks (Hassan and Ansari, 2015). Despite the low inverse relation of the Chitral rainfall, its temperature shows a maximum correlation (0.852) with the river flow, because both have the same annual seasonal variations (Figures 2a and 2b). Furthermore, the temperature data of all the cities were found to have a significant positive correlation with the river flow; (Table 1) shows a strong impact. These interdependent relations can be modelled using the MLR method for the Indus River flow at the Kalabagh station. This suggested model will be helpful for forecasting future extreme events such as floods and droughts.

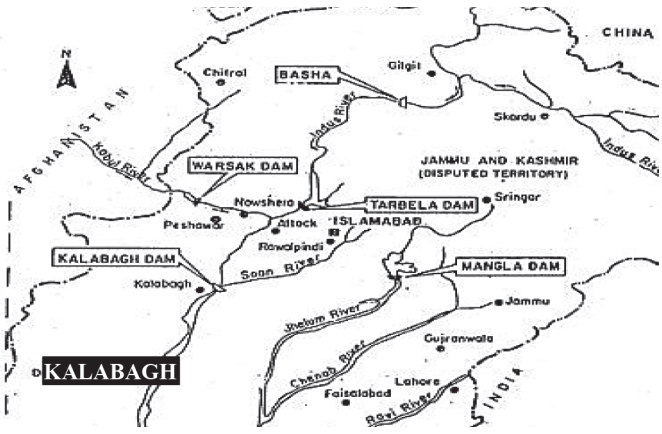

Fig. 1 *Study Area*

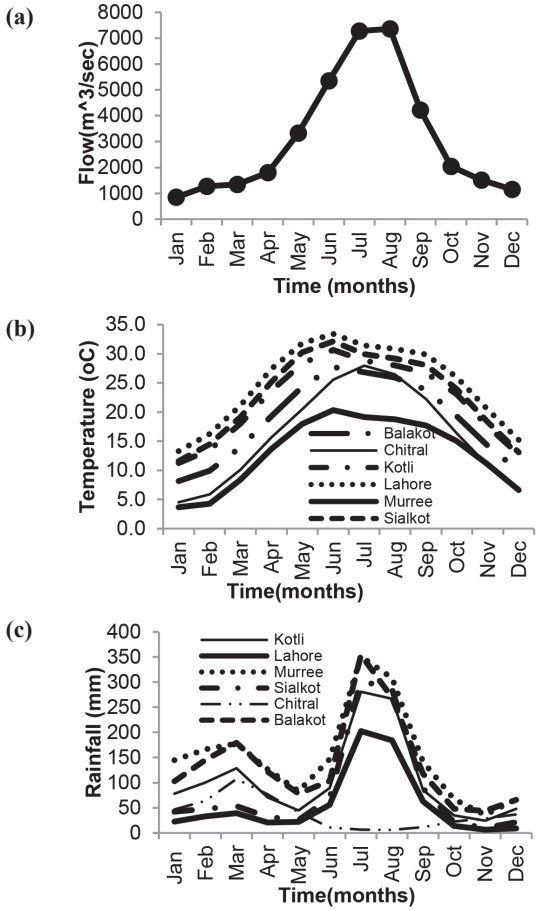

Fig. 2 *Seasonal pattern plot (Jan.1976-Dec.2013) (a) River Flow at Kalabagh station, different cities (b) Temperature and (c) rainfall*

The MLR can be expressed as

$$Y_t = b_0 + b_1 X_{1,t} + b_2 X_{2,t} + \ldots + b_k X_{k,t} + \varepsilon_t, \quad (1)$$

where $X_{i,t}$s are the predictors; the b_i's are their coefficients; and Y_t is the prediction (Indus River flows). The regression coefficients are determined by using the least squares estimation method. In the presence of large independent variables, the stepwise regression method (Markridakis *et al*. 2008) is employed to compute the possibly significant models (Eq. 1) of the leading variables using the step forward technique. In this procedure, the predictor was removed from the equation when its coefficient had a low significant (p-values < 5%) value (Eldaw *et al*., 2003; Hamza & Hassan, 2015). Accordingly, only four MLR models (Table 2) have been selected and represented:

Model **MLR-1**:

$$Q^1 = \alpha_0^1 + \alpha_1^1 R_{Sialkot} + \alpha_2^1 R_{Murree} + \alpha_3^1 R_{Balakot} + \alpha_4^1 T_{Chitral} + \\ + \alpha_5^1 T_{Lahore} + \alpha_6^1 T_{Balakot} + \alpha_7^1 T_{Kotli} \quad (2)$$

Model **MLR-2**:

$$Q^2 = \alpha_0^2 + \alpha_1^2 R_{Sialkot} + \alpha_2^2 R_{Murree} + \alpha_3^2 T_{Chitral} + \\ + \alpha_4^2 T_{Lahore} + \alpha_5^2 T_{Balakot} \quad (3)$$

Model **MLR-3**:

$$Q^3 = \alpha_0^3 + \alpha_1^3 R_{Sialkot} + \alpha_2^3 R_{Murree} + \alpha_3^3 T_{Chitral} + \alpha_4^3 T_{Lahore} \quad (4)$$

Model **MLR-4**:

$$Q^4 = \alpha_0^4 + \alpha_1^4 R_{Sialkot} + \alpha_2^4 T_{Chitral} + \alpha_3^4 T_{Lahore} \quad (5)$$

where Q^i shows the i^{th} monthly amount of flow at the Kalabagh station; whereas, $R_{Sialkot}$, R_{Murree}, and $R_{Balakot}$ represent rainfall; and $T_{Chitral}$, T_{Lahore}, $T_{Balakot}$ and T_{Kotli} denote the temperature of the cities mentioned in each subscript. For the estimation of the parameters of Eqs. 2 to 5, the Eviews-6 software was used. To select the best model, the R-squared, Adj. R-squared, Durbin-Watson (DW), Akaike information, and Schwartz criterion measures (Table 2) were employed (Hassan and Ansari, 2010). Moreover, Table 2 reveals that the DW statistics are insignificant (i.e., DW << 2) because some significant initial lag values appear in the autocorrelation graph of the residuals (Figure 3). This indicates that some time-varying information stays in the error terms that can prevent obtaining better MLR forecasts. In other words, the river flow actually relies on many independent variables having different intrinsic time series variation patterns that may not collectively explain the predicted data form. Furthermore, based on the above stated criteria (Table 2), MLR-1 is the best relative to the other models selected.

Tab. 2 *Selection criterion based on predictive accuracy of the proposed MLR-1 to MLR-4 models (Eq. 3 to 6)*

MLR Proposed Models	R-squared	Adjusted R-squared	Durbin-Watson statistics	Akaike information criterion
MLR-1	**0.84509**	**0.842009**	**1.324634**	**16.63607**
MLR-2	0.841976	0.839744	1.341582	16.64486
MLR-3	0.838173	0.83635	1.324408	16.66309
MLR-4	0.826199	0.824735	1.333089	16.72891

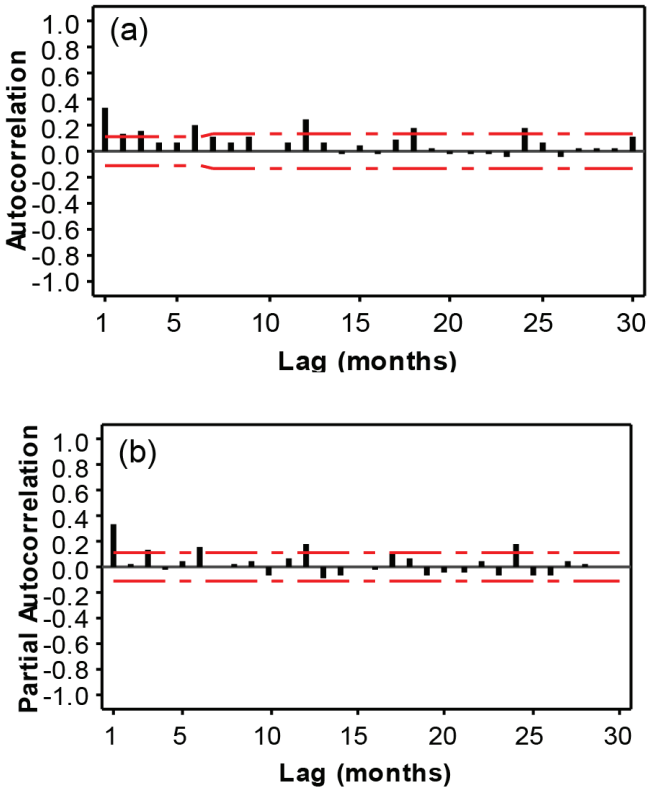

Fig. 3 *Residual correlograms of MLR-1 model (a) ACF and (b) PACF*

2.2 Stochastic time series method

The general multiplicative seasonal ARIMA (SARIMA) model of the Box & Jenkins (1994) methodology (Box & Jenkins 1994; Hamza & Hassan, 2015) is used in this paper. The SARIMA model $(p, d, q)\times(P,D,Q)_s$ is described as:

$$\phi_p(B)\nabla^d\Phi_P(B^s)\nabla_s^D Y_t = \theta_q(B)\,\Theta_Q(B^s)\,\varepsilon_t \quad (6)$$

where Y_t is the observed outflow (m^3/sec.); ε_t is the white noise process, and $\phi_p(B)$, $\theta_q(B)$ are the polynomials in B of order p and q of the autoregressive and moving average parameters, respectively. Similarly, $\Phi_P(B^s)$ and $\Theta_Q(B^s)$ are the polynomials in B^s of the seasonal autoregressive and moving average parameters, respectively. The D and d are the seasonal and non-seasonal order of differencing, respectively, whereas, S is the seasonal number (e.g. 12 for the monthly data). The polynomials in Eq. 6 are further defined as:

$$\phi_p(B) = (1-\phi_1 B- \phi_2 B^2-\ldots- \phi_p B^p) \quad (7)$$

$$\Phi_P(B^s) = (1-\Phi_1 B^s-\Phi_2 B^{2s}-\ldots-\Phi_P B^{ps}) \quad (8)$$

$$\theta_q(B) = (1-\theta_1 B-\theta_2 B^2-\ldots-\theta_q B^q) \quad (9)$$

$$\Theta_Q(B^s) = (1-\Theta_1 B^s-\Theta_2 B^{2s}-\ldots-\Theta_Q B^{Qs}) \quad (10)$$

where, B is the backward shift operator such that $BY_t = Y_{t-1}$, and $B^sY_t = Y_{t-s}$. The difference operators ∇ are such that $\nabla=1-B$, $\nabla^d= (1-B)^d$ and $\nabla_s^D= (1-B^s)^D$. The selection of a suitable model in the time series method follows three steps, i.e., identification, parameter estimation, and diagnostic checking (Box and Jinken, 1994; Ahmad *et al*., 1993; Hassan and Ansari, 2010); finally, it helps to forecast the future values.

2.2.1 SARIMA modelling procedure

The observed time series plot shows the main features such as the seasonality, trends, outliers and discontinuities (Al-Masudi, 2011). The seasonal low and high flows of the winter and summer, respectively, can be clearly observed within each annual cycle of the time series plot (Figure 4; all 456 data points). The river starts rising from April to June and declines to a recession flow level from October to March. To identify the proper structure and order of the proposed model, the ACF and PACF plots must be analysed (Hassan & Ansari, 2010; Al-Masudi, 2011). The ACF and PACF plots in Figures 5a and 5b show some significant spikes in the initial lags with a prominent annual seasonal pattern. These spikes of the ACF and PACF plots (Figures 5a & 5b) help to select the order of the MA and AR components of the proposed SARIMA models, respectively. These analyses suggested five SARIMA models, i.e., $(1,0,0)\times(1,0,1)_{12}$, $(0,0,1)\times(1,0,1)_{12}$, $(0,0,2)\times(1,0,1)_{12}$, $(0,0,2)\times(1,0,0)_{12}$ and $(2,0,0)\times(0,0,1)_{12}$ (Table 3). The most suitable among these include the best values of the R-squared, Schwarz criterion (Schwarz, 1978), the DW statistic (Markridakis *et al*., 2008), and the Akaike information criterion (Akaike, 1974) along with significant (p-value < 0.05) parameters coefficient values (estimated from the Eviews-6 software: Table 3). This procedure proposes the SARIMA $(1,0,0)\times(1,0,1)_{12}$ model (Table 3) as the best among the five; it is defined as:

$$(1-\boldsymbol{\phi_1}B)\,(1-\boldsymbol{\Phi_1}B^{12})\,Y_t = (1+\boldsymbol{\Theta_1}B^{12})\,\varepsilon_t \quad (12)$$

Moreover, the residuals left over after the fitting of a good model should simply be white noise that represents no significant serial correlative (ACF and PACF) values (Figure 5) (Markridakis *et al*., 2008). Hence the suggested model can be considered as appropriate for forecasting.

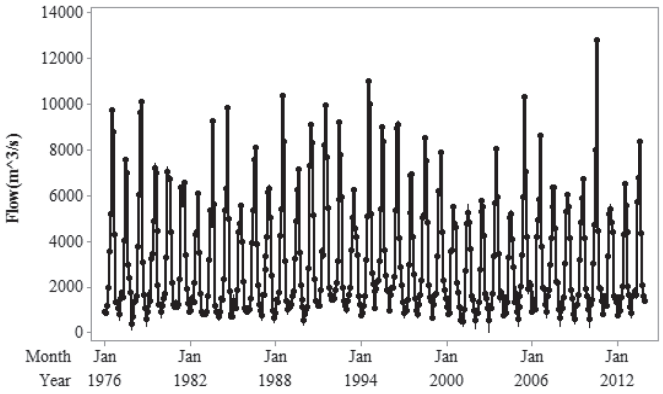

Fig. 4 *Time series plot of Indus River flow at Kalabagh station (Jan.1976-Dec.2013).*

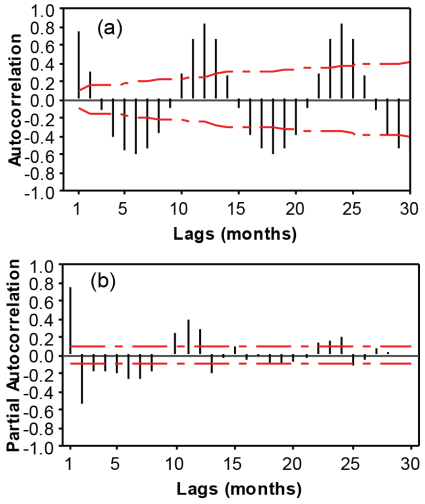

Fig. 5 *Indus River flow at Kalabagh station correlograms (Jan.1976-Dec.2005), (a) ACF and (b) PACF*

Tab. 3 *Selection criterion based on prediction accuracy of the five SARIMA suggested models*

SARIMA model $(p,d,q)\times(P,D,Q)_s$	Model Equation	R-squared	Durbin-Watson statistics	Akaike information criterion	Schwarz criterion
$(1,0,0)\times(1,0,1)_{12}$	**$(1-\phi_1B)\,(1-\Phi_1B^{12})\,Y_t = (1-\Theta_1B^{12})\,\varepsilon_t$**	**0.880408**	**1.979665**	**16.33372**	**16.367**
$(0,0,2)\times(1,0,1)_{12}$	$(1-\Phi_1B^{12})\,Y_t=(1-\theta_1B-\theta_2B^2)\,(1-\Theta_1B^{12})\,\varepsilon_t$	0.880271	1.984737	16.34024	16.38452
$(0,0,1)\times(1,0,1)_{12}$	$(1-\Phi_1B^{12})\,Y_t=(1-\theta_1B)\,(1-\Theta_1B^{12})\,\varepsilon_t$	0.879285	1.925292	16.3427	16.37591
$(0,0,2)\times(1,0,0)_{12}$	$(1-\Phi_1B^{12})\,Y_t=(1-\theta_1B-\theta_2B^2)\,\varepsilon_t$	0.818936	1.972186	16.74812	16.78133
$(2,0,0)\times(0,0,1)_{12}$	**$(1-\phi_1B-\phi_2B^2)\,Y_t= (1-\Theta_1B^{12})\,\varepsilon_t$**	**0.695018**	**1.988721**	**17.2868**	**17.31932**

2.2.2 Hybrid SARIMA-GARCH methods

The existence of conditional or time-varying variances (volatility) in a univariate stochastic process is called heteroscedasticity, and if they are constant, then it is known as homoscedasticity (Wang, 2006; Modarres and Ouarda, 2013b). The autoregressive conditional heteroscedasticity (ARCH) model was introduced by Engle (1982); later, Bollerslev (1986) and Nelson (1991) extended it to their Generalized (GARCH) models. This method gives a suitable framework for focusing on the nonlinear behaviour of the second order moment of a hydrological time series (Modarres and Ouarda, 2013a; Senaviratna *et al*., 2017; Agnolucci, 2009; Sigauke and Chikobvu, 2011; Yaziz *et al*., 2013; Pahlavani and Roshan, 2015, among others). Closely associated studies from the recent past include Wang *et al*. (2005), Wang (2006), Otache *et al*. (2012), Wang *et al*. (2012), and Modarres & Ouarda (2013a and 2013b); these writers investigated and applied different types of GARCH models in stream flow time series modelling.

The SARIMA–GARCH (*V*, *M*) model (Modarres and Ouarda, 2013b) is one in which the variance of the error term of the SARIMA model follows a GARCH process. The hybridisation of the SARIMA and GARCH models is a two-step method (Pahlavani and Roshan, 2015). In the first step, in applying the best of the SARIMA models the residuals (errors) of the SARIMA may show adequate and, sometimes, time-dependent or conditional variances, which can be accommodated by utilizing a GARCH model (Yaziz *et al*., 2013; Modarres and Ouarda, 2013b; Sigauke and Chikobvu, 2011). In the second step, the best GARCH model is employed to incorporate the possible nonlinear patterns of the residuals (Yaziz *et al*., 2013; Sigauke and Chikobvu, 2011).

The SARIMA error $\hat{I}_t$ said to follow a GARCH (*V*, *M*) process of orders *V* (ARCH) and *M* (GARCH) (Sigauke and Chikobvu, 2011; Yaziz *et al*., 2013; Modarres and Ouarda, 2013b; Pahlavani and Roshan, 2015).

The error term ε_t of the SARIMA model (Eq. 6) can be written as:

$$\epsilon_t = z_t\sigma_t, \text{ where } z_t \sim \text{iid } N(1,0) \quad \text{and}$$

$$\sigma_t^2 = \alpha_0 + \sum_{i=1}^{V} \alpha_i \epsilon_{t-i}^2 + \sum_{j=1}^{M} \beta_j \sigma_{t-j}^2$$

where σ_t^2 is the conditional variance of the error term ϵ_t ; α_i and β_i are the coefficients of the ARCH and GARCH parameters respectively. The ε_{t-i}^2 is the information about the volatility from the i^{th} lag period and σ_{t-j}^2 is the j^{th} lag period forecast error variance; z_t is the standardized error term. The GARCH (*V*, *M*) part of the hybrid model describes the conditional variance, whereas, the conditional mean is explained by a SARIMA model (Modarres and Ouarda, 2013a; and 2013b).

In the SARIMA-GARCH modelling procedure, the ARCH-LM Lagrange Multiplier test is applied to look for the existence of heteroscedasticity in the estimated errors of the SARIMA prediction. The results in Table 4 (last column: 0.0152) depict the presence of the ARCH effect (*p*-value < 0.05) in the series, which may reject the null hypothesis; H_o: No ARCH effect is in the residual, at the 5% level of significance. After trying many combinations, only the GARCH (1,1) model gives optimum and significant results. Accordingly, the SARIMA–GARCH model should be applied; then the residuals of this hybrid model should be checked using the ARCH-LM test. The probability of the observed R-squared (0.4353: Table 4) is greater than 0.05, which reveals that neither any heteroscedasticity nor further ARCH effect is found in this model at a 5% significance level. Therefore, the SARIMA–GARCH model is found to be reasonable to eliminate the persistent unpredictability of the SARIMA. However, there is no guarantee of a better performance of the SARIMA–GARCH model forecast, at least for this case study. The SARIMA-GARCH model would be a very useful addition to the local hydrological community and should be the topic of future research efforts to investigate/accommodate conditional variances in hydrological processes. The selection of the most appropriate model for forecasting between SARIMA $(1,0,0)\times(1,0,1)_{12}$ and SARIMA $(1,0,0)\times(1,0,1)_{12}$-GARCH (1,1) based on the R-squared, Durbin-Watson, Akaike information, and Schwartz criterion (Table 5), suggests the SARIMA $(1,0,0)\times(1,0,1)_{12}$ model's performance is the best.

The forecasting procedure values are computed for the monthly data of 8 years (2006-2013) using the *n* step ahead method. To assess these values, the correlation coefficient (CC), mean absolute error (MAE), root mean squared error (RMSE), and mean absolute percentage error (MAPE) between the observed and forecasted values (Table 6) are analysed.

Tab. 4 *Heteroscedasticity ARCH Test for:* **SARIMA (1,0,0) × (1,0,1)$_{12}$** *Model.*

F-statistic	5.954959	Prob. F(1,344)	0.0152
Obs*R-squared	5.887660	Prob. Chi-Square(1)	0.0152

SARIMA (1,0,0) × (1,0,1)$_{12}$-GARCH (1,1) Model.

F-statistic	0.606158	Prob. F(1,344)	0.4368
Obs*R-squared	0.608610	Prob. Chi-Square(1)	0.4353

Tab. 5 *Comparison of two selected models based on their predictive performance*

Model	R-squared	Durbin-Watson statistics	Akaike information criterion	Schwarz criterion
SARIMA (1,0,0) × (1,0,1)$_{12}$	**0.880408**	**1.979665**	**16.33372**	**16.367**
SARIMA (1,0,0) × (1,0,1)$_{12}$-GARCH(1,1)	**0.863396**	**1.976858**	**17.37731**	**17.44386**

Tab. 6 *Comparison of forecasting accuracies of SARIMA, SARIMA-GARCH and MLR models (Jan 2006-Dec 2013)*

Model	MAE	RMSE	MAPE	CC
SARIMA (1,0,0) × (1,0,1)$_{12}$	**497.53**	**894.90**	**16.14**	**0.92**
SARIMA(1,0,0) × (1,0,1) $_{12}$-GARCH(1,1)	625.11	1118.32	18.59	0.874
MLR-1 Model	**657.50**	**1004.11**	**30.09**	**0.905**

3 RESULTS AND DISCUSSION

A comparison between the selected SARIMA and MLR models on the basis of the higher R-squared, close to 2 DW values (for the SARIMA only), and the lowest values of the Akaike and Schwarz criteria shows that the MLR-1 and SARIMA $(1,0,0)\times(1,0,1)_{12}$ models are the best in each category (Tables 2 & 3). Moreover, only a few spikes appear in the ACF and PCAF plots of the residuals for the MLR and SARIMA (Figures 3 and 8), which may also confirm the best selection and adequacy of the models.

The forecasted and observed flow values of the MLR and SARIMA models have a very close agreement as is shown in the time series and scattered plots (Figures. 6, 7, 9a and 10 a & 10b). The higher CC value and smaller values of the MAE, RMSE and MAPE (Table 6) show a better degree of accuracy of the forecast. Furthermore, its suitability can be confirmed through a quantile–quantile (QQ) plot (Figures, 11a and 11b); if the points fall approximately along a 45° sloping line, then the forecasted values and the observed flows are of the same distribution (Modarres and Ouarda, 2013a). The time series, scatter and QQ plots (Figures. 6,

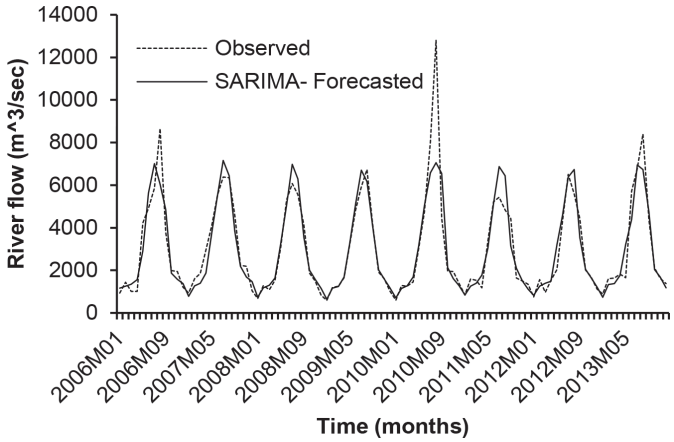

Fig. 6 Comparison of observed and SARIMA (1,0,0) × (1,0,1)$_{12}$ forecasted flow (Jan. 2006- Dec. 2013).

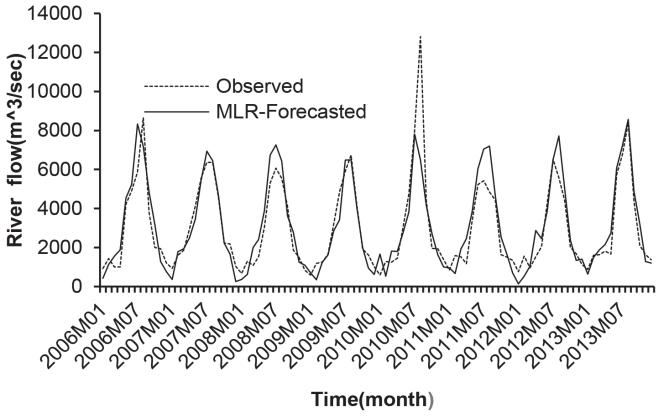

Fig. 7 *Comparison of observed and MLR-1 forecasted flows (Jan.2006-Dec.2013)*

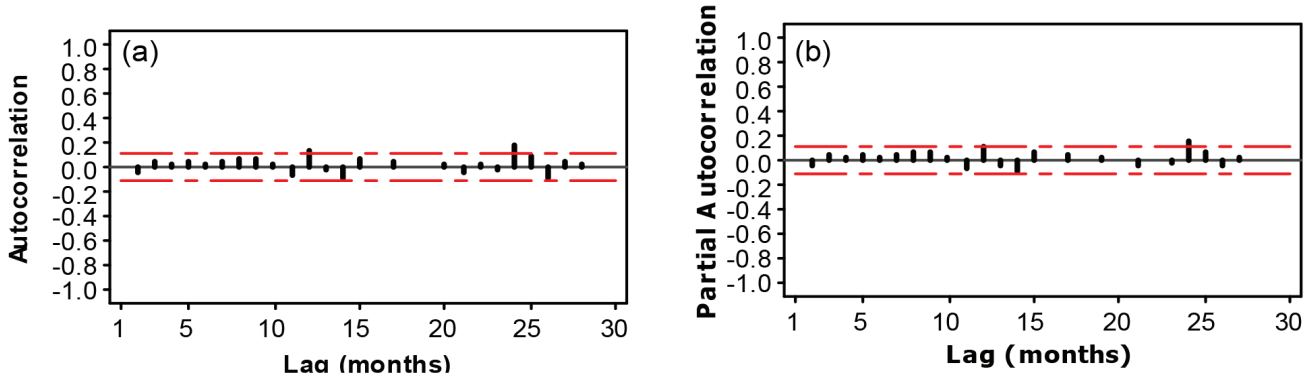

Fig. 8 *Correlograms of SARIMA (1,0,0) × (1,0,1)$_{12}$ residual (a) ACF and (b) PACF*

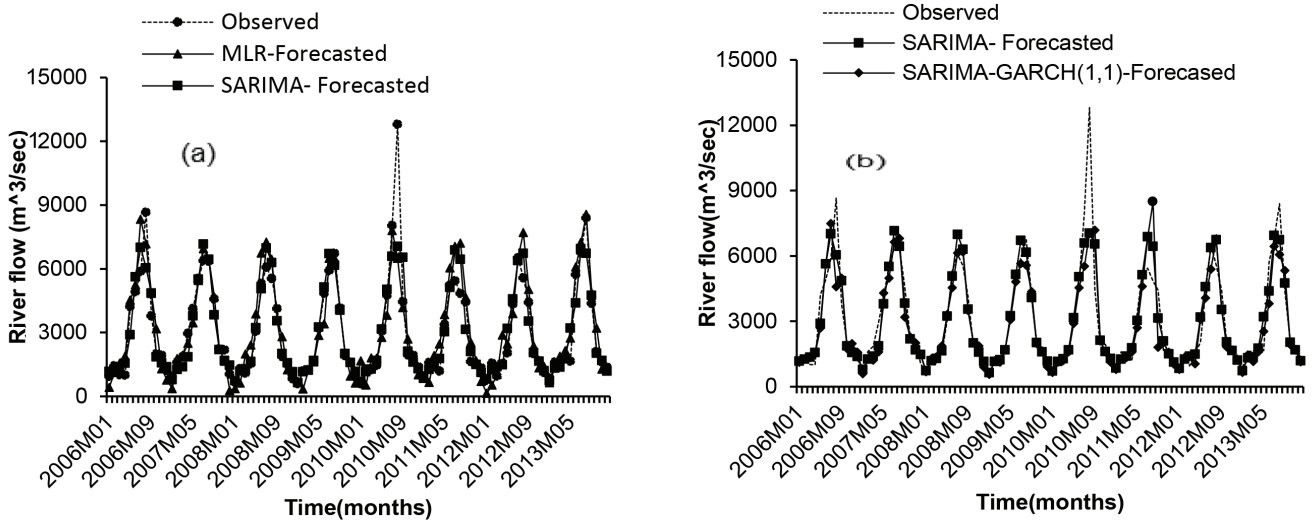

Fig. 9 *Comparison of observed (Jan.2006-Dec.2013) with (a) SARIMA and MLR forecasted flow and (b) SARIMA and SARIMA-GARCH*

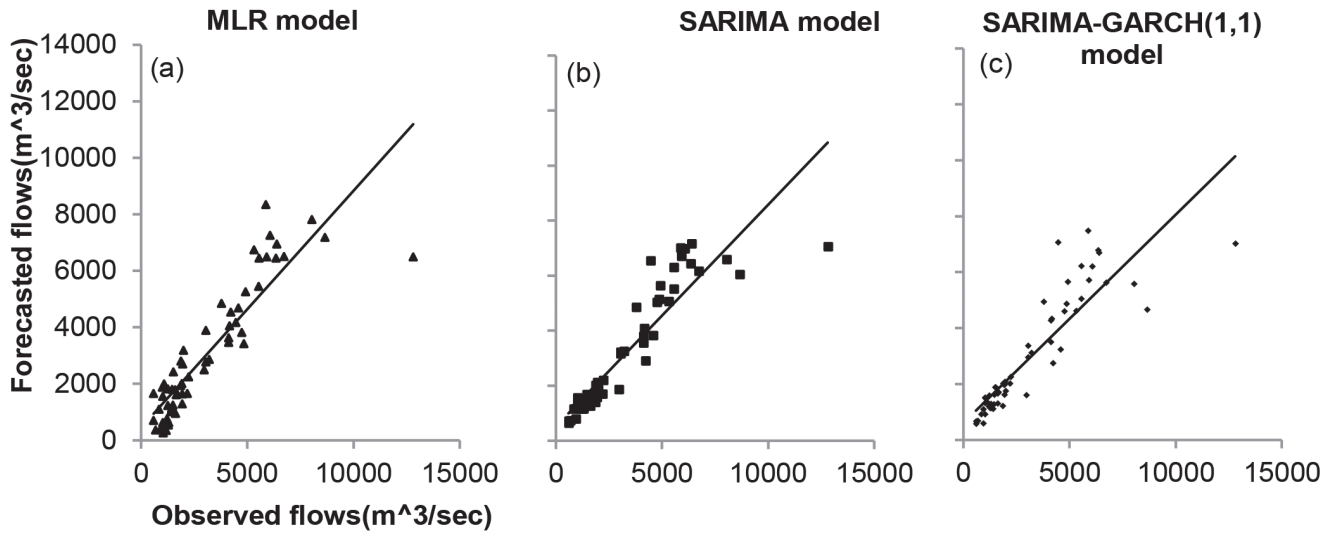

Fig. 10 *Scatter plot between observed and (a) MLR-1 (b) SARIMA and (c) SARIMA-GARCH forecasted flows*

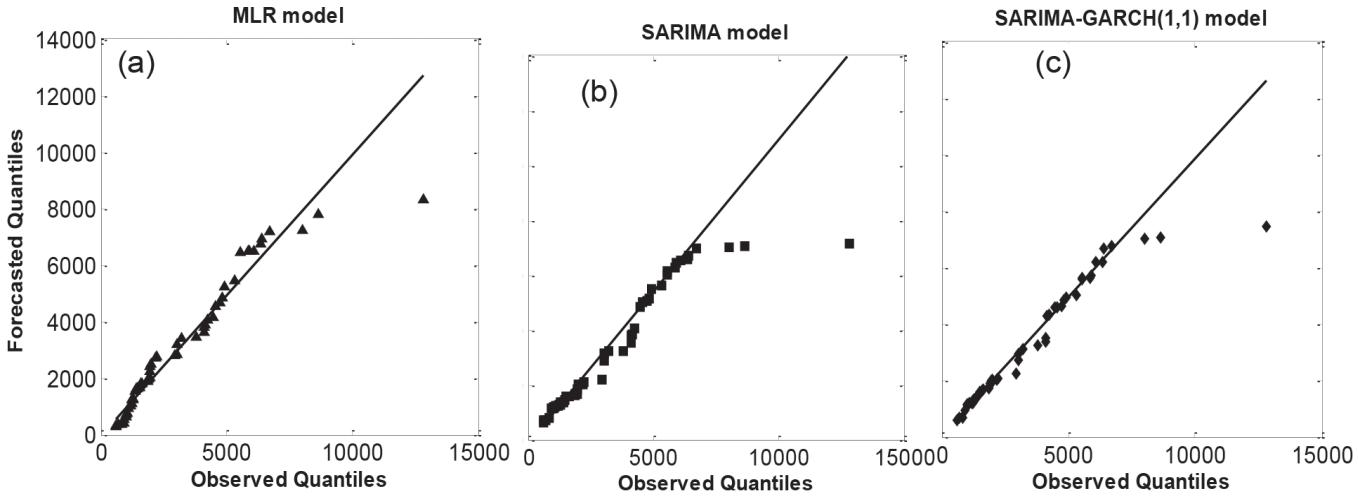

Fig. 11 *QQ (quantile–quantile) plot between observed and (a) MLR-1 (b) SARIMA and (c) SARIMA-GARCH forecasted flows Quantiles.*

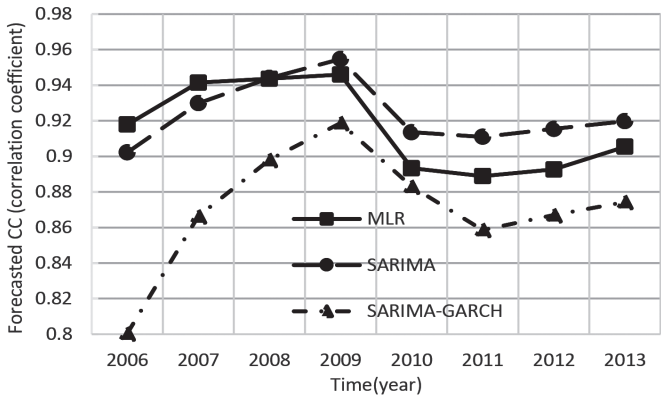

Fig. 12 *Comparative analysis of the correlation coefficient (CC) of the different models forecasts*

7, 9(a), 10a, 10b, 11a and11b) of the observed and forecasted flows, and the good values of the forecast indicators (Table 6) confirm the best performance of the SARIMA model.

The residuals of the SARIMA model may show adequate and, sometimes, conditional variances, which can be accommodated by utilizing a GARCH model. Some weak conditional heteroscedasticity in the residuals of the SARIMA prediction can be found (Section 2.2.2; Table 4), and this can be removed by the best fitted SARIMA $(1,0,0)\times(1,0,1)_{12}$-GARCH(1,1) model (Table 4). Therefore, this model sufficiently compensates for the conditional variances of the river flow time series (Table 4). However, the results from Table 6 and Figs. 9b, 10c and 11c show no improvement in the forecast indicators of the SARIMA-GARCH model as compared to that of the SARIMA $(1,0,0)\times(1,0,1)_{12}$ model (Table 6). It can be therefore said that the SARIMA $(1,0,0)\times(1,0,1)_{12}$ is good for modelling and forecasting the river flow time series of the Indus.

It seems that the GARCH model is essential to remove the heteroscedasticity (or volatility) remaining in the residuals of the SARIMA $(1,0,0)\times(1,0,1)_{12}$ model. Additionally, Figure 12 analyses the forecast performance among the three models using the CC relation for different time spans (1, 2, 3, 4, 5, 6, 7 and 8 years). It shows that the MLR model is best for short-term forecasting because it has higher CC values in the first two years, whereas, the SARIMA results indicate that it is best for a long-term period (maximum of at least three years). Moreover, the relatively low CC values of the SARIMA-GARCH forecast exhibit a unique feature of the higher increasing rates of the CC values. This may

suggest that for long or very long-term forecasting, it is best to remove the heteroscedasticity in the time series model, which may compromise the efficiency, if that is acceptable.

4 CONCLUSIONS AND RECOMMENDATIONS

The exploration and forecasting of river flow dynamics are significant in the management of water resources. Therefore, this paper has analysed and forecasted Indus River flows by MLR, SARIMA and SARIMA-GARCH models at the Kalabagh station. The results illustrate the meaningful impact of the preferred climatic parameters on the river flows. Moreover, the residuals of the SARIMA model disclose the additional structure of heteroscedasticity; accordingly, the predictive SARIMA-GARCH model completely describes a higher degree of variability in river flow volatility. However, the SARIMA model has stronger explanatory power than the other two methods and is proposed as a good forecaster of the mean monthly flow of the Indus River. Nevertheless, the SARIMA-GARCH model could be a very useful addition to the local hydrological community and should be the topic of future research efforts to investigate/accommodate conditional variances in hydrological processes. It is expected to be the most suitable for a long-term consistent performer with a little compromise in the efficiency of the forecast.

Acknowledgements

We would like to thank the Department of Mathematics, University of Karachi. This research was funded by the DFS grant of University of Karachi. We acknowledge the Irrigation Department of the Government of Sindh and Pakistan and the Meteorological Department (PMD) Karachi for cooperation in the data collection. The contents of this paper form a supplementary part of the first author's doctoral thesis.

REFERENCES

Adenan, N. H. - Noorani, M. S. M. (2014) Nonlinear prediction of river flow in different watershed acreage, *KSCE Journal of Civil Engineering, vol.* 18, no**.** 7, pp. 2268-2274.

Agnolucci, P. (2009) Volatility in crude oil futures: a comparison of the predictive ability of GARCH and implied volatility models, *Energy Economics,* vol. 31, no. 2, pp. 316-321.

Ahmad, M. S. - Ahmad, M. I. - Naeem, H. M. - Sarwar, M. (1993) Time Series Modelling of Annual Maximum Flow of River Indus At Sukkur, *Pak. J. Agri. Sci, vol.* 30, no.1.

Akaike, H. (1974) A new look at the statistical model identification *Automatic Control, IEEE Transactions on, vol.* 19, no. 6, pp. 716-723.

Al-Masudi, R. K. (2011) Fitting ARIMA Models for Forecasting to Inflow of Dokan Reservoir, *Journal of Babylon University, vol.* 19, no. 4.

Bollerslev, T. (1986) Generalized autoregressive conditional heteroskedasticity, *Journal of econometrics, vol.* 31, no.3, pp. 307-327.

Box, G.E.P. - Jenkins, G.M. (1994) Time Series Analysis; Forecasting and Control, *Holden Day*, San Francisco, CA, USA.

Eldaw, A. K. - Salas, J. D. - Garcia, L. A. (2003) Long-range forecasting of the Nile River flows using climatic forcing, *Journal of Applied Meteorology, vol.*42, no.7, pp. 890-904.

Engle, R. F. (1982) Autoregressive conditional heteroscedasticity with estimates of the variance of United Kingdom inflation, *Econometrica: Journal of the Econometric Society, pp.* 987-1007.

Fowler, H. J. - Archer, D. R. (2005) Hydro-climatological variability in the Upper Indus Basin and implications for water resources, *Regional Hydrological Impacts of Climatic Change—Impact Assessment and Decision Making, vol.* 295, pp.131-138.

Hamza, K. - Hassan, S. A. (2015) Stochastic River Flow Modelling and Forecasting of Upper Indus Basin, *Journal of Basic & Applied Sciences, vol.* 11, pp. 630-636.

Hassan, S. A. - Ansari, M. R. K. (2010) Nonlinear analysis of seasonality and stochasticity of the Indus River, *Hydrological Sciences Journal–Journal des Sciences Hydrologiques, vol.* 55, no. 2, pp. 250-265.

Hassan, S. A. - Ansari, M. R. K. (2015) Hydro-climatic aspects of Indus River flow propagation, *Arabian Journal of Geosciences, vol.* 8, no.12, pp.10977-10982.

Jamil, S. - Khan, M. N. (2012) Seasonal variations of vivax and falciparum malaria: an observation at a tertiary care hospital, *J. Ayub Med Coll Abbottabad, vol.* 24, no.1.

Khalid, S. - Qasim, M. - Farhan, D. (2013) Hydro-meteorological characteristics of Indus River Basin at extreme north of Pakistan, *J. Earth Sci. Clim. Change, vol.*5, no.2.

Khan, A. R. (2001) Analysis of hydro-meteorological time series: Searching evidence for climatic change in the Upper Indus Basin, *International Water Management Institute (IWMI), Lahore, Pakistan*.

Khatibi, R. - Ghorbani, M. A. - Naghipour, L. - Jothiprakash, V. - Fathima, T. A. - Fazelifard, M. H. (2014) Inter-comparison of time series models of lake levels predicted by several modeling strategies, *Journal of Hydrology, vol.* 511, pp. 530-545.

Kiem, A. S. - Austin, E. K. - Verdon-Kidd, D. C. (2016) Water resource management in a variable and changing climate: hypothetical case study to explore decision making under uncertainty, *Journal of Water and Climate Change. Vol.* 7, no. 2, pp. 263-279.

Kwon, H. H., Brown, C., Kaiqin, X. and Lall, U. (2009) Seasonal and annual maximum streamflow forecasting using climate information: application to the Three Gorges Dam in the Yangtze River basin, China, *Hydrological sciences journal, vol.* 54, no. 3, pp. 582-595.

Markridakis, S. - Wheelwright, S.C. - Hyndman, R. J. (2008) Forecasting methods and application, John Wiley & Sons.

Modarres, R. - Ouarda, T. B. M. J. (2013a) Generalized autoregressive conditional heteroscedasticity modelling of hydrologic time series, *Hydrological Processes, vol.* 27, no. `22, pp. 3174-3191.

Modarres, R. - Ouarda, T. B. M. J. (2013b) Modelling heteroscedasticty of streamflow times series, *Hydrological sciences journal, vol.* 58, no.1, pp. 54-64.

Naheed, G. - Kazmi, D. H. - Rasul, G. (2013) Seasonal Variation of Rainy Days in Pakistan, *Pakistan Journal of Meteorology, vol.* 9, no.18.

Nelson, D. B. (1991) Conditional heteroskedasticity in asset returns: A new approach, *Econometrica: Journal of the Econometric Society*, pp. 347-370.

Pahlavani, M. - Roshan, R. (2015) The Comparison among ARIMA and hybrid ARIMA-GARCH Models in Forecasting the Exchange Rate of Iran, *International Journal of Business and Development Studies, vol.* 7, no.1, pp. 31-50.

Schwarz, G. (1978) Estimating the dimension of a model, *The annals of statistics, vol.* 6, no. 2, pp. 461-464.

Senaviratna, N. A. M. R. - Cooray, T. M. J. A. (2017) Forecasting gold prices in Sri Lanka using generalized autoregressive conditional heteroscedasticity approach, *International Research Journal of Natural and Applied Sciences, vol.* 4, no.7, pp. 99-110.

Shakir, A. S. - Rehman, H. - Ehsan, S. (2010) Climate Change Impact on River Flows in Chitral Watershed, *Pakistan Journal of Engineering & Applied Sciences, vol.* 7, pp. 12-23.

Sigauke, C. - Chikobvu, D. (2011) Prediction of daily peak electricity demand in South Africa using volatility forecasting models, *Energy Economics*, vol. 33, no. 5, pp. 882-888.

Thevakaran, A. - Suppiah, R. - Sonnadara, U. (2019) Trends in extreme rainfall events in Sri Lanka, 1961-2010, *Journal of the National Science Foundation of Sri Lanka, vol.* 47, no. 3.

Wang, H. - Gao, X. - Qian L. - Yu, S. (2012) Uncertainty analysis of hydrological processes based on ARMA-GARCH model, *Science China Technological Sciences*, pp. 1-11.

Wang, W. (2006) *Stochasticity, nonlinearity and forecasting of streamflow processes* (Doctoral dissertation, TU Delft, Delft University of Technology).

Wang, W. - Van Gelder, P. H. A. J. M. - Vrijling J. K. - Ma, J. (2005), Testing and modelling autoregressive conditional heteroskedasticity of streamflow processes, *Nonlinear processes in Geophysics, vol.* 12, no.1, pp. 55-66.

Yaziz, S. R. - Azizan, N. A. - Zakaria, R. - Ahmad, M. H. (2013) The performance of hybrid ARIMA-GARCH modeling in forecasting gold price, In 20th International Congress on Modelling and Simulation, Adelaide, pp.1-6.

sciendo

Slovak Journal of Civil Engineering

Vol. 30, 2022, No. 1, 42 – 48
DOI: 10.2478/sjce-2022-0005

NUMERICAL STUDY ON THE EFFECT OF WATER WAVES AND DEPTHS ON INCLINED BRACES WITH RESPECT TO THE STABILITY OF VLFS PLATFORMS IN THE CASPIAN SEA

Ali MOASAMI[1], Bahador FATEHI-NOBARIAN*[2], Yousef HASSANZADEH[3]

Abstract

Very large floating structures (VLFSs) have various applications, such as recreational applications, port facilities, etc. A surge in the population, the advantages of building floating structures compared to traditional methods of land extraction from the sea, and the development of construction technologies, have led to engineers paying attention to very large floating structures. Bracing systems are capable of controlling and reducing the horizontal responses of a floating platform, but they have no major impact on its vertical responses. In the present study, the semi-floating platform was numerically designed to be least affected by the three factors of wave force, horizontal torsion, and horizontal displacement. In order to optimize the design, the semi-floating platform was simulated and subjected to the three wave directions with collision angles of 40, 45 and 55 degrees in the environmental conditions of the Caspian Sea and by exerting the wave effect in a Flow-3D model. Examination of the platform's movements has demonstrated that the arrangement of an eight-way restraint system with a 40-degree restraint angle responds better to the impact of waves and is more economical compared to other designs.

Address

[1] Master of Civil Engineering, Water Engineering and Hydraulic Structures, Islamic Azad University, Tabriz Branch, Tabriz, Iran.

[2] Assistant Professor, Department of Civil Engineering of Hydraulic Structures, Aras Branch, Islamic Azad University, Jolfa, Iran.

[3] Professor, Department of Water Engineering, Center of Excellence in Hydro informatics, Faculty of Civil Engineering, University Of Tabriz, Tabriz, Iran.

* ***Corresponding author:*** b.fatehinobarian@iaut.ac.ir

Key words

- Very Large Floating Structures (VLFS),
- Flow 3D Model,
- Bracing Lines,
- Floating Platform,
- Horizontal Platform Displacement.

1 INTRODUCTION

Very large floating structures (VLFSs) have always attracted the interest of architects, designers, urban planners, and engineers, because these structures, unlike those made with conventional construction methods, provide an environmentally friendly solution to creating land on water. Applications of very large floating structures include floating docks, floating hotels, floating fuel storage facilities, floating bridges, floating airports, and even floating cities; they have led to extensive research over the past two decades. VLFS structures can be divided into two general categories: 1) Semi-floating VLFS structures, and 2) Floating VLFS structures. Since there are many types of VLFS structures, it is more useful to classify them spatially. From such a spatial perspective, two major groups of very large semi-submerged structures that can be named are: 1) Coastal VLFS and 2) Offshore VLFS.

Fig. 1 *Mega-Float structure, Gulf of Japan (https://web-japan.org/atlas/technology/tec14.html(*

Between 1995 and 2001, a Mega-Float (experimental 1km floating runway) (Fig. 1) was designed and implemented in Tokyo Bay. Its performance was investigated in order to develop and examine the accuracy of VLFS technology for use in a floating airport. The findings of that study suggested that the use of VLFS technology in the construction of floating airports, including maintaining the radius of the curvature of the runway at a height of 10 km, is feasible.

The integrity of the positioning system is a key factor in the successful design of semi-floating structures. The positioning system of a floating structure can be either single-point bracing or extensive bracing. Another type of positioning system is dynamic positioning. Rashidi et al. (2015) focused on the following results: the mechanism of wave loading on a platform is such that when the wave length is equal to the distance between the columns, the induced force in the front and rear columns is in one direction, and the cumulative effect of these forces leads to a strong force in the direction of the surge. Ohmatsu (1998) focused on presenting an effective design for calculating the hydro-elastic response induced by a wave over a very large pontoon type floating structure that is close to a breakwater.

The numerical computation method is the same as previously; it was prepared by the same author for a VLFS in free water (without a breakwater) (Parizadeh and Khanjani, 2017). The new method was developed in such a way that it encompassed the hydrodynamic interaction between the breakwater and the floating structure. Ali Karimi and Saeed Rahmanlou (2015), in a report issued by the Caspian Oil Company in the scientific-promotional monthly Oil and Gas Exploration and Production No. 130, outlined the design and containment challenges in the deep waters of the Caspian Sea. In this report, in addition to introducing the specifications of the Amirkabir platform, the only semi-floating platform in Iran, they discussed how to anchor the platform, and how to determine the effect of environmental forces on the stability of the platform. In Ketabdari et al. (2018), the following items were highlighted: Apar is a floating platform used in deep and super- deep waters. In this paper, the effects of a restraint line alignment on the hydrodynamic response of a truss spar platform on a real scale were studied numerically using a dispersion theory. Wang and Tay (2011) conducted an extensive study with a focus on mega structures and considered their development. Watanabe et al. (2004) found that the construction of this type of structure is easy and rapid. VLFS structures can be easily developed. Moreover, these structures are not affected by vibrating waves, since their basements are originally isolated. Utsunomiya et al. (1998) developed an auxiliary overlap method for rigid body movements and floating plate bending modes. The semi-floating structure is held above the water surface using tubular columns or elements of balancing structures. These types of structures are used for turbulent and long-lasting sea conditions. In contrast, their floating types or pontoons remain on the surface of the water like a large plate, so the stability of the pontoon in different dimensions and the maximum load induced by the floating structure must be calculated. The equilibrium in a floating structure is realized when the output forces and anchors on the structure are zero. When the floating structure is tilted by an angle (a), the center of the float (b) will shift. As the mass is floating (Fig. 2), the intersection of the buoyancy force and the axis of symmetry is called the metacentre (M). It is clear that a rectifying torque occurs when the metacentre (M) is above the center of gravity (G). In other words, if the metacentre (M) is above the center of gravity (G), the structure is stable. The degree of stability depends on the distance between (M) and (G), which becomes the height of the metacenter (*hm*). As the height of the metacenter becomes greater, the more stable the structure and the lower the deflection angle of the structure that can be expected (Parizadeh and Khanjani, 2017).

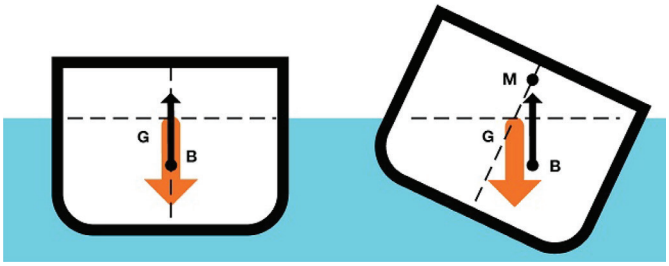

Fig. 2 *Different metacentric states*

In an equilibrium vessel, the torque generated by the eccentric force is equal to the rectifying torque. An off-center force deflects the structure until equilibrium is established. By calculating this value for different structures, their stability can be compared. The floating structure is usually held in place by bracing, vertical elongated tendons, dynamic position stabilization or a combination thereof.

In the present study, the modeling of an installation platform with a different bracing arrangement has been done without the need for retaining pontoons. One of the distinctive aspects of this research is that it is a single deck, and it is balanced against wave forces. All the environmental forces, waves, water flow and wind have an insignificant impact on its operation.

In other words, symmetrical systems can maintain the position of the platform against environmental forces entering from different directions by using the symmetry and homogeneous distribution of lines in different directions. Indeed, all control of the vertical floating responses determines the dimensions and shape of the floating platform, and in order to reduce these responses, the platform should be optimized. Designing a suitable bracing system and a suitable layout pattern is one of the most important parts of designing a semi-floating platform.

2 MATERIAL AND METHODS

The FLOW-3D model is one of the most powerful models in the field of computational fluid dynamics; it was developed and supported by Flow Science. The FLOW-3D model features many physical patterns, including shallow water, viscosity, cavitation, turbulence, porous media, etc. This model is used in fields such as casting, process engineering, hydraulics, the environment, aerospace, marine science, oil, gas, etc. The Volume of Fluid (VOF) and Fraction Area Volume Obstacle Representation (FAVOR) methods are examples of non-volumetric methods.

In these methods, the region to be modeled is first divided into a network of smaller elements or volumes of controls. For fluid-containing elements, the numerical values for each of the flow variables such as pressure, temperature, and velocity are stored within them. These values usually represent the volumetric average of the values in each element. The great advantage of the VOF method is that the fluid flows through a fixed network, and there is no deformation or displacement of the network. The

FAVOR method is another volumetric technique that is used to determine the geometry. Just as the volumetric component of a fluid is adopted to determine the position of the fluid surface inside each grid cell, a quantitative component other than the volume can be used to determine the surface area of a rigid body.

2.1 Governing equations for common fluid levels and free surfaces

In general, the fractions of area and volume in a Flow-3D model are independent of time. However, when it comes to the model of moving obstacles, these quantities may change over time. The fluid position is defined in terms of the volume of the fluid of the function (*F (x, y, z, t)*). This function represents the volume of fluid #1 per unit volume as the following equation:

$$\frac{\partial F}{\partial t}+\frac{1}{V_F}\left[\frac{\partial}{\partial x}(FA_x u)+R\frac{\partial}{\partial y}(FA_y v)+\right.$$
$$\left.+\frac{\partial}{\partial z}(FA_z w)+\xi\frac{FA_x u}{x}\right]=F_{DIF}+F_{SOR} \quad (1)$$

Where:

$$F_{DIF}=\frac{1}{V_F}\left[\frac{\partial}{\partial x}\left(\upsilon_F A_x\frac{\partial F}{\partial x}\right)+R\frac{\partial}{\partial y}\left(\upsilon_F A_y\frac{\partial F}{\partial y}\right)+\right.$$
$$\left.+\frac{\partial}{\partial z}\left(\upsilon_F A_z\frac{\partial F}{\partial z}\right)+\xi\frac{FA_x u}{x}\right] \quad (2)$$

In the Cartesian coordination system, R is equal to 1, and ξ is equal to zero, while in a spherical coordination, it is equal to 1. F_{SOR} denotes the equation of mass continuity and the scatter of turbulence, and FA_z is the flow cross section in the z direction in Cartesian coordinates (m^3). F is the volume occupied by the fluid for the locations where F= 1.0, and the fluid and locations are F= 0 and a hole. V_F is the fluid volume in the defined path (m^3); υ is the symatic movement (m^2/sec). u, v and w are the velocity parameters in the Cartesian direction, and T is the time (sec).

The diffusion coefficient is $\upsilon_F=\frac{C_F\mu}{\rho}$, where the C_F coefficient is a constant, and its inverse is sometimes attributed to the Schmidt turbulence number. These scatter plots are used only to mix two turbulent fluids whose distribution inside the field cells is expressed by the F function. The term F_{SOR} refers to the R_{SOR} density source in the mass continuity equation. F_{SOR} is equal to the time rate of the change of the fluid # 1 fraction, due to the mass source # 1.

2.2 The Navier-Stokes Equations of the Mean Time Reynolds Averaged Navier Stokes (RANS)

The basis of the governing equations is the same for solving the turbulence and turbulent flows, and the continuity and Navier-Stokes equations were adopted. The difference is that to solve the turbulent flow, the Navier-Stokes equations are averaged over time. To investigate the turbulent flow, it is best to first break down the momentary properties of the flow (for example, the velocity and pressure components) into an average and an oscillating value:

$$u_i=\bar{u}_i+\acute{u}_i \quad (3)$$

$$p_i=\bar{p}+\acute{p} \quad (4)$$

In the above relationships, the first parameters on the right side are the mean time values, and the second parameters are the oscillation values.

2.3 Model properties

Tab. 1 presents the geometric characteristics of the platforms modelled in this research based on the placement and number of restraints.

In this research, 6 or 8 braces have been used for 8 different models to control the stability of the floating platform; also this amount of braces was placed on the platforms based on the position and the wave direction in the Caspian Sea. For a better description, it can be stated that in the second row model in Tab. 1, the distance between the braces is considered equal, but in the seventh row model in Tab. 1, the distance between the braces was not the same and equal, but to avoid any possible interference between the two models, i.e., for the model of row 2 and the model of row 7, the term NEW has been used. However, it should be noted that the distance between the braces in this study was not the main focus; the main focus was on the type of arrangement of the braces and their connection angle, which is mentioned in the results section.

As can be seen in Tab. 1, a total of 8 different models with different angles of floating platforms have been designed and modelled based on the type of wave movement in the Caspian Sea. With regard to the first model, eight articulated braces maintain the balance of the

Tab 1. *Geometric characteristics of the modelled platforms*

Row	Platform dimensions (m)	Name of Model	Number of braces in X direction	Number of braces in Y direction	Angle in direction of X (degree)	Angle in direction of Y (degree)	Mode of connection to bottom
1	97*79	(45-8)	6	2	45	45	Ring joint
2	97*79	(45-6)	6	0	45	0	Ring joint
3	97*79	(40-8)	6	2	40	40	Ring joint
4	97*79	(40-6)	6	0	40	0	Ring joint
5	97*79	(55-8)	6	2	55	55	Ring joint
6	97*79	(55-6)	6	0	55	0	Ring joint
7(New)	97*79	(45-6)	6	0	45	0	Ring joint
8	97*79	(45-4) (40-2)	6	0	(4-45 & 2-40)	0	Ring joint

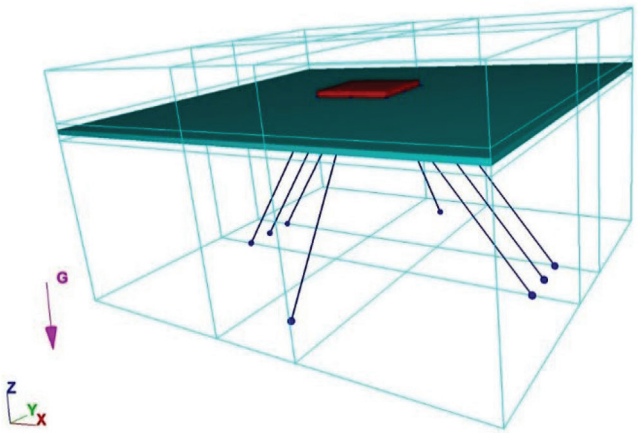

Fig. 3 *Placement of braces in the model (40-8)*

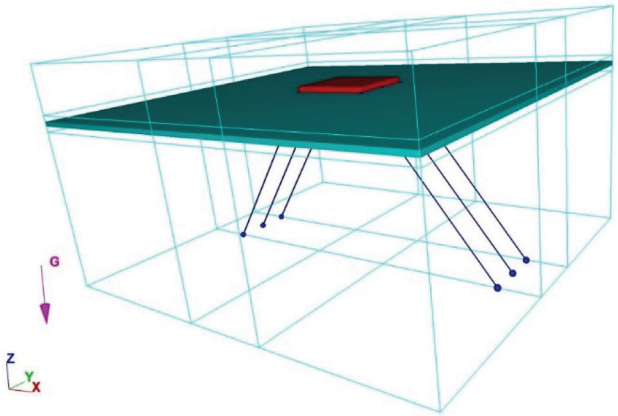

Fig. 4 *Placement of braces in the model (40-6)*

platform with angles of 45° to the sea floor, which is mainly due to the trajectory and direction of the surface wave and subsurface waves of the Caspian Sea, which is often in the x direction. Eight types of symmetrical bracing system arrangements in the form of 6 and 8 braces have been used to evaluate the best bracing models. It should be noted that the predominant wave direction in the Caspian Sea is in the (x) direction; in the performed models, it has been assumed to be the same. Therefore, the main direction of the platform design in this research is the direction (x), but in all the models, the direction perpendicular to it (y) has also been scrutinized.

For example, two models that performed with the connection details of the braces f in this research are shown schematically in Figs. 3 and 4.

2.3.1 Boundary Conditions

The boundary conditions for the transfer equations of the quantities of turbulence are included in the equations of the two-equation models, through the surface components. For instance, all the displacement and diffusion fluxes at the solid boundaries, where the open surface components were lost, are automatically considered to be zero. On the free surface, the tangential stresses become zero due to the loss of velocity derivatives. In the same study, it was assumed that the tangential stresses at the wall boundaries are zero due to the zero flow rate. However, the tangential shear stresses of the wall compensate for them. These stresses occur in the quiet substrate and are proportional to the molecular viscosity and local velocity gradients. Therefore, the shear stresses of the wall can be included in the expression of turbulence (P_T). Unfortunately, in all the cases, this approach is not responsive and does not confine the k_T values well near the boundaries. In the FLOW-3D model, the values of k_T specify that in each cell of the network, part or its entire surface should be surrounded by a rigid boundary. In the usual method for determining the boundary values for k_T quantities, the local equilibrium between the production processes and the declining shear stress is assumed, and a wall velocity profile law is assumed, whose values are calculated in relation (5), which is used to assign the k_T values in the center of the cell as the optimal boundary condition.

$$k_T = \frac{u_*^2}{\sqrt{CNU}} \quad \text{and} \quad \varepsilon_T = \frac{u_*^3}{\kappa d} \tag{5}$$

There are a total of 10 different boundary conditions in the Flow-3D numerical model, which can be used for models. Each of these boundary conditions has a specific function, all of which are activated from the boundaries section of the Flow-3D model. In the VLFS computational model, the same boundary conditions are used to define different environments.

3 RESULTS AND DISCUSSION

The key results of the studies applied to these models are given in the stabilization diagrams of the pressure convergence ratio and the level measurements in Figs. 5 through 7. According to the stability diagrams and the time step within the defined time range for

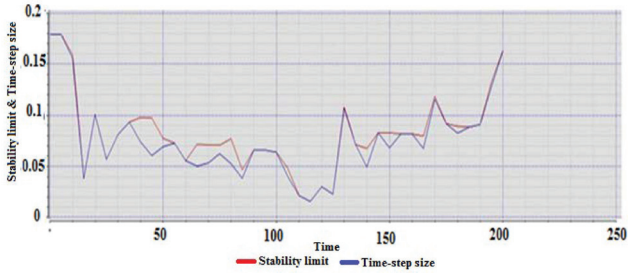

Fig. 5 *Diagram of stability measurement based on the time steps for the model (40-8)*

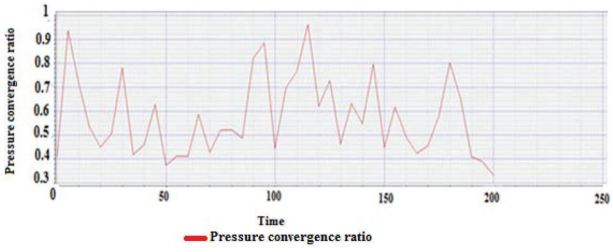

Fig. 6 *Diagram of the pressure convergence ratio based on the time steps for model (40-8)*

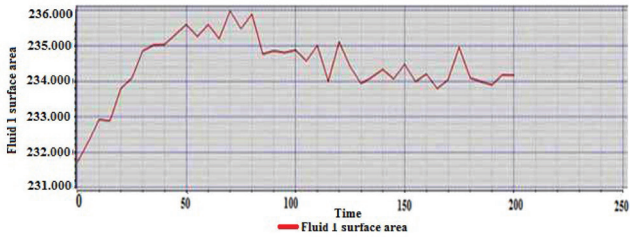

Fig. 7 *Time step diagram based on the time steps for model (40-8)*

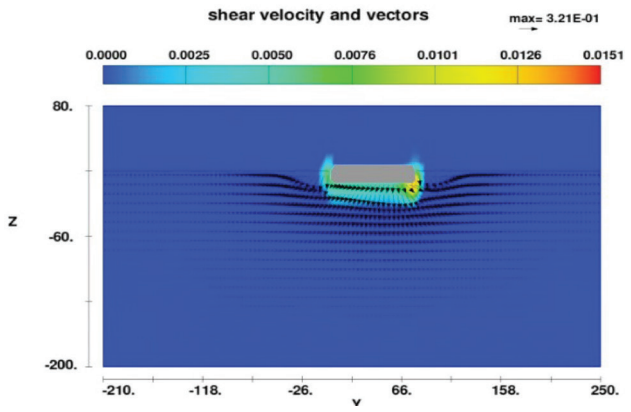

Fig. 8 *Contour display of the cutting velocity for the (z-y) axis in the model (40-8)*

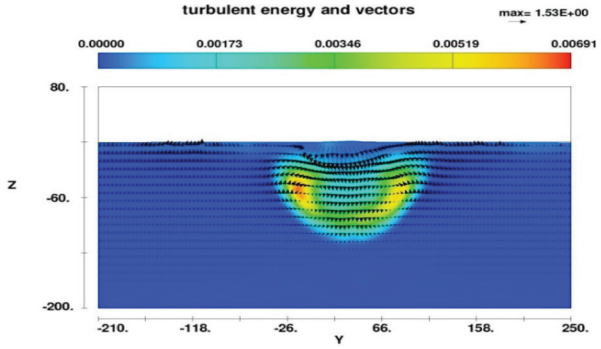

Fig. 9 *Contour display of turbulence energy for the (z-y) axis in model (40-8)*

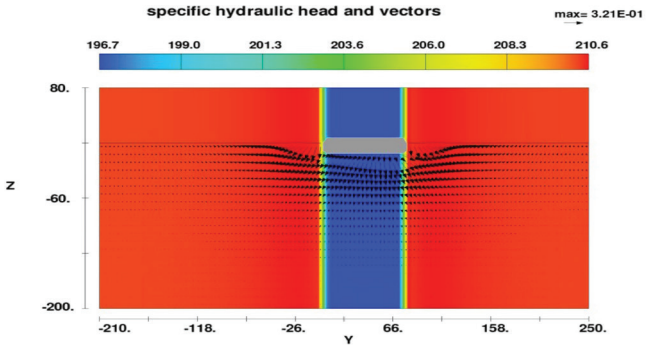

Fig. 10 *Contour display of the total head for the (z-y) axis in model (40-8)*

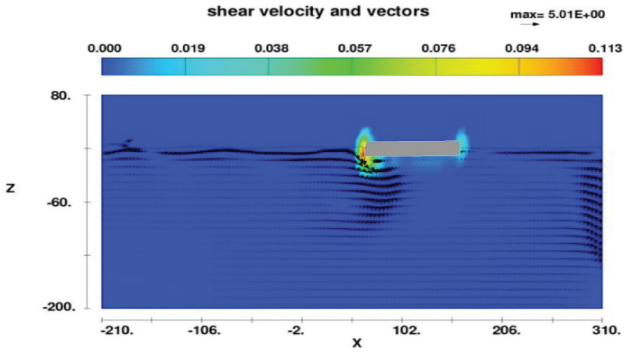

Fig. 11 *Contour display of the cutting velocity for the (z-x) axis in model (40-8)*

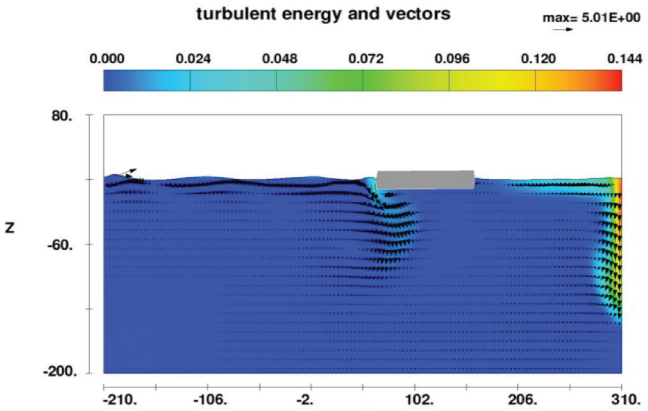

Fig. 12 *Contour display of the turbulence energy for the (z-x) axis in model (40-8)*

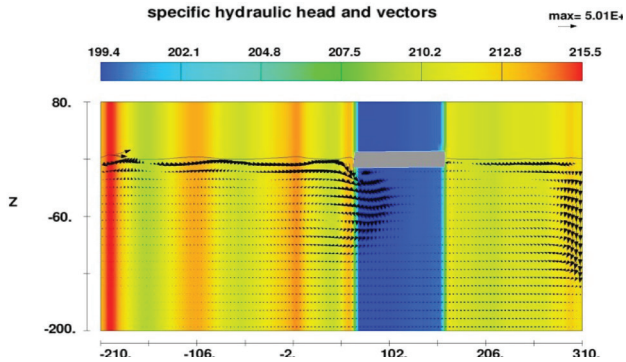

Fig. 13 *Contour display of the total head for the (z-x) axis in model (40-8)*

modeling, the model's equilibrium is depicted showing resistance to the hydrodynamic forces of the wave current. This adaptation has its highest value in the model (40-8) which can be seen in Fig. 5. It should be noted here that the model (40-8) means that in this model, 8 braces, which are connected to the sea floor at an angle of 40 degrees are used. In normal numerical modeling conditions and without considering the validation diagrams, the results of model number (40-8) can be considered as the best mode for the results obtained. However, in the following sections, the same results have been clearly demonstrated in the validation diagrams.

The best conditions for the stability and conformity of the diagram show that based on diagram (7), which is related to the measurement of the simulation level, it can be seen that the resonance rate is low. In Figs. 8 to 13, the cut-off of the velocity and turbulence energy meter for all the models is shown to perform in two directions, namely, (*z-y*) and (*z-x*). The platform moved horizontally due to the impact of the waves, but did not rotate around the axis perpendicular to the floor of the platform. Hence, this model can be opted as the best mode for a stagnation (static mode) state of a platform floating on the sea. It is worth stating that the counter display is not provided due to the over-rotation of the platform bottom and the upset in the balance, which resulted from the collision of waves in the models (new model: 45-6, in Tab. 1) and (model 8: 40-2 and 45-4, in Tab. 1).

As seen in the afore-mentioned diagrams, there is a desirable degree of compliance of the sustainability with the time steps in all the sustainability procedures accomplished, thereby implying the higher efficiency of the software in modeling this type of phenomenon.

3.1 Validation

For making a comparison between the modelling and the performed models, it is necessary to compare the outputs of the numerical model of the designed platform of the present study with the results obtained in previous studies. One of the most important platforms of this type is the Amirkabir Platform on the Caspian Sea, about which numerous studies have been carried out with a focus on its stability against the wave forces and depths affecting the platform. In the present study, with regard to the platform's nature, which is focused on the geometrical arrangement of the bracing lines and their placement in the sea, two general comparisons were done with the Amirkabir Platform.

1) The variations in wave velocity relative to the forces acting on the platform
2) The variation in resonance relative to the horizontal displacement of the platform section over the wave height

As mentioned before, one of the general objectives of this study is to reduce the horizontal resonance on the platform and mitigate the economical load of establishing a platform. Therefore, in comparison with the Amirkabir Platform, one of the suggested models of the present study exhibited more favorably compared to the other models. Diagram 14 illustrates the variation in wave velocity relative to the forces applied to the platform.

With regard to Fig. 14, the amount of variations for the wave velocity in model (40-8) showed a better degree of compliance with the results obtained for the Amirkabir Platform, and the distance was equal to 7 %. Other models showed a better degree of compliance with the results obtained for the Amirkabir Platform during the beginning of a wave collision's with a platform, when the velocity was close to 0.25 m/s for the models (40-8), (55-6) and (45-8). However, more divergence was observed in the other models, compared to the Amirkabir Platform, so that the distances between the results of the models (45-6) and (55-8), New (45-6) and (40-2 and 45-4) and (40-6) with the results of the Amirkabir Platform are as below; 21 %, 25 %, 16 %, 18 % and 20 %, respectively.

The distance of the models (55-6) and (45-8) from the Amirkabir Platform is equal to 12 % and 14 %, respectively, and the results obtained for model (40-8) showed the best compliance with the results of the Amirkabir Platform, among all the other models. As seen in the diagram, the placement mode of the platform in the developed models and also in the Amirkabir Platform is of the direction of the flow, which is in the x direction of Descartes for all the models. In another comparison, the amount of the variation for the resonance relative to the horizontal displacement of the platform is shown (Fig. 15).

Fig. 15 shows the position of the changes in resonance with respect to the horizontal displacement of the platform due to the impact of the waves. It can be observed that the least amount of horizontal displacement relative to the resonance variations induced by the wave force is related to model (40-8), which was modelled in three different categories of the model waves, and these three cases exhibited a lower displacement relative to the other models. Generally, the other models exhibited almost a 12 % or 26 % distance from the results of the (40-8) model. Hence, the (40-8) model, which was also shown in Fig. 14, is the best model among all the models of this study developed. The use of an arrangement array of the bracing cables of (40-8) model is therefore suggested, since this model is capable of stable sustainability with the least amount of displacement for the industrial facilities in regions like the Caspian Sea.

4 CONCLUSION

In general, eight numerical models in this research have been examined for the design of floating platforms, each of which has its own properties.

In the present research, which is based on the structure of the Amirkabir Platform, which was constructed in the Caspian Sea, a different but practical model has been proposed; it is much more capable than the Amirkabir. From all the different models, which have different structures, and all the numerical models of the floating platform, proposed in the Flow-3D model, one of which is mentioned as the best model because it exhibited the least amount of displacement against lateral waves.

1. Model (40-8) shows a better degree of adaptation than the other models; this distance was about 7 % compared to the results of the Amirkabir Platform.

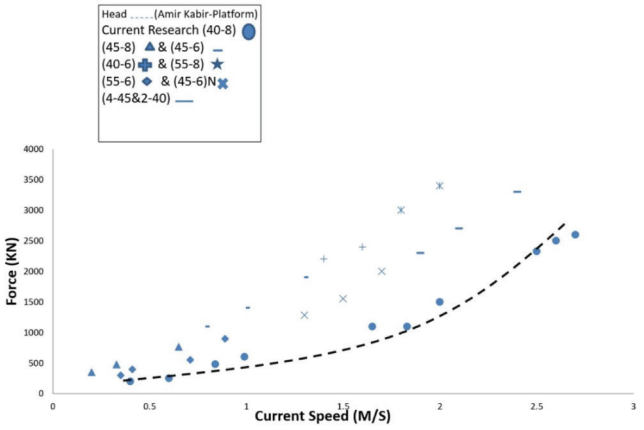

Fig. 14 *Variations in wave velocity relative to the horizontal forces acting on the platform*

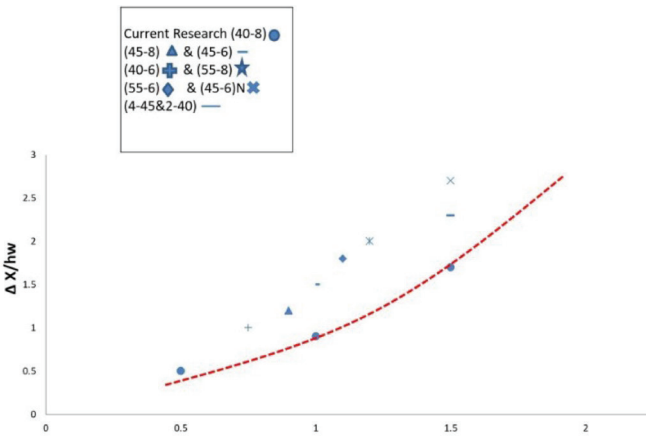

Fig. 15 *Amount of variation of the resonance relative to the horizontal displacement of the platform from the height of a wave*

2. According to Fig. 14, at the beginning of a wave collision's with a platform, i.e., near a velocity of 0.25 m/s, the models (40-8), (55-6) and (45-8) show a better adaptation compared to the results of the Amirkabir Platform.
3. The results of models (45-6) and (55-8), (45-6), (40-2 and 45-4), (40-2 and 45-4) and (6-40) with the results of the Amirkabir Platform have the following intervals, respectively: 21 %, 25 %, 16 %, 18 %, and 20 %; that the distance of the models (55-6) and (45-8) are 12 %, and 14 % respectively with the results obtained for the Amirkabir Platform.
4. In diagram (15), the model (40-8) has the lowest amount of horizontal displacement compared to the other models. The other models have a distance of about 12 % - 26 % with the least amount of displacement. Therefore, the capability of the model (8-40) is demonstrated in this diagram.

REFERENCES

Flow 3-D User Manual, Version 9.3

Karimi, A. - Rahmanlu, S. (2016) *Control of the Amirkabir semi-submersible platform in deep waters in the Caspian Sea, challenges, design and implementation*. Scientific Journal of Exploration & Production Oil & Gas, Vol. 130, pp. 6-10 [in Persian].

Ketabdari, M. J. - Bakhtiari, M. - Ghassemi, H. (2018) *Numerical analysis of the effects of mooring line configurations on the dynamic response of a truss spar platform in sea waves*. Iranian Journal of Science and Technology: Marine Technology, Vol. 5, pp. 53-62.

Ohmatsu, S. (1998) *Numerical calculation of hydroelastic behavior of VLFS in time domain*. In: *Proceeding of 2nd International Conference on Hydroelasticity in Marine Technology,* Fukuoka, Japan.

Parizadeh, A. - Khanjani, M. J. (2017) *An Experimental Study on the Effect of Gill Cells on Very Large Floating Structures*. Journal of Ferdowsi Civil Engineering, Vol. 28, No. 2, pp. 57-76. https://doi.org/10.22067/civil.v28i2.37882

Rashidi J. - Ahmadi, A. - Seif, M. S. - Azarsina, F. (2015) *Experimental study of Creelov-landing force due to regular wave refraction on a semi-floating platform*. Sixth International Offshore Conference, Sharif University of Technology, Tehran, Sharif University of Technology.

Utsunomiya, T. - Watanabe, E. - Eatock Taylor, R. (1998) *Wave response analysis of a box-like VLFS close to a breakwater*. In Proceedings of the International Conference on Offshore Mechanics and Arctic Engineering - OMAE ASME.

Wang, C. M. - Tay, Z.W. - (2011) *Very Large Floating Structure: Applications, Research and Developmen*t. Procedia Engineering, Vol. 14, pp. 62-72.

Watanabe, E. - Wang, C. M. - Utsunomiya, T. - Moan, T. (2004) *Very large floating structures: Applications, analysis and design*. CORE Report No. 2004-02; National University of Singapore.

https://web-japan.org/atlas/technology/tec14.html

sciendo

Slovak Journal of Civil Engineering

Vol. 30, 2022, No. 1, 49 – 56
DOI: 10.2478/sjce-2022-0006

EFFECTING THE RHEOLOGICAL PROPERTIES OF COMPOSITES FOR 3D PRINTING TECHNOLOGY IN CONSTRUCTION

Adam UHLÍK[1]*, Mário BUCH[1], Stanislav UNČÍK[1]

Abstract

The article deals with the factors that lead to the beginnings of the solidification and hardening of materials used in 3D home printing technology in construction. At the beginning, the composition of the materials as well as their essential fresh and hardened properties and the performance assumptions of such a mixture are described. Subsequently, the article discusses the main aspects of the rheology and hydration of cement composites and the use of additives such as superplasticizers, viscosity modifiers, and acceleration and retardation additives, which directly affect the onset of the setting of such materials and the strength of the resulting mixtures. Finally, we describe the printing and curing process of the extruded material, which is divided into 4 main phases from the pumping and extrusion of the material through the initial deposition of layers to a sufficient increase in strength in the required time.

Address

[1] Dept. of Material Engineering and Physics, Faculty of Civil Engineering, Slovak University of Technology in Bratislava, Bratislava, Slovakia

* ***Corresponding author:*** adam.uhlik@stuba.sk

Key words

- 3D printing,
- Technology,
- Material,
- Composite,
- Additives,
- Solidification rate,
- Structural strength.

1 INTRODUCTION

Adaptive manufacturing technologies have brought about new opportunities for many dynamically developing industries. Thanks to its versatility, 3D printing technology has the potential to take construction technology to another level and therefore has a great future in construction. The automation of construction processes can result in a reduction in manpower, which increases safety on a construction site and shortens the construction time and the production costs. The material used for such technology is 3D extruded cement composite, a special type of concrete that can be applied by a 3D printer layer by layer without any formwork support. Its important technical properties and technological parameters, including its workability, setting time, and mechanical properties, can be optimized by the appropriate selection of composite material and the setting of the printing parameters. To date, many building structures have been successfully extruded using 3D printing technology; 3D extruded concrete composite therefore has great potential in practical applications for future construction applications, such as affordable construction in developing countries or as a technology for rapidly built housing for socially disadvantaged groups.

2 CONCRETE MATERIAL FOR 3D PRINTING IN CONSTRUCTION

For the production of houses and structures in construction using the new 3D printing technology, it is best to use a special concrete material (a cement-mortar composite). Additives and admixtures also play an important role in the composition of such a special composite; these are present in the materials together with aggregates, cement, and water, and are added to improve the selected material´s properties. Such material must be compatible with the 3D printer and the respective nozzles with which the material will be extruded (Zhang, J., et. al., 2019). When designing a cement-mortar composite mixture suitable for the 3D printing of houses, it is necessary to ensure that such a material meets the performance requirements of fresh and hardened mixtures.

Fig. 1 *Example of material and extruded construction using 3D concrete printing (Source: Kauppila I., 2021, CreaBeton Materiaux, 2019)*

According to (Luo, W., et. al., 2020), additives can significantly change the properties of fresh or hardened concrete composites. The suitability of a material for 3D construction printing technology depends on three main interacting factors: the choice of raw materials, the application methods and the production methods. When composing the mixture, the climatic conditions at the construction site must also be taken into account. The time after which the given properties will be achieved also affects the printing process; this further depends on the method of the material´s delivery and the time of the application of other layers of material. As mentioned above, when designing a material for such a technology, attention must also be paid to the properties that affect the methods and quality of the printed object. As (Ngo, T. et. al. 2018) noted, particular attention should be paid to parameters such as extrudability, pumpability, and buildability as well as the bonding time and strength of the layer and the shrinkage of the concrete.

3 THE MOST IMPORTANT FACTORS AFFECTING THE SETTING SPEED OF BUILDING MATERIALS FOR 3D CONCRETE PRINTING

The setting of a composite material´s solidification affects the entire final construction of the printed element. This is called feasibility, which is affected by the correct extrusion of the material from the printer nozzle and which requires a long "opening time". Otherwise, the material would become stiffer and cause the mixture to flow more slowly through the printer's power system, thereby causing its clogging and blocking. In addition, the long opening time helps to bond the material between the layers, but this can adversely affect the formation of the printed elements (Van Der Putten, J., et. al., 2019). A short interval of time is required when joining the upcoming layers of material to maintain the shape and load of the higher layers applied. The strength and stiffness of the extruded shape are obtained due to the increased density of the composite by using finer powders such as Portland cement. The strength of the mixture is also affected by the water-cement ratio, the strength class of the cement, the quality of the aggregates, and the use of admixtures and additives. When designing such material, the need for proper extrusion of the material and the factors that affect the processability and open pumping time of the material must be taken into account.

The key properties of hardened concrete are its compressive and flexural strength. In this context, it can be concluded that the concrete composite for the 3D printing of houses must have the following properties: high strength at an early age, good bonding between the layers, and sufficient final strength to hold the following layers (Ngo, T. D., et. al., 2018). In order to acquire these properties, complex modifiers and admixtures, such as superplasticizers, viscosity modifiers, accelerators, and retarders, must be used in the right proportions in the concrete mixes, as well as the rheology and hydration of the cement.

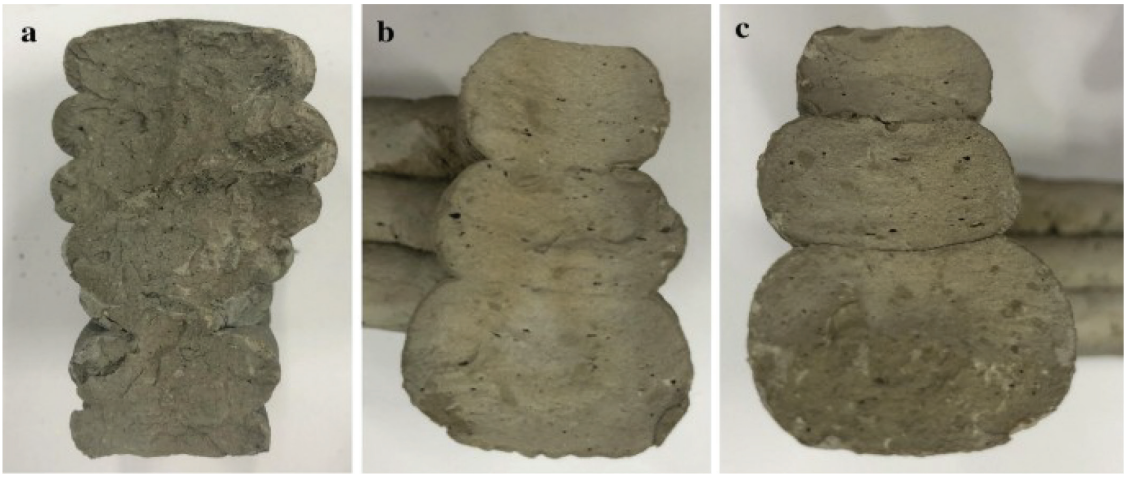

Fig. 2 *Printed samples with a time interval of a) 15 min, b) 30 min and c) 60 min (Source: Jun J. H., J. et. al., 2020)*

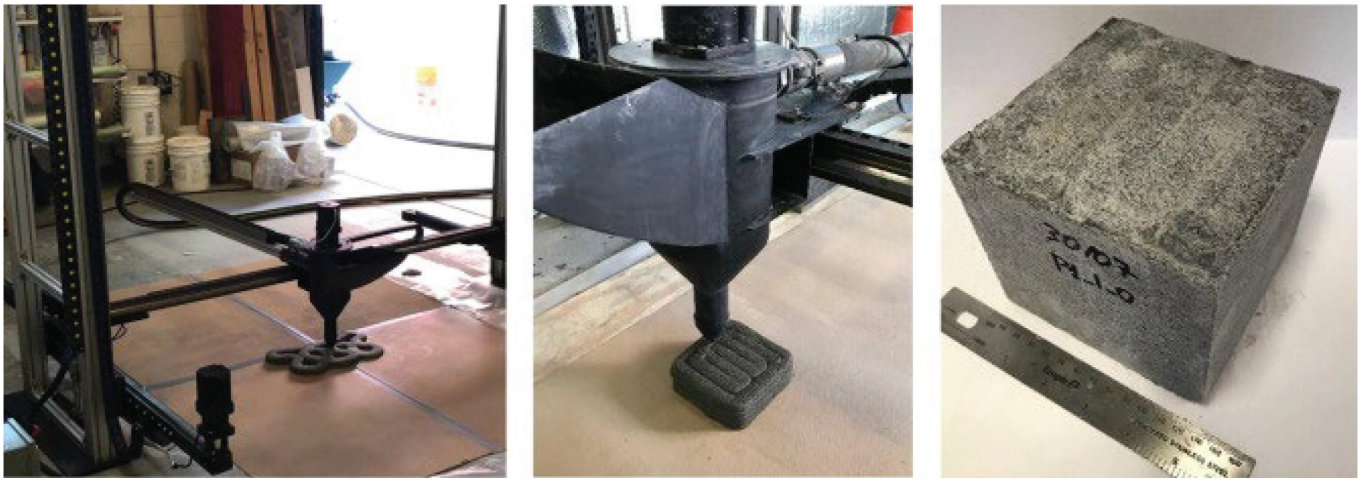

Fig. 3 *Examples of the 3D printing process and details of the material composite after solidification (Source: Murcia Heras, D., M. et. al., 2020)*

4 ASPECTS OF THE RHEOLOGY AND HYDRATION OF CEMENT

Controlling the rheological properties of materials for the 3D printing of houses and structures is essential in terms of the good extrudability and buildability of the fresh material, as it will determine the efficiency or failure of the printing process during construction. The hydration kinetics must be delayed and affected in a relatively extreme way so that the material does not harden during the printing process, does not dissipate immediately after application, and can bear its own weight and consequently the weight of the deposited layers of material. Using special rheology, there must be a balance between fluidity during printing and the rate of curing immediately after the application.

The rheology of concrete materials is generally influenced by the design (composition) of the mix, including the volume fraction of the bonding system, its composition (e.g., the presence of additional cementitious materials), and the attributes of the aggregate (i.e., the particle´s size, distribution, and shape). Ingredients can be used as an effective tool for adjusting the appropriate rheology. Superplasticizers, which act as dispersants (plasticizers) to reduce ultimate stress, and viscosity modifiers, which increase the viscosity of the material, are now regularly used in various concrete materials to control their feasibility. Printed material for additive production. The key factor for successful 3D printed material is controlling its rheology through the selection of suitable additives in the most appropriate ratio and combination (Marchon, D., S. et. al., 2018).

5 THE MAIN ADDITIVES AND ADMIXTURES USED IN 3D COMPOSITES

5.1 Superplasticizers

Superplasticizers are polymeric dispersants used in cementitious materials to reduce yield stress and viscosity. These are concrete admixtures that improve the workability and cohesiveness of the mixture without increasing the water content. For mixing and casting, it is necessary to increase the workability of the material and the extrusion in the 3D technology. In addition, it allows for a decrease in liquid content at a constant yield limit, which can reduce the porosity of the hardened material and increase its mechanical properties, performance, and service life. Therefore, most 3D printing materials in construction use a filler without any coarse aggregates; therefore, the volume of the finer particles increases. Lignosulfonates are natural polymers with a relatively modest ability to reduce water (Papachristoforou, M., et. al., 2018). This is due to their robustness and ability to induce good extrudability but still retain their shape within seconds of the initial casting. These properties are in great demand in the extrusion of a 3D printed composite. The most effective superplasticizers for current use are polycarboxylate ethers (PCE).

According to (Marchon, D., et.al., 2018) these admixtures can significantly reduce the need for the water and cement content and can reduce viscosity and shrinkage; they are very effective for ensuring the high strength and durability of the material.

5.2 Viscosity modifiers

Viscosity modifiers are commonly used in the construction industry; they are used to control the water transfer and porous structure in both fresh and solidified states. They improve cohesion and reduce the tendency of concrete material to segregate. The most commonly used viscosity modifiers in cement systems are cellulose and ether derivatives. Such admixtures are necessary to control and affect the high degree of segregation for liquid concretes, which in some cases improves water retention to promote particle flocculation and is therefore very promising for use in 3D technology (Papachristoforou, M., et. al., 2018). They can also increase the yield strength of cementitious materials and effectively reduce the deformation of the material at its own weight, which is crucial for the production of concrete additives.

5.3 Accelerating and retarding additives

Concrete admixtures are substances that are added in small quantities in order to affect the properties of fresh or hardened concrete. Retarding additives are used to compensate for the effect of higher temperatures, which shorten the setting time, or to avoid complications if the time between mixing and laying the concrete is prolonged. (Myrdal, R., 2007) pointed out that in order to

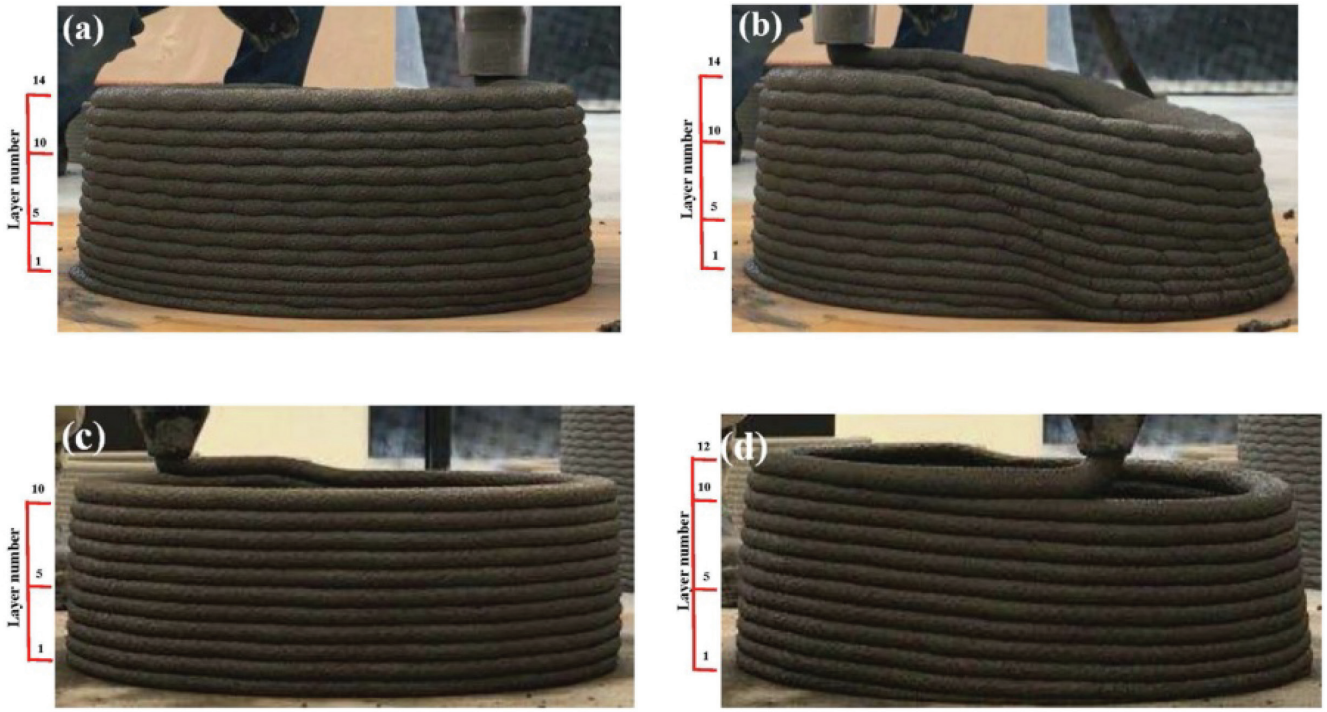

Fig. 4 *Different types and numbers of layers of a composite; high viscosity and collapse of a structure (Source: Jayathilaka, R., et. al., 2020)*

accelerate the hydration of the cement, to shorten the setting time of the cement, and, in most cases, to accelerate the development of the initial strengths, accelerating admixtures are used.

Accelerating additives are substances that accelerate the hydration of cement, shorten the setting time of cement, and, in most cases, accelerate the development of the initial strengths. Acceleration of the cement's is hydration is achieved in various ways and can be divided into physical and chemical effects. The first physical effect we can consider involves the desorption of retardants from the reacting surface, as in the case of sucrose in the presence of portlandite. Alkali metal hydroxides, carbonates, aluminates or silicates are essential components of setting accelerators. They provide a strong but basic reaction in a solution. According to (Myrdal, R., 2007), the acceleration of cement hydration is achieved with C3A, which releases a considerable amount of heat and insoluble calcium salts. The elevated temperature leads to accelerated C3S hydration, which results in increased initial strengths, but usually does not lead to increased long-term strengths. Some salts of strong acids and weak bases (e.g., aluminum chloride), which accelerate the hydration of alite, can cause rapid solidification at higher doses. A partial increase in the initial strength is usually recorded. In the case of a pressed concrete composite, it is very important to adjust the setting acceleration as soon as the concrete is extruded. This is ensured by accelerators that are composed of aluminum salt or alkali-free accelerators. Due to the high concentration of aluminum and sulphate, non-alkaline accelerators accelerate the precipitation of ettringite, which causes rapid flocculation of the system and allows for the stacking of several layers. Therefore, this principle is used in additive production in cases where a very fast setting of the solidification of the material is required.

Retarding additives are used wherever it is necessary to

Fig. 5 *Different types of additives (superplasticizers, viscosity modifiers, accelerators and retardants) for use in 3D printed materials, and a sample printing process after adding the retarding additive (Source: Mastercivilengineer, 2021, Digital manufacturing experts, 2020)*

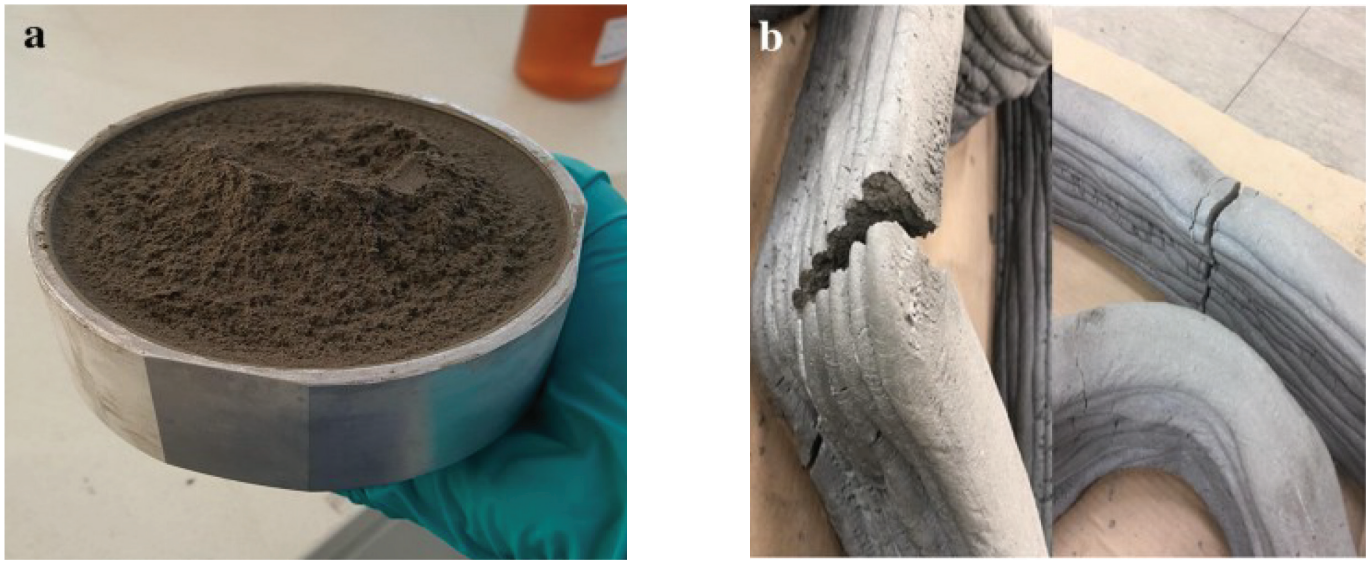

Fig. 6 *Shrinkage cracks, which are very undesirable, must be eliminated by a suitable composition of the printed material (Source: Jun, J. H et. al., 2020)*

compensate for the effect of higher temperatures, shorten the setting time, or avoid complications if the time between mixing and laying the fresh concrete is prolonged. Slowing down the hydration of the cement can be achieved by adding chemical additives. They prolong the induction period by delaying the onset of solidification, but once the onset occurs, the reaction rate usually accelerates during the acceleration period. This prevents the imperfect joining of successive concrete layers and the excessive heating of massive structures due to the heat of the hydration of the cement.

Retarding admixtures for 3D building printing materials are based on lignosulphonic acids and their salts, hydroxycarboxylic acids and their salts, sugars and their derivatives, or inorganic salts. Organic acid retardants and their salts are adsorbed on the C3S surface and slow down the initial rate of hydration by prolonging the course of the reactions in the first hours of hydration (prolonging the induction period). They therefore prolong the setting time of Portland cement. Subsequent hydration can be rapid; therefore, the development of the strength does not have to be significantly slower than when the additive is not used. The use of retarding additives leads to a reduction in the initial (one-day) strengths. If the retarding admixture is not solid, the strength after 7 days tends to be approximately the same as for concrete without an admixture, while 28-day and long-term compressive and tensile strengths tend to be higher than for concrete without an admixture (ASB, 2009).

6 CURING THE MATERIAL

In the 3D printing of concrete composites, the properties of the fresh mix during transport and pumping must be carefully checked to avoid any water loss. Indeed, the loss of water over time can negatively affect the degree of hydration, especially at low water/cement ratios, which can also negatively affect the adhesion between the applied layers and cause shrinkage disturbances.

Fig. 7 *Construction printed by a 3D printer at the Prague Technical University (Source: photos by the author: Uhlík, A. 2021)*

This shrinkage can adversely affect the final condition of the material. For example, the use of saturated light curing units or chemical compounds, such as expanding agents and shrinkage reducing additives, may be beneficial for additive manufacturing (Marchon, D., et. al., 2018). Therefore, it is necessary that the solutions be unique for the additive production of 3D technology in construction. For example, curing compounds may be used, but their effect on the adhesion properties between the printed layers must be taken into account for extrusion-based techniques. Water losses due to increased wind speed and/or the temperature during the printing must also be considered when printing at a specific location. The Apis Cor Company (3D Printing Progress, 2017) has therefore displaced a house in a temporary, temperature-controlled tent due to the low temperatures of the season and the climatic zone in order to avoid undesirable water losses during the 3D application. Another important factor in the use of impurities and alternative binders to control the rheology and hydration aspects of additive production will be ultimately necessary to consider their impact on the water transport properties of the material (Özalp, F., 2020).

7 THE PROCESS OF DEVELOPING THE CURING OF MATERIAL FOR 3D TECHNOLOGY IN CONSTRUCTION

The following paragraphs describe the main stages of the rheological condition of concrete used for 3D printing technology in construction. Fig. 8 schematically represents the expected development of the boundaries of pressed concrete by dividing it into four stages. The principle described below mostly focuses on the preparation of the material in batches with the activation of hydration. Continuous mixing of the material is also considered, but this is more difficult for ensuring the constant quality of the supply of the material. The material extrusion system, where the development of fluidity is expressed as, the yield stress (Pa), is divided into four main stages as shown in Figure 8. It should be clarified that the dynamic yield stress is the stress required to end the flow under shear, while the static slip limit is necessary to start printing from the beginning. For the material´s extrusion, the static slip limit is expected to be critical to the load-bearing capacity and dimensional stability (Marchon, D., et. al., 2018). Depending on the components of the material´s mixture, printing conditions and other parameters, the development of the flowability and solidification of the material can vary.

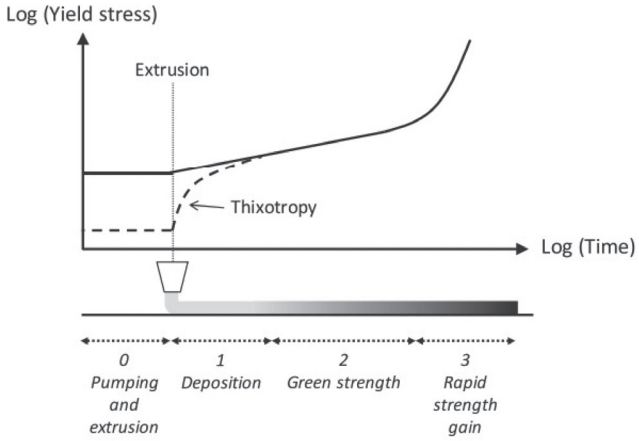

Fig. 8 *The static yield stress process, which is reported on a log-log scale in relation to the properties of the concrete to be printed. The direction of laying the concrete is schematically shown by moving from right to left, while the fresh concrete is light gray, and the hardening concrete is black. Phase 0 represents the time frame during which the fresh concrete is subjected to a high degree of shear during the mixing, pumping, and extrusion. Starting with the layering in stage 1, the concrete shows an internal structure at rest. The dashed line shows the structural formation in the presence of thixotropic agents (Source: Marchon, D., et. al., 2018).*

Such technology requires concrete materials with low initial stress values to provide easier control over various processing steps such as pumpability. The extrusion is described in step 0

Tab.1 Different *properties of concrete composites at different stages of printing using different types of additives (Source: Marchon, D., et. al., 2018).*

Stage		Concrete properties	Admixtures	
			Type	Targeted requirements
0	Pumping and extrusion	High fluidity	SPs (PCEs)	Dispersion
		Mix stability	VMAs	Water retention
1	Deposition	Rapid structural build-up to retain its own shape and weight	VMAs	Flocculation of particles
			(Nano-) clays	Flowability during extrusion, "House of cards" effect at rest
			Polymeric fibers	Shear thinning during extrusion, 3D structure at rest
			Entrained air	
2	Green strength	Controlled open time	PCEs	Hydration retardation
			Sugar derivatives	Duration of open time
3	Rapid gain strength	Setting through hydration reactions	Portlandite	Inhibition of retarders action by either sucrose or PCEs uptake
			Clays	
			Inorganic salts	Enhanced chemical reactions
			PCEs	Promoted formation of hydrates and development of new surfaces
			C-S-H seeds	
			Shotcrete accelerator	
	Curing	Concrete hardening	Saturated lightweight aggregates	Reduction of early water loss
			Expansive and shrinkage-reducing admixtures	Minimization of plastic shrinkage cracking

in Figure 8. Marchon, D., et al. (2018) deliberately numbered the pre-application grade as 0 to distinguish concrete that is subjected to a degree of high shear stress by pumping and extrusion from concrete at rest after the application, which exhibits an internal accumulation of structures starting with grade 1. In the case of an initial stress to the yield point required for good workability, such material directly depends on the type of superplasticizer, e.g., PCE, and its doses. Achieving high structural stability is not always an easy task, especially with a high degree of dispersion. In the case of additive production, this is very important, especially before the layers are laid, because the mixture applied should be sufficiently cohesive so that it does not spread unduly after application.

The development of the yield stress immediately after extrusion and the application is showed in stage 1 in the time period after mixing the water and the binder, where there are no special hydrating effects on the stress and ultimate strength.

The transition period during which the stress is static and increases over time is shown in stage 2. If the fresh concrete material is allowed to rest and harden, a certain initial strength is developed through a thixotropic increase. In (Marchon, D., at al. 2018), the initial strength is the fresh strength of the concrete, which is needed to maintain its own shape and the other layers before the final solidification. Although this initial strength is usually not sufficient to hold multiple layers on the structure, this force is necessary to overcome the time gap between the extrusion and coating process (stage 1) and the rapid increase in force (stage 3). According to Marchon, D., 2018, stage 2 in practice also represents an open time during which concrete can still be easily laid and shaped; at the same time the mixture shows constant dynamic slip limits.

The sudden increase in the slip limit shown in phase 3 is a crucial point for the construction of 3D printing structures. After this point, it is known that the material is prone to keeping more layers due to the rapid increase in strength; at the same time the casting should be controlled quickly or at least precisely to prevent the formation of surface defects and deep cracks. Therefore, it is necessary to further investigate the properties of specific material composition systems in this time frame (Sung-Gul, H., et. al. 2018). While the initial flowability of a material can be changed in a simple way by adding various additives and admixtures, the subsequent development of solidification over time is considered a greater challenge for such 3D printing technology as the ultimate strength begins to increase and the material control becomes problematic.

8 CONCLUSION

Based on the study and analysis, it can be stated that chemical additives are necessary to produce concrete materials for 3D printing technology for which initial fluidity, the preservation of workability, and layer deposit ability are important, and which are among the main essential requirements for structural strength. These requirements are mainly based on the elimination of the use of formwork. Preparing compatible material for a large format 3D printer is therefore not an easy task. There are several factors that affect the properties of fresh and hardened composites. The individual compositions and dosages of the materials are tested daily, and their functionality and effect on the correct properties of the structure are examined by laboratory testing.

In the article, we have outlined some chemical and physical solutions offered by common admixtures to cope with the rapid growth of yield stress resulting from the effect of hydration and rheology and thus directly affecting the setting rate of cement composites. Therefore, the appropriate composition of materials and the management of the processing strategy are the most important aspects in the control of all material properties leading to good structural strength for such digital 3D technology. The research shows us that in order to achieve favorable results affecting the setting speed, it is important to correctly set the onset of setting and further behavior of the mixture with respect to the construction of 3D cement composites. The results are directly affected by the correct composition of the mixture and the correct dosage of the individual additives.

Acknowledgments

This work was supported by VEGA Grant 1/0680/20.

REFERENCES

ASB. (2009) *Spomaľovacie a urýchľovacie prísady do betónov*. Available at: https://www.asb.sk/stavebnictvo/zaklady-a-hruba-stavba/cement-beton/spomalovacie-aurychlovacie-prisady-do-betonov

CreaBeton Materiaux. (2019) *3D printing: printed concrete on jobsites.* Available at: https://www.vicat.com/news/3d-printing-printed-concrete-jobsites

Digital manufacturing experts. (2020) *3D Printing in Construction: How it Works, Technology and 3D Printers.* Available at: https://top3dshop.com/blog/3d-printing-in-construction

Jayathilaka, R. - Rajeev, P. - Sanjayan, J.G. (2020) *Yield stress criteria to assess the buildability of 3D concrete printing.* Available at: https://www.researchgate.net/publication/338423178_Yield_stress_criteria_to_assess_the_buildability_of_3D_concrete_printing

Jun, J. H. - Wan Byung, J. - Woohyun, Ch. - Jung-Hoon, K. (2020) *Development of a 3D Printer for Concrete Structures: Laboratory Testing of Cementitious Materials*. Available at: https://ijcsm.springeropen.com/articles/10.1186/s40069-019-0388-2

Kauppila, I. (2021) *How to 3D Print a House With Concrete.* Available at: https://all3dp.com/1/how-to-3d-print-a-house-with-concrete/

Luo, W. – Ma, X. - Yin, J. (2020): *Application and Research on Building 3D Printing*. Available at: http://www.jcreview.com/fulltext/197-1592494730.pdf

Marchon, D. - Kawashima, S. - Bessaies Bey, H. - Mantellato, S. (2018) *Hydration and rheology control of concrete for digital fabrication: Potential admixtures and cement chemistry*. Available at: https://www.researchgate.net/publication/325385160_Hydration_and_rheology_control_of_concrete_for_digital_fabrication_Potential_admixtures_and_cement_chemistry

Master civil engineer. (2021) *Mineral Admixtures – Its Types, Advantages and Their Effects on Concrete.* Available at: https://mastercivilengineer.com/mineral-admixtures-its-types-advantages-and-their-effects-on-concrete/

Murcia Heras, D. - Genedy, M. - Reda Taha, M.M. (2020) *Examining the signigicance of infill printing pattern on the anisotropy of 3D printed concrete.* Available at: https://www.sciencedirect.com/science/article/pii/S0950061820325642#f0015

Myrdal, R. (2007) *Accelerating admixtures for concrete.* Available at: https://www.researchgate.net/publication/288883755_Accelerating_admixtures_for_concrete

Ngo, T. - Kashani, A. - Imbalzano, G. - Nguyen, K. - Hui, D. (2018) *Additive manufacturing (3D printing): A review of materials, methods, applications and challenges*. Available at: https://doi.org/10.1016/j.compositesb.2018.02.012

Özalp, F. - Halit, Y.D. (2020) *Fresh and Hardening Properties of 3D High-Strength Printing Concrete and Its Recent Applications.* Available at: https://www.researchgate.net/publication/340069039_Fresh_and_Hardened_Properties_of_3D_High-Strength_Printing_Concrete_and_Its_Recent_Applications

Papachristoforou, M. - Mitsopoulos, V. - Stefanidou, M. (2018) *Evaluaton of workability parameters in 3D printing concrete.* Available at: https://www.sciencedirect.com/science/article/pii/S2452321618300714/pdf?md5=f61be7a68248eccb7ac3ef893ab89fb2&pid=1-s2.0-S2452321618300714-main.pdf

Sung-Gul, H. - Jiseul, P. - Nam-hee, K. (2018) *Structural Stability in Concrete 3D Printing Construction.* Available at: https://www.researchgate.net/publication/327577234_Structural_Stability_in_Concrete_3D_Printing_Construction

Van Der Putten, J. - Deprez, M. - Cnudde, V. - De Schutter, G. - Van Tittelboom, K. (2019) *Microstructural Characterization of 3D Printed Cementitious Materials.* Available at: https://www.mdpi.com/1996-1944/12/18/2993/pdf

Zhang, J. - Wang, J. – Dong, S. – Yu, X. - Han, B. (2019) *A review of current progress and application of 3D printed concrete*. Available at: https://www.sciencedirect.com/science/article/pii/S1359835X19302829

3D Printing Progress. (2017) *The first on-site house has been printed in Russia.* Available at: https://www.3dprintingprogress.com/articles/10683/the-first-on-site-house-has-been-printed-in-russia

sciendo

Slovak Journal of Civil Engineering

Vol. 30, 2022, No. 1, 57 – 66
DOI: 10.2478/sjce-2022-0007

A STUDY ON THE APPLICABILITY OF A SWAT MODEL IN PREDICTING THE WATER YIELD AND WATER BALANCE OF THE UPPER OUÉMÉ CATCHMENT IN THE REPUBLIC OF BENIN

Oluwatosin Onaopemipo OLOFINTOYE[1*], Ayanniyi Mufutau AYANSHOLA[1], Adebayo Wahab SALAMI[1], Akim IDRISSIOU[2], Juliana Omanya IJI[1], Oluwafemi Oyetunde ADELEKE[2]

Abstract

This study investigates the applicability of a Soil and Water Assessment Tool (SWAT) model in predictions of the water yields and water balance of the Upper Oueme catchment in the northern part of the Republic of Benin. Meteorological and hydrological data for a period of 20 years were collected from the Meteorological Agency of Benin and the National Directorate of Water respectively. Spatial data such as a Digital Elevation Model and land use and soil maps were also extracted from suitable databases. Geographic information system (GIS) software was applied in combination with SWAT to process the spatial data and simulate the streamflow record. A good correlation between the simulated and observed data during the calibration and validation was found, using statistical measures such as the Nash-Sutcliffe Efficiency (NSE>0.65%), the standard deviation ratio (RSR<0.6), percent bias (±10%≤PBIAS<±15%), and the coefficient of determination (R^2=0.78). An estimated potential water yield of 18,671.61mm in the catchment over the period of the simulation suggests that subsistence agriculture is sustainable in the area. The model is suitable for estimating the water yield and water balance in the catchment.

Address

[1] Dept. of Water Resources and Environmental Engineering, University of Ilorin, Ilorin, Nigeria

[2] Dept. of Civil Engineering, University of Ilorin, Ilorin, Nigeria

* ***Corresponding author:*** olofintoye.oo@unilorin.edu.ng; olofintoye.oo@gmail.com

Key words

- Catchment
- SWAT model.
- GIS,
- Water Yield,
- Water Balance.

1 INTRODUCTION

The problem of the scarcity and poor quality of water is prevalent in many developing nations of the world. This, in some cases, has been attributed to the overutilization and mismanagement of limited freshwater resources (Olofintoye et al., 2013; Ayanshola et al., 2016). To effectively resolve water mismanagement issues to ensure the sustainability of freshwater at both the watershed and basin levels, reliable estimates of the water yield and balance is a prerequisite (Ayanshola et al., 2018). The water balance in a catchment is influenced by parameters such as the climate, land use, soil use, and physical properties defined by the morphology. Understanding the hydrological response of a watershed to variations in these parameters is necessary in assessing the water yield and availability within a catchment over a period of time (Tracy and Scott, 2013).

Agricultural activities and urbanization have been identified as major contributors to extensive changes in land and soil use. These changes often lead to the degradation of land, which, more often than not, is detrimental to the sustainability of the environment (Portnova and Safriel, 2004). For instance, the deforestation of virgin land for agricultural or urban uses may impact soil integrity, the assemblage of native species, and nutrient fluxes. This may affect the hydrological regime of the watershed by altering the rates of interception, infiltration, evapotranspiration and groundwater recharge, which often result in changes in the timing and amount of the river flow (Smakhtin, 2001). Contrary opinions (Chandler, 2006), however, suggest that afforestation, especially the establishment of plantations in subtropical regions, has resulted in increased transpiration over an area with a consequential reduction in the groundwater recharge and base flow rates. This can also affect the hydrological regime

of a watershed. Further studies (Chandler, 2006; Bonnell et al., 2010) suggest, however, that the removal of a vegetal cover may result in an increased base flow if the soil is left undisturbed or may result in a reduction in base flow if the deforestation is followed by land use practices such as urbanization, which can compact the soil. Hence, extensive changes in land use as a result of agricultural activities or urbanization necessitate an investigation of the water balance and yield of a watershed.

An extended period of drought experienced in the northern parts of the Republic of Benin in the 1970s resulted in the degradation and depletion of croplands in the region. A massive migration of farmers from the region led them to resettle in the less-populated southern areas of the upper Oueme catchment (GLOWA-IMPETUS, 2005). These migrant farmers occupied croplands in what is now referred to as "cropland colonization" in that area. Massive changes in land use occurred as a result of the removal of vegetation cover when the farmers searched for new farmlands and urban areas to develop and resettle in. Lawin et al., (2019) reports a substantial conversion of the woodlands, gallery forests, forests and savannas into agricultural land in the area between 1975 and 2013. Agriculture occupied 7.1% of the catchment area in 1975 but 31.4% in 2013. These changes have resulted in increased direct runoff and erosion. Furthermore, the pressure on natural and freshwater resources in the region has been further exacerbated by a high demographic growth rate of about 3% per annum and, in recent times, the impact of climate change. Thus, it is pertinent to investigate the water balance and yield in the region to reduce the vulnerability and ensure the sustainability of its freshwater resources. This aim aligns with the sustainable development goal (SDG) No. 6 of the United Nations (UN, 2021).

According to Stehr et al. (2008), the study of water resources at the river catchment level has been widely adopted as a better alternative for managing and assessing freshwater resources. Various hydrological models that incorporate an understanding of hydrological components and their spatial and temporal variability have been applied for the efficient planning and management of water resources. In particular, researchers have adopted simulation software in modeling hydrological processes in the region of the study area. For instance, Lawin et al., (2019) investigated the impacts of climate change on the Ouémé River discharge at the Bonou outlet (1971 to 2050) using four global climate models (GCM). The Hydrological Modeling System from the Hydrological Engineering Center (HEC-HMS), which is a semi-distributed model, was used to simulate the runoff. The model showed an ability to simulate runoff while taking into account changes in the land use and cover. An increasing trend in discharges was forecasted over the study period. Biao (2019), applied a lumped conceptual hydrological model based on the least action principle (HyMoLAP), which was designed to minimize uncertainties in rainfall-runoff process modeling, to assess the impacts of climate change on river discharge dynamics in the Bétérou and Bonou sub-catchments in the Oueme River basin. The model's uncertainty projections indicated that the entire discharge distribution had shifted towards extreme events. HyMoLAP was found suitable for modelling river discharges in the basin. The water balance of the interactions between the soil, biosphere, and atmosphere over the upper Ouémé River basin was evaluated by Getirana et al. (2014) using a Land Surface Model (LSM). It was determined that a LSM is not appropriate for estimating river discharges in that region. Further studies based on field measurements were recommended to improve the performance of the model. A study on the application of the LISFLOOD hydrological model in estimating future discharges in the Ouémé river basin at the Bétérou outlet is reported in Emmanuel et al., (2018), while the application of a time-dependent generalized extreme value (GEV) model in estimating the annual maximum discharge at five gauging stations in the Ouémé River Basin may be found in Hounkpe et al., (2015).

The Soil and Water Assessment Tool (SWAT) developed by Texas Agricultural and Mechanical University (TAMUSWAT, 2021) is a physically-based model, which employs a water balance equation for the simulation of the hydrological processes within a watershed. A major example of the applications of SWAT took place within a hydrological unit model that was used to support the United States Department of Agriculture (USDA) analyses of the Resources Conservation Act Assessment of 1997. This system was employed to simulate the hydrology and losses from pollutants within each of the 2,149 United States Geological Survey (USGS) 8-digit Hydrological Cataloging Units (Arnold *et. al.,* 1999; Gassman *et. al*., 2007). Olusanya et al. (2021) investigated the applicability of SWAT in the Oueme River Basin using remotely sensed data due to the unavailability of observed data. The model satisfactorily simulated the streamflow; however, the effectiveness of the satellite data remains unclear in some areas. Other applications of SWAT have also been reported in the literature (Stehr et al. 2008; Tracy and Scott, 2013; Ayanshola et al., 2018).

This study further investigates the applicability of SWAT in the upper Oueme catchment. The aim of the research is to calibrate a SWAT model using a manual optimization method (Moriasi et al., 2007) and to use the calibrated model to estimate the water yield and water balance of the catchment. The remaining part of the paper is sectioned as follows: Section 2 presents a brief description of the study area; section 3 describes the methodology adopted in the study; while section 4 presents the results and discussion. The conclusion is presented in section 5.

2 DESCRIPTION OF THE STUDY AREA

The River Oueme, which is also called the Weme river, is the largest river in the Republic of Benin, West Africa. The river, which is about 510 kilometers long, is sourced in the Atakora Mountains at an elevation of about 465 meters above sea level and flows through several agro-ecological zones to discharge into the Atlantic Ocean at the Gulf of Guinea in Coutonou at an average rate of 170 cubic meters per second. The catchment of the river is situated between latitudes 6°30'N and 10°00'N and longitudes 0°52'E and 3°05'E. Its largest tributaries are the Okpara River on the left flank and the Zou River on the right. The Oueme River catchment represents the largest river basin in the country, with an area of about 46,990 square kilometers. The Oueme River Basin is composed of two main sub-basins, i.e., the Upper Oueme Catchment in the Dahomeyen Pedi plain and the Lower Oueme Catchment situated on the coastal sediments. The region is in the tropical savanna climate zone according to the Koppen climate classification. The annual average rainfall ranges from 900 mm to 1,200 mm, while the average annual temperature ranged between 25°C to 30°C within the period from 1998 to 2017. The largest portion of the basin area, i.e., about 89%, is located in Benin; 10% is situated in the western part of Nigeria, while 1% lies on the eastern fringe of Togo (Bossa, 2012).

The upper Oueme River basin is a sub-basin in the Oueme River catchment. It has a drainage area of 14,400 square kilometers. The sub-basin is located in the Sudan climate zone and is characterized by a single rainy season with an average rainfall of 1150 mm/year. The bulk of the rainfall occurs during the monsoon period between April and October. The average runoff is about 150 mm/year (Getirana et al., 2014). The geomorphology of the catchment is characterized by a flat, undulating pediplain relief with altitudes from 227 to 616 meters above sea level. The geology of the study area is mainly characterized by a Precambrian basement, which predominantly consists of complex granulites and gneisses. The dominant soil type is Luvisols and reflects stable geological conditions. The texture of the various soil types encountered is mainly composed of loam, clay, clay-loam, sandy-loam and sandy-clay-loam (Lawin et al., 2019). The land cover in the watershed is 80.7 % forest, 18.9 % croplands, and 0.3 % urban. The major crops grown in the catchment are corn, cassava, yams, and sorghum (Olusanya et al., 2021). Fig. 1 shows the study area.

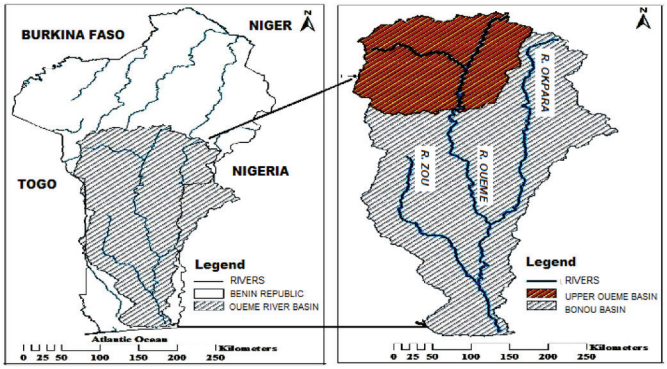

Fig. 1 *Location of the Oueme River catchment area. (Adapted:* www.mapwindow.com)

3 MATERIALS AND METHOD

3.1 Methodological framework

A hybrid framework was adopted in this study. Adeyemo and Olofintoye (2012) reported the success of several applications of hybrid models in resolving water management problems. The authors also noted that the development of hybrid systems, which blend existing models into a coherent solution framework that provides useful tools to aid in critical water management decisions, has been found propitious. Therefore, the application of hybrid models in the solution of water resources problems is encouraged (Olofintoye et al., 2016).

The hybrid framework applied in this study involves the combination of a Geographic Information System (GIS) software and SWAT. The GIS interface used was Map-window. This interface was chosen based on its ease of use and reported capability to effectively simulate the hydrology of a catchment with a high degree of accuracy when used in combination with a suitable plug-in (Tetsoane, 2013). Documentation on the software may be found at MapWin (2021). A plug-in that facilitates the incorporation of SWAT in the Map-window software environment is Map-window SWAT (MWSWAT). Documentation on the plug-in is available at TAMUSWAT (2021). In the workflow of the study, MWSWAT takes spatial data sets as the input and processes them in conjunction with the Map-window preprocessor to delineate the watershed and demarcate the Hydrological Response Units (HRUs) within the watershed. The HRUs and weather data are further processed by the SWAT engine to simulate the streamflow. During the calibration and validation, the simulated streamflow is compared with the observed streamflow, and the model parameters are adjusted until an acceptable calibration is achieved. The calibrated model is then used to estimate the water balance and yield of the catchment. This workflow is depicted in Fig. 2.

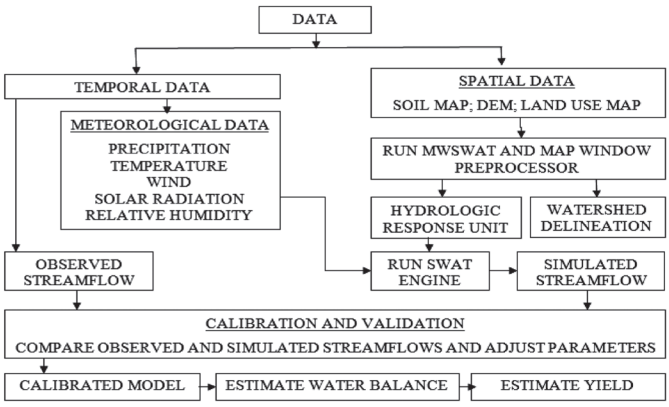

Fig. 2 *Methodological workflow diagram of the modeling process*

3.2 Data collection

The types of data required for the study are spatial and temporal data. The spatial data are topographical, i.e., a Digital Elevation Model (DEM) and soil and land use maps. These were employed to delineate the catchment area, demarcate the HRUs, and show the type of soil and land use/cover respectively. The watershed area is 14,236.73km^2 at a mean elevation of 355.09m with a slope of 0.99. The temporal data used are meteorological and streamflow data. The meteorological data include the daily precipitation, temperature, solar radiation, wind speed, and relative humidity. These were used in conjunction with the HRUs as an input to the SWAT engine to determine the hydrological response (simulated streamflow) of the catchment. Where there are gaps in the dataset, a weather generator embedded in SWAT (developed by Schuol and Abbaspour, 2007) was used to estimate the missing data. The streamflow data was acquired for the calibration and validation of the model.

The spatial data maps of the study area are presented in Fig. 3. Fig. 3a presents a 90 x 90 m resolution topographical data extracted from the Shuttle Radar Topography Mission (SRTM) website (http://srtm.csi.cgiar.org/). The site archives digital elevation data for major parts of the world. These archives have been preprocessed to fill data voids and to facilitate its ease of use by a wide range of potential users. This was done in an effort to encourage the applications of geospatial science methods for sustainable development and resource conservation in the developing world. The DEM provides the basis for watershed delineation into sub-basins. Also, topographic parameters such as the terrain slope, channel slope, and reach length are evaluated using the DEM. The land use maps (Figs. 3b and 3c) for the area were extracted from the Global Land Cover Characterization (GLCC) database (http://edcsns17.cr.usgs.gov/glcc/glcc.html). This database is maintained by the United States Geological

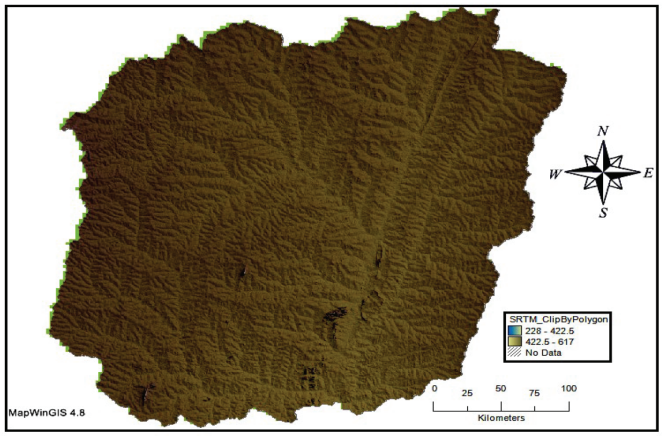

(a) *Digital elevation model (DEM)*

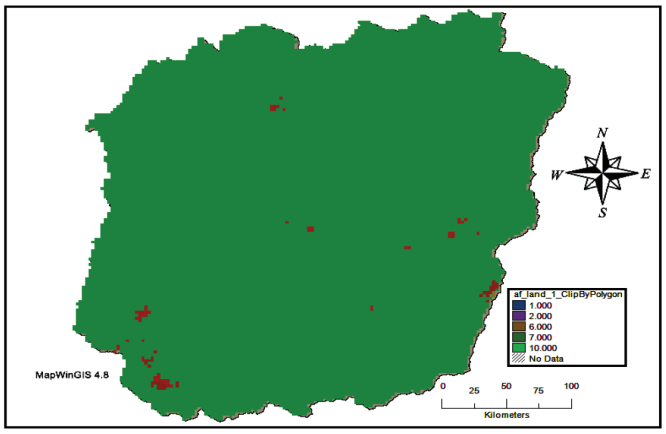

(b) *Land use map*

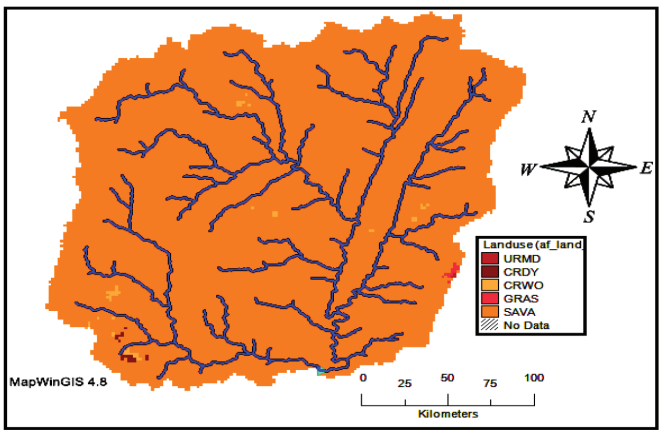

(c) *Land use showing stream reach*

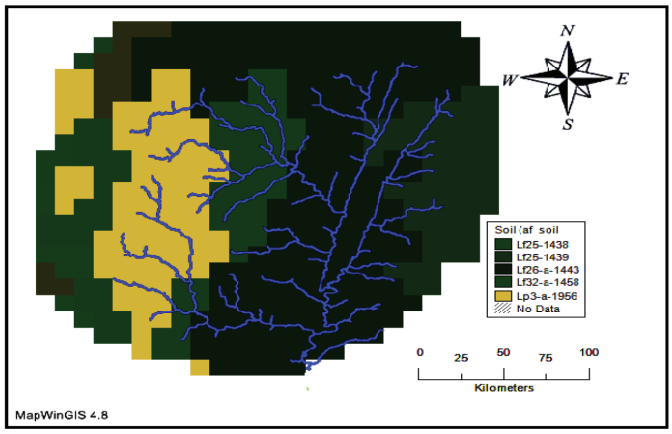

(d) *soil type*

Fig. 3 *Spatial data maps of the Upper Ouémé River Catchment.*

Tab. 1 *The land use distribution in the study area*

S/N	SWAT Code	Description	Area(ha)	%Watershed
1	SAVA	Savannah	894687.98	60.5
2	CRWO	Cropland/Woodland	492448.10	33.3
3	GRAS	Grass Land	26618.81	1.8
4	URMD	Urban and Built-Up Land	14788.23	1.0
5	CRDY	Dry Land, Cropland, and Pasture	50279.98	3.4

Tab. 2 *The soil type distribution in the study area*

S/N	SWAT Code	Description	Area(ha)	%Watershed
1	Lf26-a-1443	Sandy-Clay-Loam	743897.0	49.69
2	Lf25-1438	Sandy-Clay-Loam	237453.8	15.86
3	Lp3-a-1956	Sandy-Clay-Loam	336304.1	22.46
4	Lf25-1439	Sandy-Clay-Loam	156459.4	10.45
5	Lf32-a-1458	Sandy-Clay-Loam	208.77	0.01

Survey. The GLCC has a spatial resolution of 1 Km and 24 classes of land use representations, which provided the basis for estimating the vegetation cover in the watershed. Tab. 1 shows the land use distribution in detail. The soil map for the study area (Fig. 3d) was obtained from the Harmonized Digital Soil Map of the World (HWSD). These maps were produced by the Food and Agriculture Organization of the United Nations and were completed in January 2003. The database provides data for 16,000 different soil mapping units containing two layers (depths of 0 - 30 cm and 30 - 100 cm). Tab. 2 shows the soil distribution in the study area.

The meteorological data were obtained from the Benin Meteo Agency for the Parakou weather station, which is located at 2.60° N, 9.35°E. The monthly streamflow data from the stream gauging station located at Bétérou for the years 2003–2009 was collected from the National Directorate of Water (DG-Eau) of Benin. This was used for the calibration of the model. Tab. 3 presents the data used in this study, while Tab. 4 presents the monthly averages of the variables at the Parakou weather station.

Tab. 3 *Model input for the upper Ouémé river catchment area.*

S/N	Data type	Description	Resolution	Source
1	Topography	Digital Elevation Model	90×90 m	Radar Topographical Mission Shuttle
2	Land Use Map	Land Use Classification	1 km	Global Land Cover Classification, Satellite Raster
3	Soil Map	Soil Type and Texture	10 km	Digital Soil Map of the World
4	Weather	Daily Precipitation, Temperature, Relative Humidity, Wind Speed, Solar Radiation	Daily	Benin Meteo Agency
5	Streamflow	Monthly stream flow	Monthly	National Directorate of Water

Tab. 4 *Monthly averages of the variables at the Parakou weather station (1998 – 2017)*

Variable	J	F	M	A	M	J	J	A	S	O	N	D
Precipitation (mm)	3.3	9.5	34.2	77.5	134.1	168.1	176.4	206.5	216.2	107.3	8.7	2.1
Solar Rad/day (h)	8.1	8.2	7.5	7.7	7.3	6.4	4.8	3.8	5	6.8	8.3	8.5
T max (°C)	38.2	39.4	39.9	39.3	36.9	34.3	32.9	32.2	33.0	34.7	36.6	37.0
T min (°C)	17.1	19.4	21.2	20.8	20.3	19.6	19.9	19.8	19.5	20	19.1	17.0
RH max (%)	89.8	90.1	90.1	95.3	96.6	97.2	97.4	97.7	98.0	97.4	96.7	92.0
RH min (%)	8.2	7.9	11.4	23.2	37.0	46.6	51.8	55.3	52.4	35.4	14.4	9.8
Wind sp (m/s)	2.2	2.1	2.3	2.5	2.3	2.1	2.0	1.9	1.7	1.8	1.9	2.2

3.3 Configuration of the model for the hydrological simulation

SWAT is a semi physically-based model, which can model a number of sub-basins based on a given digital elevation model map instead of using regression equations to describe the input-output relationship. The model simulates surface and subsurface processes by accounting for vadose processes. Runoff volume is calculated using the Curve Number (CN) Method, and the sediment yield is calculated using a modified universal soil loss equation. The routing is done using the variable storage method or the Muskingum method. Extensive details of the model may be found in the literature (Neitsch et al., 2011; Arnold et al., 2012; TAMUSWAT, 2021). Fig 4 gives an overview of the SWAT model.

Configuring the model for a hydrological simulation involves adjusting the relevant settings in the software's interface. The settings to be adjusted may include the period of simulation, the location of the spatial and weather database files, and the methods of computing hydrological variables (which may be optimized). In this study, the simulation period was from January 1, 1998, to December 31, 2017 (20 years). A total of 147 sub-basins were created and further divided into 174 HRUs.

3.4 Calibration and validation of the model

SWAT provides different methods for estimating hydrological variables. For example, the Priestley, Penman-Monteith or

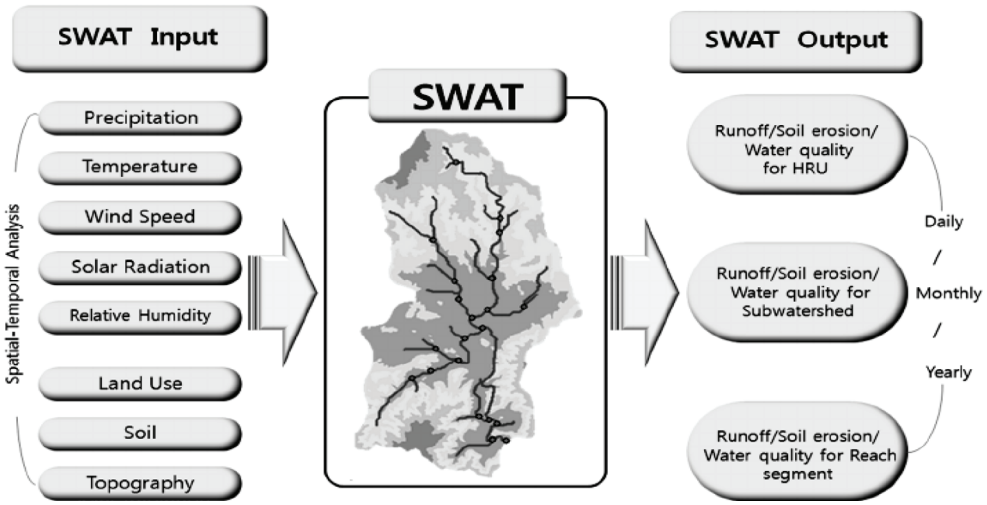

Fig. 4 *Overview of the SWAT model (Heo et al., 2008)*

Tab. 5 *Performance ratings for the recommended statistics for calibrating the monthly time step (Moriasi et al., 2007)*

Performance Rating	PBIAS (%)	RSR	NSE
Very good	PBIAS < ±10	0.00≤RSR≤0.50	0.75 < NSE≤1.00
Good	±10≤PBIAS < ±15	0.50≤RSR≤0.60	0.65 < NSE≤0.75
Satisfactory	±15≤PBIAS < ±25	0.60≤RSR≤0.70	0.50 < NSE≤0.65
Unsatisfactory	PBIAS≥±25	RSR > 0.70	NSE≤0.50

Tab. 6 *Optimization of the model parameters*

SWAT Code (Parameter)	Description	Method	SWAT-Value	Decision Variable range
IPET	Potential Evapotranspiration	Priestley Penman/Monteith Hargreaves	0 1 2	0 - 2
IEVENT	Run off	Curve Number Green/Ampt	0 1	0 - 1
IRTE	Routing	Variable Muskingum	0 1	0 - 1

Hargreaves methods are available for estimating potential evapotranspiration; the Curve Number or Green and Ampt methods are available for estimating surface runoff; while the Variable or Muskingum methods are available for channel water routing. These were used as parameters in calibrating the model. The Actual Evaporation is computed as a function of the Potential Evaporation by the SWAT model internally.

Manually calibrating a physically-based process model involves iteratively adjusting the parameters of the model until the discrepancy between the model output (simulated data) and the observed (measured) data is at a minimum, or until a test statistic, which is evaluated based on this discrepancy, falls within an acceptable range (Moriasi et al., 2007). However, caution must be exercised to ensure that the range of values employed for the parameters during calibration is plausible. This is necessary to ensure the applicability of the calibrated model afterwards when assessing the impacts of changing scenarios in the management options (Stehr et al., 2008). Moriasi et al. (2007) suggests the use of three statistics in evaluating the model's performance; i.e., the standard deviation ratio (RSR), the Nash–Sutcliffe efficiency (NSE), and the percent bias (PBIAS). These may be employed as objective functions in optimizing the model. These statistics and the coefficient of determination (R^2) were employed to evaluate the model's performance in this study. The rating for the performance of the model, which was calibrated on a monthly time-step and based on these statistics, is presented in Tab. 5.

Since the aim of this study is to demonstrate the applicability of SWAT in the basin, a manual calibration approach (Moriasi et al., 2007) was adopted. A constraint satisfaction combinatorial optimization problem, in which the parameters for computing the variables are adjusted until the NSE and PBIAS falls within a very good or good range, was adopted. The optimization model parameters are given in Tab. 6.

The SWAT model was calibrated for the upper Oueme river watershed using the observed streamflow at the Beterou gauging station. Streamflow data from January, 2003, to December, 2005, was used as the calibration set, while data from January, 2006, to December, 2009, was used as the validation set. The simulation in SWAT was based on a daily time-step; therefore, the simulated daily streamflows were aggregated to monthly flows to enforce the calibration in the monthly time-step.

4 RESULTS AND DISCUSSION

4.1 SWAT parameters settings

The settings determined from the calibration are as follows: the Run-off Curve Number (CN) method was employed to estimate the surface runoff from precipitation (IEVENT=0); the Penman-Monteith method was selected for estimating the potential evapotranspiration (IPET=1), while the variable storage method was chosen to simulate the channel water routing (IRTE=0).

4.2 Evaluation of the model's performance

The computed values of the test statistics used for the model's evaluation are presented in Tab. 7 for both the calibration and validation datasets. Fig. 5 presents a pictorial view of how well the simulated data fits the observed data during the calibration and validation.

An inspection of Fig. 5 shows a good fit between the simulated and observed streamflow data. Also, the NSE values are greater than 0.65; the values of RSR are greater than or equal to 0.5; while the PBIAS values lie in the range ±10%≤PBIAS<±15%, for both the calibration and validation periods. This indicates the good performance of the model (See row 2 of Tab. 5).

The fit here is not as close as that reported by Emmanuel et. al., (2018) using the LISFLOD model (NSE=0.92 for calibration

Tab. 7 *Values of the performance statistics for the calibration and validation data sets.*

Test Statistics	Data Set Calibration	Validation
NSE	0.66	0.75
RSR	0.58	0.50
PBIAS	-14.00%	-11.90%
R^2	0.78	0.78

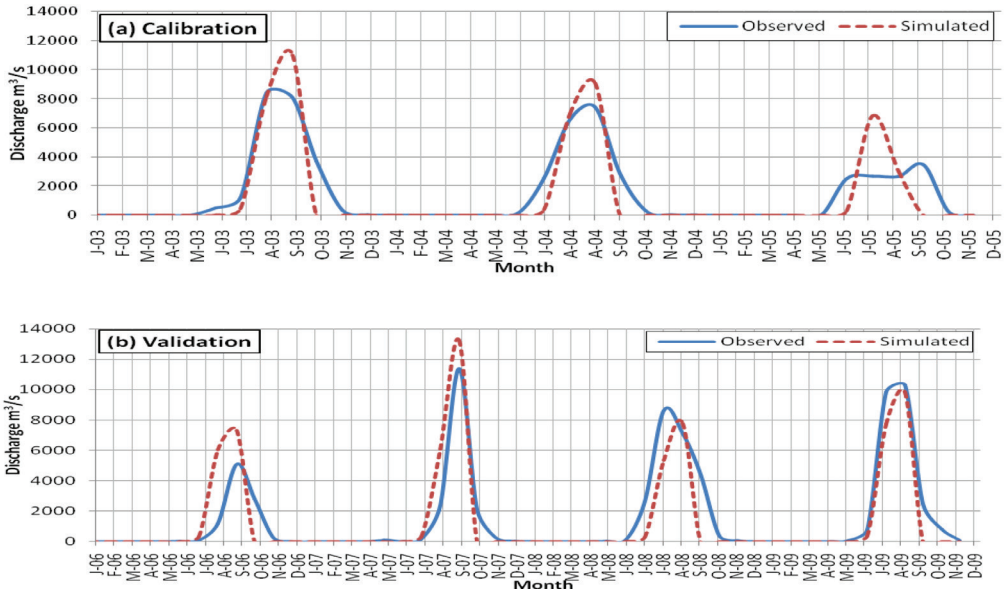

Fig. 5 *Fit of observed and simulated monthly streamflow for the (a) calibration and (b) validation periods.*

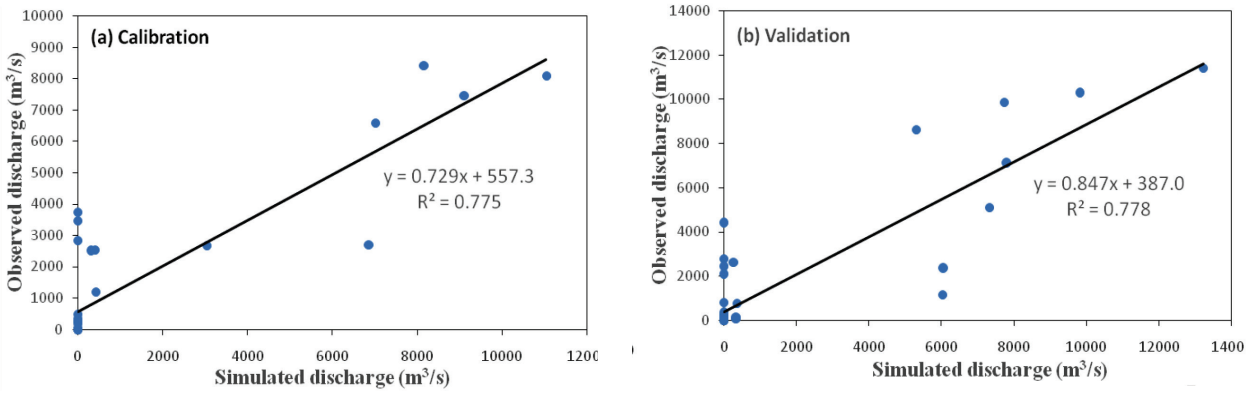

Fig. 6 *Correlation between the observed and simulated monthly discharge for the (a) calibration and (b) validation periods.*

and NSE=0.95 for validation). This may be due to differences in the periods employed for the model's calibration and the differences in the types and number of model parameters and other possible random variables. Since both studies employed the manual calibration approach, the performance of one model over the other may not be established until rigorous statistical tests are performed. This is beyond the scope of this study. However, the better performance during validation than during calibration that was observed in the study is also the case in the present study.

A study by Getirana et al. (2014) in the study area also produced NSE=0.9 for both the calibration and validation. However, the ISBA model employed was optimized using a multi-objective complex evolution global optimization algorithm. The values of NSE in this study suggest a closer fit than the study by Olusanya et. al. (2001), who calibrated a SWAT model using remotely sensed data in the region and obtained NSE=0.55 during calibration and NSE=0.51 during validation. The results however were satisfactory.

Negative values of the PBIAS may be obtained in cases where a model overestimates the observed data. However, the errors in the estimates in this study are negligible as the value of the statistics lies in the range of a good fit (Tab. 5). Furthermore, the regression analyses of the observed versus the simulated data (Fig. 6) for the calibration and validation periods show good relationships between the dataset as indicated by the R^2 values of approximately 0.78 in both cases.

The manual approach adopted in this study may constitute a serious limitation. Overall, the model developed in this study compares well with models that have been applied in the area. The aim of this study is to demonstrate the applicability of the model in the area and not involve a rigorous comparison of the model's performance. Since the performance of the calibrated model falls in a good range, the model is therefore adopted for the remaining part of this study.

4.3 Application of the results

Following the successful calibration and validation of SWAT, the model was applied to estimate the water balance components of the river basin and subsequently the water yield.

4.3.1 Estimation of the water balance

The estimation of the Upper Oueme River catchment water balance components was done on an annual basis for 20 years

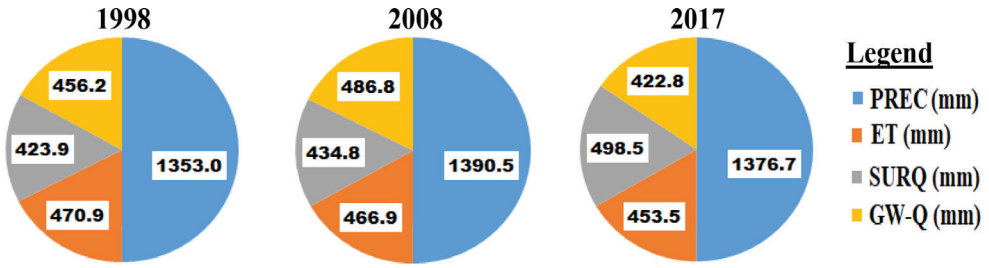

Fig. 7 *Pie charts showing the water balance in (a) 1998, (b) 2008 and (c) 2017*

(1998 to 2017). The main components of the water balance in the river basin are: the total amount of precipitation (PREC) in the basin in a year, the actual evapotranspiration (ET) from the basin, and the net amount of water that appears as streamflow out of the basin (the water yield). The SWAT simulation outputs (measured in mm) are: (ET), surface runoff (SURQ), groundwater flow (GW-Q) and lateral flow (LAT-Q). Pie charts showing the water balance for the years 1998 (the beginning of the simulation period), 2008 (a year around the middle of the simulation period), and 2017 (the end of the simulation period) are presented in Fig. 7 a–c respectively.

It was observed that the lateral flow contributions to the river flow were negligible in all the cases and is therefore not a component in the pie charts. Lateral flows are usually high where an impervious layer is close to the surface and the slope of the area is high (Reddy, 2014). The contrary, however, exists in the study area. The loose nature of the soil (see Tab. 2) combined with the gentle slope of the area (less than 3%) reduces the potential for lateral flows. Also, farming activities in the area have further loosened the top soil.

In 1998, approximately 35% of the precipitation within the basin was lost through ET, while about 31% and 34% were converted into surface runoff and base flow respectively. Around 34%, 31% and 35% of the rainfall, respectively, appeared as ET, SUR-Q, and GW-Q in 2008, while about 33%, 36% and 31% of the precipitation, respectively, appeared as ET, SUR-Q and GW-Q in 2017.

In order to facilitate a comparison of the water balance obtained in this study with an earlier study in the basin (Getirana et al., 2014), the water balance over a period of 4 years (2005–2008) was estimated. In this study, approximately 41% of the precipitation within the basin is lost through ET, while about 27% and 32% are converted into surface runoff and the base flow respectively. The values here are different from those obtained in the earlier study, which reported 72%, 5% and 23% respectively for ET, SUR-Q and GW-Q. It should be noted, however, that the water balance in the earlier study was estimated over 5 stations, while the water balance in this study employs a single station. Moreover, the authors reported that the LSM method employed in estimating the water balance in the study is not an appropriate approximation for the river discharges in the tropical region. Therefore, the calibrated SWAT model in this study is adopted for further evaluations. However, the high rate of evapotranspiration observed in the earlier study is also noted herein. This high rate of ET in the basin may be attributed to the significant vegetal cover (see Tab. 1), the high temperatures and the high volumes of water available at the root zone due to high percolation as indicated by the large volume of the groundwater flow. While the potential surface runoff in the Upper Oueme River watershed may not be particularly high, the high volume of sub-surface water (about 34%) suggests that the development of sub-surface water is a viable alternative source of water resources for the inhabitants of the study area.

4.3.2 Estimation of the water yield

The water yield potential of a basin is one of the important parameters that need to be estimated for efficient water management. Knowledge of this data may assist managers in planning and predicting the possibilities of water shortages in the future. In SWAT modeling, the water yield may be considered as the total amount of water leaving the HRUs and entering the main stream channel during the time step (Adeogun et al., 2014).

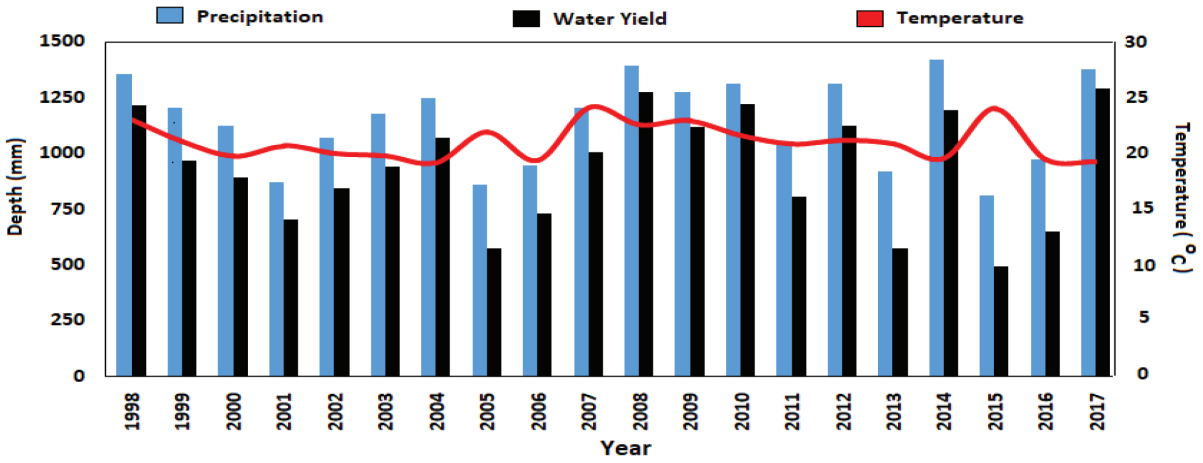

Fig. 8 *Plot of the Annual Water Yield from 1998 – 2017*

The contributions of each sub-basin in the watershed to the water yield during the period of the simulation were examined using the calibrated SWAT model. A cumulative amount of 18,671.61 mm of water was estimated as the potential water yield of the basin over the period of the simulation (1998–2017). This suggests that subsistence agriculture is sustainable in the area.

The distribution of the annual water yield in the basin was also investigated. A plot showing variations in the water yield over the simulation period is presented in Fig. 8. It was observed that the maximum yield (1,289.1 mm) occurred in 2017, while the minimum (492.7 mm) occurred in 2015. It may be inferred that 2015 was a dry year with a low precipitation record in the catchment.

5 CONCLUSION

This study investigated the applicability of SWAT in estimating the water balance and yield by simulating the hydrological processes and responses within a river basin. The model was calibrated and validated using the monthly streamflow data from the Beterou River gauging station and subsequently employed to estimate the water balance and yield of the Upper Oueme River Basin. A close fit between the simulated and observed streamflow data during the calibration and validation suggests a good model performance. This was further established by the values of the standard test statistics (NSE>0.65, RSR$\leq$0.5, $\pm$10%$\leq$PBIAS<$\pm$15% and R^2>0.75) lying within good acceptable ranges. Overall, the model was able to predict the water balance and yield in the study area satisfactorily. The results showed that once the SWAT hydrological model is effectively calibrated, it can be a useful tool for accurate hydrological predictions to aid in management decisions.

The surface runoff potential of the catchment was moderate; however, substantial sub-surface water components suggest that sub-surface water development is viable as an alternative potential water resource for the basin. Although the surface runoff is moderate, Emmanuel et at., (2018) has noted that the Oueme River at the Beterou outlet will experience increased discharges for all the time horizons until 2050 and for all the combined climate and land use change scenarios. This information on the future of water resources in the basin is an invitation to water resource managers to plan for design and mitigation strategies to cope with the negative effects of increased discharges.

REFERENCES

Adeogun, A.G. - Sule, B.F. - Salami, A.W. - Okeola, O.G. (2014) *Validation of SWAT Model for Prediction of Water Yield and Water Balance: Case of Upstream Catchment of Jebba Dam in Nigeria*. International Journal of Mathematical, Computational, Physical and Quantum Engineering, Vol. 8, No. 2, pp. 264-270.

Adeyemo, J. - Olofintoye, O. (2012) *Application of hybrid models in water resources management*. Proceedings of EVOLVE International Conference 2012. Mexico City, Mexico, Schuetze, O., Tantar, A., Tantar, E., Bouvry, P., Moral, P. D. and Legrand, P. (eds.) 1-13. Published by CINVESTAV-IPN, Mexico.

Arnold, J. G., and Allen, P. M. (1999). Automated methods for estimating base-flow and ground water recharge from streamflow records, *JAWRA Journal of the American Water Resources Association. 35 (2), 411–424.*

Arnold, J.G. – Kiniry, J.R. – Srinivasan, R. - Williams, J.R. – Haney, E.B. - Neitsch, S.L. (2012)) *Soil and Water Assessment Tool Input/Output Documentation Version (2012)*. Texas Water Resources Institute, USA.

Ayanshola, A.M. - Jacob, S.O. - Bilewu, S.O. - Salami, A.W. - Mokuolu, O.A. (2016) *Prioritization of Adaptation Strategies for Water Supply and Demand under Climate Change and Its Variability in Abuja, Nigeria*. Journal of Research in Forestry, Wildlife and Environment. Vol. 8, No. 3, pp. 1–10.

Ayanshola, A. - Olofintoye, O. - Obadofin, E. (2018) *Impact of Global Warming on Precipitation Pattern in Ilorin and Hydrological Balance of Awun Basin*. Slovak Journal of Civil Engineering - SJCE, Vol. 26, No. 1, pp. 40-46.

Biao, E. I. (2017) *Assessing the Impacts of Climate Change on River Discharge Dynamics in Oueme River Basin (Benin,West Africa).* Hydrology, Vol. 4, No. 4, 47. DOI: 10.3390/hydrology4040047.

Bonnell, M. - Purandara, B.K. - Venkatesh, B. - Krishnaswamy, J. – Acharya, H.A.K. - Sungh, U.V. - Jayakumar, R. - Chappell, N. (2010) *The impact of forest use and reforestation on soil hydraulic conductivity in Western Ghats of India: implications for surface and sub-surface hydrology*. J. Hydrol. Vol. 391, pp. 47–62.

Bossa, Y.A. (2012) *Multi-scale modeling of sediment and nutrient flow dynamics in the Ouémé catchment (Benin), towards an assessment of global change effects on soil degradation and water quality*. Thesis (PhD), University of Bonn, Germany. 130 pp.

Chandler, D.G. (2006) *Reversibility of forest conversion impacts on water budgets in tropical karst terrain*. For. Ecol. Manage. Vol. 224, pp. 95–103.

Emmanuel, L.A. – Yèkambèssoun, N.M. - Biaou, C.A. – Komi, K. – Hounguè, R. – Yao, K.B. – Afouda, A.A. (2018) *Mid-Century Daily Discharge Scenarios Based on Climate and Land Use Change in Ouémé River Basin at Bétérou Outlet.* Hydrology, Vol. 5, No. 4, 69. DOI: 10.3390/hydrology5040069**.**

Gan, T. Y. - Dlamini, E. M. - Biftu G. F. (1997) *Effects of model complexity and structure, data quality, and objective functions on hydrologic modeling*. J. Hydrol. Vol. 192, No. 1, pp. 81-103.

Gassman, P. W., Reyes, M. R., Green, C. H. and J. G. Arnold, (2007). The soil and water assessment tool: historical development, applications and future research directions. American Society of Agricultural and Biological Engineers. *Invited Review Series. ISSN 0001-2351. Vol. 50(4), 1211-1250*

Getirana, A.C.V. - Boone, A. – Peugeot, C. (2014) *Evaluating LSM-Based Water Budgets over a West African Basin Assisted with a River Routing Scheme.* AMS Journal of Hydrometeorology, Vol. 15, No. 6, pp. 2331–2346. DOI: 10.1175/JHM-D-14-0012.1.

Glowa-Impetus, (2005) *Global Change and the Hydrological Cycle*. GLOWA Bonn, Berlin, BMBF: pp. 43.

Heo,S. – Kim, N. – Park, Y. – Kim, J. – Kim, S. – Ahn, J. – Kim, K. – Lim, K.J. (2008) *Evaluation of Effects on SWAT Simulated Hydrology and Sediment Behaviors of SWAT Watershed Delineation using SWAT ArcView GIS Extension Patch.* Journal of Korean Society on Water Quality, Vol. 24, No. 2, pp.147-155 (2008)

Hounkpè, J. – Diekkrüger, B. – Badou, D.F. – Afouda, A.A. (2015) *Non-Stationary Flood Frequency Analysis in the Ouémé River Basin, Benin Republic.* Hydrology, Vol. 2, No. 4, pp. 210-229. DOI: 10.3390/hydrology2040210.

Lawin, A.E. – Hounguè, R. – Yèkambèssoun, N.M. – Hounguè, N. R. – Attogouinon, A. - Afouda, A.A. (2019) *Mid-Century Climate Change Impacts on Ouémé River Discharge at Bonou Outlet (Benin).* Hydrology, Vol. 6, No. 3, 72. DOI: 10.3390/hydrology6030072.

MapWin (2021). *About the MapWindow GIS Open Source Project*. Available at: https://www.mapwindow.org/, (accessed at 29/07/2021).

Moriasi, D.N. - Arnold, J.G. - Van Liew, M.W. - Bingner, R.L. - Harmel, R.D. - Veith, T.L. (2007) *Model evaluation guidelines for systematic quantification of accuracy in Watershed Simulations*. Trans. ASABE Vol. 2007, No. 50, pp. 885–900.

Neitsch, S.L. - Arnold, J.G. - Kiniry, J.R. - Williams, J.R. (2011) *Soil and Water Assessment Tool, Theoretical Documentation Version (2009)*. Texas Water Resources Institute.

Odusanya, A.E. – Schulz, K. – Biao, E.I. – Degan, B.A.S. - Mehdi-Schulz, B. (2021) *Evaluating the performance of streamflow simulated by an eco-hydrological model calibrated and validated with global land surface actual evapotranspiration from remote sensing at a catchment scale in West Africa.* Journal of Hydrology: Regional Studies, Vol. 37 (2021). DOI: 10.1016/j.ejrh.2021.100893.

Olofintoye, O. - Adeyemo, J. - Otieno, F. (2013) *Evolutionary algorithms and water resources optimization*. In EVOLVE - A Bridge between Probability, Set Oriented Numerics, and Evolutionary Computation II. : Published by Springer Berlin Heidelberg, 2013. 491-506 pp. ISBN 978-3-642-31518-3.

Olofintoye, O. - Otieno, F. - Adeyemo, J. (2016) *Real-time optimal water allocation for daily hydropower generation from the Vanderkloof dam, South Africa*. Applied Soft Computing, Vol. 47, No. 2016, pp. 119–129.

Portnova, B.A. - Safrielb U.N. (2004) *Combating desertification in the Negev: dryland agriculture vs. dryland urbanization*. Journal of Arid Environments Vol. 56, No. 2004, pp. 659–680.

Reddy P.J.R (2014) . *A Textbook of Hydrology*. University Science Press, India, 2014. 50 pp. ISBN 978-93-80856-04-9.

Schuol, J. - Abbaspour, K.C. (2007) *Using Monthly Weather Statistics to Generate Daily Data in a SWAT Model Application to West Africa*. Ecological Modelling, Vol. 201, pp. 301-311.

Smakhtin, V.U. (2001) *Low flow hydrology: a review*. J. Hydrol. Vol. 240, pp. 147–186.

Stehr A. - Debels, P. - Romero, F. - Alcayaga, H. (2008) *Hydrological modelling with SWAT under conditions of limited data availability: evaluation of results from a Chilean case study*. Hydrological Sciences– Journal–des Sciences Hydrologiques, Vol.53, No. 3, pp. 588601.

TAMUSWAT (2021). *SWAT: The Soil & Water Assessment Tool.* Available at: https://swat.tamu.edu/ (accessed at 29/07/2021).

Tetsoane, S.T. (2013) *Evaluation of the SWAT Model in Simulating Catchment Hydrology: Case Study of the Modder River Basin, South Africa*. A dissertation, Dept. of Civil Engineering, Central University of Technology, South Africa.

Tracy J.B. - Scott N.M. (2013) *Using the Soil and Water Assessment Tool (SWAT) to assess land use impact on water resources in an East African watershed*. Journal of Hydrology, Vol. 486, No. 2013, pp. 100–111.

UN (2021) *Envision2030: 17 goals to transform the world for persons with disabilities.* Available at: https://www.un.org/development/desa/disabilities/envision2030.html, (accessed at 26/07/2021).

sciendo

Slovak Journal of Civil Engineering

Vol. 30, 2022, No. 1, 68 – 74
DOI: 10.2478/sjce-2022-0008

IMPACT OF CHANGES IN SHORT-TERM RAINFALL ON DESIGN FLOODS: CASE STUDY OF THE HNILEC RIVER BASIN, SLOVAKIA

Gabriel FÖLDES[1], Marija Mihaela LABAT[2*], Silvia KOHNOVÁ[3], Kamila HLAVČOVÁ[3]

Abstract

The research aims to analyze changes in the predicted short-term rainfall intensities at the Telgárt climatological station and the subsequent use of these predicted rainfall intensities for estimating design floods. The area of interest selected is the upper Hnilec River basin in Slovakia. The research is divided into two parts: In the first part, the authors have focused on analyzing future seasonal changes and the trend of short-term rainfall intensities and estimating the scaling exponents of short-term rainfall. In the second part, the observed and predicted short-term rainfall intensities have been applied to estimate the design floods in the study area, using the Soil Conservation Service – Curve Number method (SCS CN). The results indicate that for the future periods, there will be a shift in the rainfall maxima of about one week to an earlier period in July compared to the historical period. The changes in the short-term rainfall trends were detected in the 60-, 120- and 180-minute rainfall durations at the 90% significance level. The results of the design discharges predict higher values in the near future in the case of the 10- and 20-year return periods and higher values in the 50- and 100-year return periods for the remote future.

Address

[1] Board of Tourism, Senec, Slovakia

[2] Dept. of Surface Water Quantity, Slovak Hydrometeorological Institute, Bratislava, Slovakia

[3] Dept. of Land and Water Resources Management, Faculty of Civil Engineering STU in Bratislava, Bratislava, Slovakia

* ***Corresponding author:*** marija.labat@shmu.sk

Key words

- Short-term intensities,
- CLM model,
- Burn's vector,
- Mann-Kendal trend test,
- SCS-CN.

1 INTRODUCTION

In recent decades, increased attention has been paid to global climate change. This is mainly reflected in the increased number of works dealing with changes in the climate and weather. Climate change models are used in many works; the models assume a worsening of the climate that could significantly affect the environment and society (Easterling et al., 2000; Maracchi et al., 2005). The models provide suitable outputs of meteorological variables in space and over time. Climate models are widely used to analyze past events and are also used to predict future weather developments (Tebaldi et al., 2006; Koutsoyiannis et al., 2008).

Serious effects from climate change could also be reflected in the intensity, frequency, and duration (IFD) of future precipitation. From the point of view of society, the intensity, duration and frequency of precipitation are as important as the total amount of precipitation, because these factors determine the disposition of precipitation on the surface and the amount of precipitation that drains in the form of runoff (Trenberth et al., 2003). According to the Intergovernmental Panel on Climate Change (IPCC), the climate is expected to be more unstable or extreme with a very probable increase in the frequency of extreme rainfall. Recent studies have confirmed an increase in short-term rainfall extremes, both in their intensity and in the frequency of rains of less than one day, which could be reflected in the occurrence of flash floods (IPCC, 2013; Lenderink and Attema, 2015; Zope et al., 2016; Soltani et al., 2017). The adaptation to these anticipated changes in short-term rainfall intensities caused by anthropogenic changes in the climate needs to be substantiated by analyses of these changes in short-term rainfall (Wesra et al., 2014). The outputs mostly used for these analyses are from regional climate models, which are compared with observations. Ntegeka and Willems (2008) have shown that extreme precipitation has multi-decadal climate fluctuations. Increases in rain totals have been found both in the winter season as well as in

the summer season. The redistribution of annual rainfall totals into a smaller number of days with a greater intensity associated with an increased risk of floods was also demonstrated in the work of Ban et al. (2015). Occurrences of intense daily and hourly short-term rains with higher intensities and more frequent frequencies were also shown in the areas analyzed in Pascale et al. (2016); the locales ranged from northern Italy to northern Germany. In Denmark, there has also been evidence of an increase in extreme rainfall and a change in the characteristics of rainfall intensities due to climate change (Madsen et al., 2009). A comprehensive understanding of the seasonality of extreme rains is essential in climate studies, flood forecasting, flood risk management etc. (Iliopoulou et al., 2018).

Also in Slovakia, there are many studies dealing with changes in extreme precipitation events, e.g., Faško et al. (2015), Svoboda et al. (2016), Beranová et al. (2018), Markovič et al. (2018), Pecho et al. (2019). However, none of these studies has been focused on developing short-term design rainfalls for the far future based on climate change scenarios in hourly time step, including analysis of changes in trends and seasonality. Derived future design rainfalls were subsequently used for estimation of design floods at ungauged catchment. This approach was tested in the pilot Hnilec River basin, Slovakia.

In this study the seasonal short-term rainfall changes were analyzed using Burn's vector methodology, and the trend analysis of the future was performed with the Mann-Kendall trend test. The future changes were assessed by the predicted short-term rainfall intensities modelled by the Community Land Model (CLM) regional climate scenario. Finally, the design floods were estimated using the empirical SCS-CN hydrological model.

2 METHODOLOGY

2.1 CLM model

The CLM model (CLM, 2005) was developed in a cooperative project between scientists in several divisions at the U.S. National Center for Atmospheric Research (NCAR) and the working group of the Community Earth System Model (CESM). The other main working groups involved in the CLM model are a bio-geochemical group, a paleo-climate group, a climate change group, and the assessor's group (CLM, 2005).

Ecological climatology was implemented in the model, which is used for understanding how natural and anthropogenic changes in vegetation cover affect the climate. It examines the biological, physical and chemical processes affecting terrestrial ecosystems and the climate on different spatial and temporal scales. The central theme is that, through their energy, water, chemicals, and trace gases terrestrial ecosystems are essential determinants of the climate. The CLM components account for surface heterogeneity, bio-geophysics, the hydrological cycle, biogeochemistry, ecosystem dynamics, and the part played by the human dimension (Böhm et al., 2006).The CLM model was used to derive the scenario rainfall data in the hourly time step for the future period till 2100, which were used in this study.

2.2 Seasonality changes in short-term rainfall

Burn´s vector method was selected to reveal changes in seasonality, e.g., the changes in the occurrence of extreme rainfall, and to describe the variability of the dates when extreme rainfall occurs. The expected day of occurrence during a year is given by the direction of the vector. The length of the vector describes the variability around the expected date of the occurrence. Finally, the average position of an event corresponds to the date of the occurrence that is displayed in a unit circle in the polar coordinates (Burn, 1997).

2.3 Changes in trends in short-term rainfall

To assess the statistical significance of any trends, the Mann-Kendall test was used. The purpose of the Mann-Kendall (Mann, 1945; Kendall, 1955) trend test is to statistically assess the significance of an increasing or decreasing trend of a selected quantity over time. The significance of a declining or rising trend depends on a steadily decreasing or increasing variable over time. The test is based on the order of the values and not on the actual value of the elements (Mann, 1945; Kendall, 1955).

2.4 Simple scaling of extreme short-term rainfall

Simple scaling enables us to estimate the design values for a duration shorter than one day for a selected time period by using daily rainfall records that are mostly available (Koutsoyiannis et al., 1993). Simple scaling was applied in this work to downscale rainfall intensities for durations shorter than 1 hour. Focusing on the probability of extreme events, the variable *Id* was introduced, which is the precipitation intensity for the duration *d*, defined as the maximum value of the moving average of a relationship in a given year. The random variable I_d has the following properties (Burlando and Rosso 1996; Menabde et al., 1999; Yu et al., 2004):

$$I_d = \lambda^{\beta} I_{\lambda d}, \tag{1}$$

where the equality is understood in terms of the equality of the probability distributions; β represents the scaling exponent; and λ is the scaling parameter.

λ is a multiplier to convert the duration d to λ_d hours. $I_{\lambda d}$ represents the rainfall intensity for the duration of λ_d hours (Yu et al., 2004). In a similar formulation, $\lambda = D/d$, where d is the duration of the rainfall for a unit of time with a known intensity (most often of one day), and D is the duration of the rainfall for a selected time unit (Menabde et al., 1999).

In this study we have applied the scaling approach of statistical moments. Because we have available rainfall data only of one hour and longer duration, the idea was to use this methodology to derive the IDF curves for lower durations, up to 10min.

2.5 Estimation of a design flood using the SCS-CN methodology

The Soil Conservation Service – Curve Number (SCS – CN) method was used for estimating the design floods. This method is also used for estimating the amount of direct surface runoff for individual rainfall-runoff events and calculating the volume and peak rate of surface runoff (Mishra and Singh, 2003; Fan et al., 2013). It is mainly applicable where direct observations or measurements are limited (as is the case with this research).

The SCS - CN methodology was developed in 1954 by the U.S. Soil Conservation Service (USDA – NRCS, 1954, 1986, 1989, 2004). This empirical method was derived from observations of rainfall and runoff from small agricultural watersheds in various areas of the United States. It is currently adapted to conditions in other parts of the world. Although some researchers have developed various modifications (Soriano et al., 2020), the basic concept behind the method is still widely used. According to Adornado and Yoshida (2010), Moretti and Montanari (2008), Soulis and Valiantzas (2012), and Mishra and Singh (2004), this method has become an inseparable part of many simulation models. Furthermore, the SCS-CN method can be applied to various landscape structures, soils, and climate conditions (Warner et al. 2010; Vojtek and Vojteková 2016; Singh et al., 2015; Tedela et al., 2012; Mishra et al., 2012; Verma et al., 2021). These researchers have also indicated that the SCS-CN method can be effectively used for small and large river basins with heterogeneous land uses.

The SCS - CN method has extended applications, mainly because it is a simple method, which includes many characteristics affecting the generation of direct runoff into a single, dimensionless CN parameter that can easily be determined using the CN table of values (USDA – NRCS, 1989). A more precise description of the application of the SCS-CN methodology in Slovak and Czech Republics see, e.g., in Štefunková et al. (2019), Danáčová et al. (2020), Caletka et al. (2020), Labat et al. (2020, 2021).

3 THE AREA OF INTEREST AND INPUT DATA

The upper part of the Hnilec River basin, with an outlet at the Stratená (ID 8530) water gauge station, was selected in this study. The Hnilec River springs below Kráľová hoľa, the highest peak of the eastern part of the Low Tatras in Slovakia; it is the largest right tributary of the Hornád River. The catchment area of the upper Hnilec River basin has an area of 67.53 km^2 and is located in central Slovakia (Figure 1). The basin´s elevation ranges from 789.13 to 1938.25 m a. s. l., which is 1062.47 m a. s. l. on average. This analysis of the predicted future changes in short-term rainfall was done for the Telgárt climatological station (ID 11938).

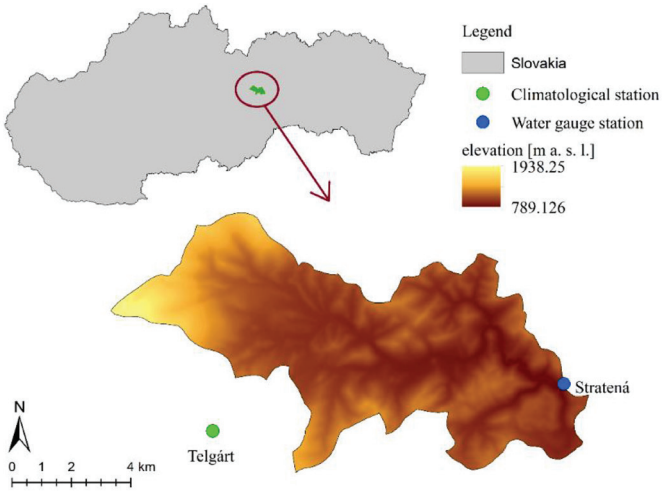

Fig. 1 *Location and Digital Elevation Model (DEM) of the area of interest*

The significant input data in this research were predicted short-term rainfall intensities that are a product of a CLM simulation and the SRES A1B Regional Climate Scenario (RCM). This data was processed by doc. RNDr. Martin Gera, PhD., Comenius University, Bratislava, Slovakia (Lapin, et al., 2012). The period over which we conducted analyses of the short-term rainfall intensities is divided into three time periods: the historical (1960-2000), the near future (2031-2070), and the remote future (2070-2100). The observed rainfall intensities from the Telgárt climatological station from 1995 – 2009 were provided by the Slovak Hydrometeorological Institute (SHMI).

The short-term rainfall intensities from the CLM simulation were used for:

a) an analysis of the seasonal changes (using Burn's vector methodology);
b) the trend testing (using the Mann-Kendall trend test);
c) estimating and comparing the results of the design floods (using the SCS-CN method) in combination with the observed downscaled rainfall intensities.

The observed (1995-2009) and predicted (near future (2031-2070) and remote future (2070-2100)) design short-term rainfall intensities for the Telgárt climatological station (downscaled by the authors) are shown in Fig 2.

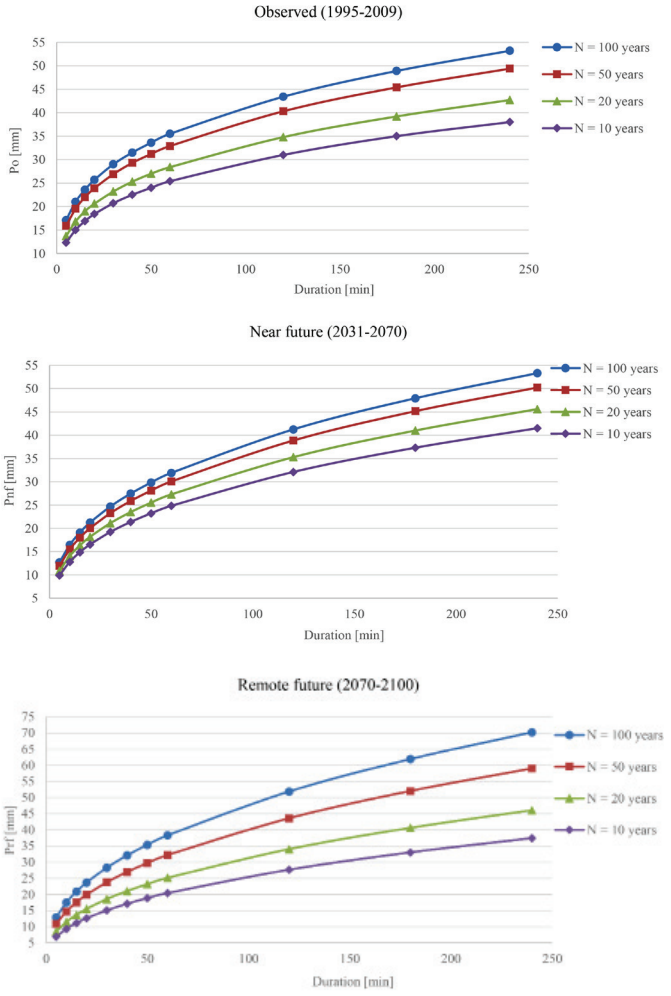

Fig. 2 *The observed (P_o), near (P_{nf}) and remote future (P_{rf}) designs of the short-term rainfall intensities for the Telgárt climatological station*

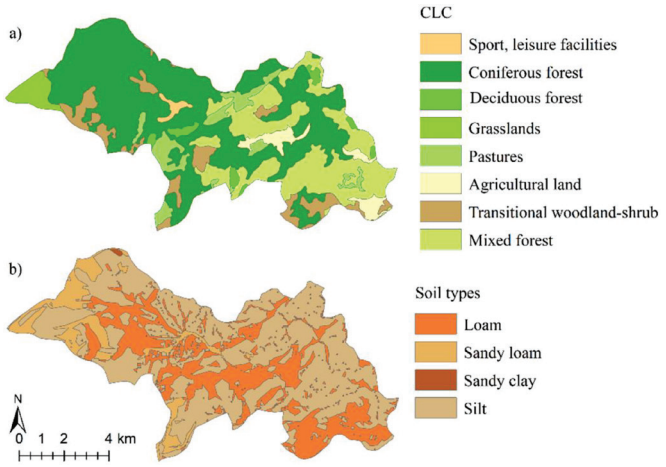

Fig. 3 Digital vector maps: a) CLC land use, b) soil types

To estimate the design floods, the following digital maps were used and processed in a GIS environment: a Digital Elevation Model (DEM), with a 20 m raster size (Fig. 1); a Corine Land Cover (CLC) land use vector map for the year 2018 (Fig. 3a) that is available online (Copernicus Land Monitoring Service); a soil type vector map (Fig. 3b); and an orthophoto map, with a 25 cm raster size (ZBGIS®).

4 RESULTS

4.1 Changes in the seasonality of the short-term rainfall

One of the aims of this analysis was to look at the shifts in the occurrence of the seasonal extremes in the short-term rainfall for the periods analyzed and compare what changes in seasonality could occur for both future periods. The periods analyzed were the historical (1961-2020), the near future (2031-2070), and the remote future (2071-2100) periods. The results from the seasonality analysis are in Figure 4.

The results show that the seasonal extremes in the short-term rainfall intensities occur in July. It can, therefore be assumed that there could be a minimal change between the two future periods. The most significant change predicted between the future periods will be the daily rainfall duration. The remote-future period shows a one-week shift to an earlier period in July. The comparison of the historical and future periods shows a minimal change, and the difference between the occurrence of the seasonal extremes is approximately one week.

4.2 Changes in the trends of the short-term rainfall

An analysis of short-term rainfall trends was undertaken too. The results from the trend analysis are available in Table 1.

Tab. 1 *The trends in the short-term rainfall intensities data*

Duration (min) / Period (year)	60	120	180	240	1440
1961-2020	↘	↘	↘	↘	↘
2031-2070	↗	↗	↗	↗	↗
2071-2100	↘	↘	↘	↘	↘

The study showed interesting results. There are decreasing but not significant trends in the historical and remote-future periods. A different situation can be seen in the near future period, where an increase was revealed in all the rainfall durations. In the 60-, 120-, and 180-minute durations, significant trends were detected at a 90% level of significance.

4.3 Estimation of the design floods using the SCS – CN method

Finally, the design floods (Q_N) were estimated using the SCS – CN method and the downscaled observed, near future and remote future design rainfall intensities (Fig. 2). The calculations were provided for different return periods (N = 10, 20, 50, and 100 years). The hydrological soil group (needed to estimate the CN parameter) was derived using the map of soil types (Fig. 3b), according to which hydraulic soil group B was selected. Subsequently, the CLC land use map for 2018 (Fig. 3a) was used to set the CN values shown in Table 2.

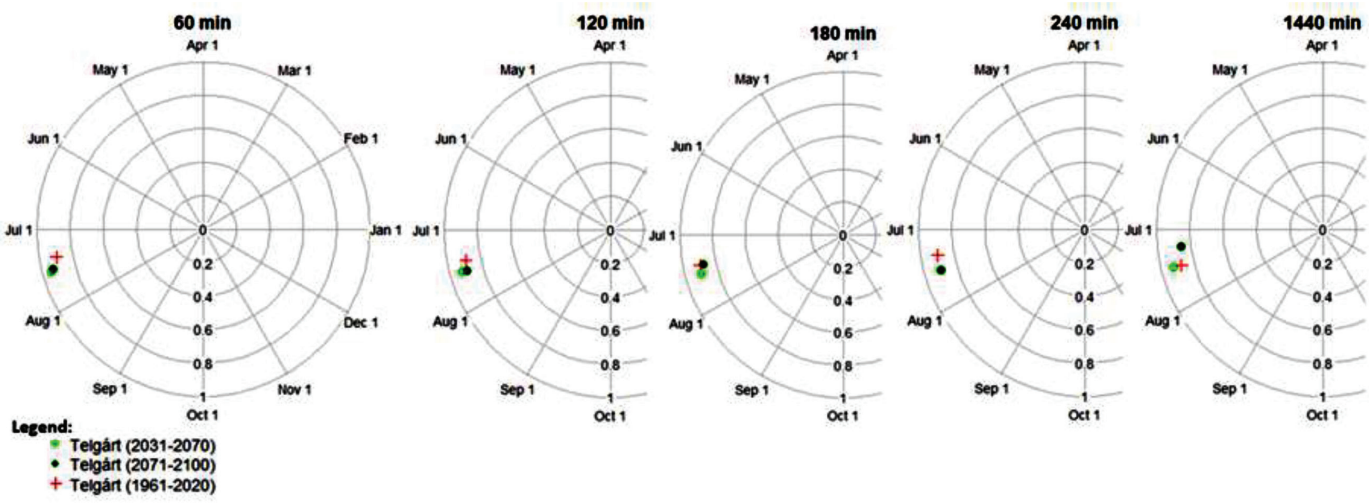

Fig. 4 The shifts in seasonality of the extreme short-term rainfall

Tab. 2 *Selected CN values used for the Hnilec River basin*

Land use	Area [km^2]	CN [-]
Sport and leisure facilities	0.52	69
Coniferous forest	36.23	60
Broad-leaved forest	1.29	60
Grasslands	1.86	58
Pastures	4.02	69
Agricultural land	2.37	72
Transitional woodland-shrub	5.56	67
Mixed forest	15.67	60
total area [km^2]	67.53	
weighted average CN value [-]		**61.55**

The research assumed that the whole analyzed area of the Hnilec River basin would be affected by precipitation: 1) with a duration equal to the time of the concentration (Pasák, 1983)), which, in the case of the Hlinec River basin, is equal to 104 min; 2) with the same statistical significance as the design flood. The values of the estimated design flood values (Q_N) using the observed (P_o), the near future (P_{nf}), and remote future (P_{rf}) design rainfall intensities are shown in Table 3.

Compared to the Q_{Na}, the results from Table 3 show that the values of the Q_{Nnf} in the near future increased in the cases of the 10- and 20-year return periods. The opposite is valid for the remote-future design floods, where Q_{Nrf} increased by 32% in the case of the 100-year return period when compared to the Q_{Na}.

5 CONCLUSIONS AND DISSCUSION

This study focused on detecting trends and changes in short-term rainfall and their influence on design floods in the selected river basin. The Mann-Kendall trend test method was used in this analysis. Historical periods (1961-2020), near-future periods (2031-2070) and distant future (2071-2100), and for 60-, 120-, 180-, 240- and 1440-minute rain durations were tested. The results are summarized in Table 1. Significant upward trends of 90 % significant were detected for the near future (2031-2070). This trend is similar to other Slovak stations such as Bratislava-Koliba, Červený Kláštor, Boľkovce, Hurbanovo, Lipovce, Liesek, Ľubochňa, Smolník and Tatranská Lomnica. The next step was to analyze the seasonality of occurrences of maximum rainfalls during the warm half-year. The Burn vector method was used, and future average shifts of short-term rainfall rates since the historical period (1961-2020) were also determined. On average, the predominant shift between historical and future periods was one week earlier in July. From a regional point of view, similar shifts to the earlier period were detected at other stations in the High and Low Tatra Regions of Slovakia.

Regarding the derivation of short-term design rainfalls, it can be concluded from the results of the period-to-period comparison that the design values of the short-term rain intensities derived from the CLM scenario for future periods are higher, Fig.2.

The changes in short term rainfall will have an impact on design flood estimation, as was detected in this case study.

The main results from the study can be summarized as follows:

1. The changes in seasonality in the short-term rainfall with durations of 60 min to one day predicted for the future periods are insignificant. But it can be noted that for the future periods, there will be a shift in the rainfall maxima of about one week to an earlier period in July compared to the historical period;
2. The changes in the short-term rainfall trends showed an insignificant decreasing trend for the historical and remote future periods. However, for the near future period, significant trends were detected in the 60-, 120- and 180-minute rainfall durations at the 90% significance level;
3. The results of the design discharges predict higher values in the near future in the case of lower 10- and 20-year return periods, and the increase for the 50- and 100-year return periods will be in the far future. These results could signal more extreme floods in the future in this area and the need for re-evaluating flood protection.

Finally, all the results presented can be helpful for future water management planning and flood protection measures in the study area.

Acknowledgement

This study is a part of the "Scientific support of climate change adaptation in agriculture and mitigation of soil degradation" (ITMS2014+ 313011W580) project, supported by the Integrated Infrastructure Operational Programme funded by the European Regional Development Fund (ERDF). This work was also supported by the Slovak Research and Development Agencies under Contract No. APVV-19-0340, and the VEGA Grant Agency Nos. 1/0782/21 and 1/0632/19. The authors are thankful for their support.

Tab. 3 *Estimated design floods using the observed (P_o), the near future (P_{nf}), and the remote future (P_{rf}) design rainfall intensities*

N [years]	P_o (1995-2009) [mm]	Q_{No} [m^3.s^{-1}]	P_{nf} (2031-2070) [mm]	Q_{Nnf} [m^3.s^{-1}]	P_{ff} (2071-2100) [mm]	Q_{Nrf} [m^3.s^{-1}]
10	29.7	33.87	30.5	35.38	26.0	26.37
20	33.4	41.95	33.5	42.05	32.0	38.68
50	38.7	54.71	36.9	50.13	41.0	60.61
100	41.7	62.53	39.1	55.84	48.7	82.59

REFERENCES

Adornado, H. A. - Yoshida, M. (2010) *GIS-based watershed analysis and surface run-off estimation using curve number (CN) value*. J. Environ. Hydrol, 2010, Vol. 18, pp. 1–10.

Ban, N. - Schmidli, J. - Schär, Ch. (2015) *Heavy precipitation in a changing climate: Does short-term summer precipitation increase faster?* Geophysical Research Letters [online]. Vol. 42, no. 4, pp. 1165–1172 ISSN 00948276. doi:10.1002/2014GL062588

Beranová, R. - Kyselý, J. - Hanel, M. (2018) *Characteristics of sub-daily precipitation extremes in observed data and regional climate model simulations.* Theoretical and Applied Climatology, Vol. 132, No. 1–2, pp. 515–527. ISSN 14344483. doi:10.1007/s00704-017-2102-0

Böhm, U. - Kücken, M. - Ahrens, W. - Block, A. - Hauffe, D. - Keuler, K. Rockel, B. Will, A. (2006) *CLM - The climate version of LM: brief description and long-term applications*, COSMO Newsletter, No. 6, pp. 225–235.

Burlando, P. - Rosso, R. (1996) *Scaling and muliscaling models of depth-duration-frequency curves for storm precipitation*. Journal of Hydrology. Vol. 187, no. 1, pp. 45–64.

Burn, D. H. (1997) "*Catchment similarity for regional flood frequency analysis using seasonality measures*," J. Hydrol., Vol. 202, pp. 212–230.

Caletka, M. - Michalková, M. - Karásek, P. - Fučík, P. (2020) *Improvement of SCS-CN Initial Abstraction Coefficient in the Czech Republic: A Study of Five Catchments*. Water. 12. pp. 1-28. 10.3390/w12071964.

CLM - Community Land Model (© 2005), *Overview*, NCAR Earth System Laboratory (NESL) a collaborative project between TSS and the CESM community, © 2005, UCAR, P.O. Box 3000, Boulder, CO, USA. Available from: http://www.cgd.ucar.edu/tss/clm, [accessed 13 Jan. 2022].

Copernicus Land Monitoring Service, *CORINE Land Cover, Copernicus Programme*, Available from: https://land.copernicus.eu/pan-european/corine-land-cover [accessed 13 Jan. 2020].

Danáčová, M., Földes, G., Labat, M. M., Kohnová, S., Hlavčová, K. (2020) *Estimating the Effect of Deforestation on Runoff in Small Mountainous Basins in Slovakia*, Water, Vol. 12, 3113, 2020.

Easterling, D. R. - Meehl, G. A. - Parmesan, C. - Changnon, S. A. - Karl, T. R. - Mearns, L. O. (2000) *Climate extremes: Observations, modeling, and impacts*, American Association for the Advancement of Science. doi:10.1126/science.289.5487.2068

Fan, F. - Deng Y. - Hu, X. - Weng, Q. (2013) *Estimating composite curve number using an improved SCS-CN method with remotely sensed variables in Guangzhou, China*, Remote Sensing, Vol. 5, No. 3, pp. 1425–1438.

Faško, P. - Šťastný, P. - Švec, M. - Kajaba, P. (2015) Occurrence and spatial distribution of high daily and multi-day precipitation totals in Slovakia. (in Slovak)

Iliopoulou, T. - Koutsoyiannis D. - Montanari, A. (2018) *Characterizing and Modeling Seasonality in Extreme Rainfall.* Water Resources Research 2018, Vol. 54, 9, pp. 6242–6258. ISSN 00431397. Doi: 10.1029/2018WR023360

IPCC (2013) (Intergovernmental Panel on Climate Change) "*Climate Change 2013: The Physical Science Basis. Contribution of Working Group I to the Fifth Assessment Report of the Intergovernmental Panel on Climate Change*," [online]. Cambridge University Press, Cambridge, UK, and New York, NY, USA.

Kendall, M. G. (1955) "*Rank correlation methods*," Griffin, London, UK.

Koutsoyiannis, D. - Efstratiadis, A. - Mamassis, N. - Christofides, A., (2008) *On the credibility of climate predictions*. Hydrological Sciences Journal, Vol. 53, 4, pp. 671–684. ISSN 2150-3435. doi:10.1623/hysj.53.4.671

Labat, M. M. - Aleksić, M. - Hlavčová, K. - Földes, G. (2021) *Impact of resolution of DEM on the calculation of design floods in a small mountainous basin*, IOP Conference Series: Earth and Environmental Science, Vol. 609. No. 1. IOP Publishing, 012060.

Labat, M. M. - Földes, G. - Kohnová, S. - Hlavčová, K. (2020) *Land use and climate change impact on runoff in a small mountainous catchment in Slovakia*, IOP Conference Series: Earth and Environmental Science.

Lapin, M. - Bašták-Ďurán, I. - Gera, M. - Hrvoľ, J. - Kremler, M. - Melo, M (2012) *New climate change scenarios for Slovakia based on global and regional general circulation models*, Acta Met. Univ. Comenius. Vol. 37, pp. 25–74, 2012.

Lenderink, G. - Attema, J. (2015) *A simple scaling approach to produce climate scenarios of local precipitation extremes for the Netherlands*. Environmental Research Letters Vol. 10, 8, p. 085001 ISSN 1748-9326. doi:10.1088/1748-9326/10/8/085001

Madsen, H. - Arnbjerg-Nielsen, K. - Mikkelsen, P. S. (2009) *Update of regional intensity-duration-frequency curves in Denmark: Tendency towards increased storm intensities*. Atmospheric Research, Vol. 92, no. 3, pp. 343–349. ISSN 01698095. doi:10.1016/j.atmosres.2009.01.013

Mann, H. B. (1945) *Nonparametric tests against trend*, Econometrica, Vol. 13, No. 3, pp. 245–259.

Maracchi, G. - Sirotenko, O. - Bindi, M. (2005) *Impacts of present and future climate variability on agriculture and forestry in the temperate regions: Europe*, Climatic Change. B.m.: Springer, pp. 117–135. doi:10.1007/s10584-005-5939-7

Markovič, L. - Faško, P. - Bochníček, O. (2018) *Maximum amounts of 2- and 5-day total atmospheric precipitation in Slovakia in the period 1951-2010.* Acta Hydrologica Slovaca. Vol. 19, No. 1, pp. 3–10.

Menabde, M. - Seed, A. - Pegram, G. (1999) *A simple scaling model for extreme rainfall* [online]. [cit. 11. máj 2019]. Dostupné na: doi:10.1029/1998WR900012.

Mishra, S. K. - Singh, V. P. (2003) *SCS-CN Method, Soil Conservation Service Curve Number (SCS-CN) Methodology*, Springer Science and Business Media LLC, Dordrecht, pp. 84–146.

Mishra, S. K. - Singh, V. P. (2004) *Long-term hydrological simulation based on the Soil Conservation Service curve number.* Hydrological Processes, Vol. 18, No. 7, pp. 1291–1313.

Mishra, S. K. - Pandey, A. - Singh, V. P. (2012) *Special Issue on Soil Conservation Service Curve Number (SCS-CN) Methodology*. Journal of Hydrologic Engineering, Vol. 17, No. 11, pp. 1157–1157.

Moretti, G. - Montanari, A. (2008) *Inferring the flood frequency distribution for an ungauged basin using a spatially distributed rainfall-runoff model*. Hydrology and Earth System Sciences Vol. 12, No. 4, pp. 1141–1152.

Ntegeka, V. - Willems, P. (2008) *Trends and multidecadal oscillations in rainfall extremes, based on a more than 100-year time series of 10 min rainfall intensities at Uccle, Belgium*. Water Resources Research [online]. Vol. 44, No. 7, ISSN 00431397. doi:10.1029/2007WR006471.

Pasák, V. - Janeček, M. - Šabata, M. (1983) *Protection of agricultural soil against erosion, Methodologies for introducing research results into agricultural practice* (in Czech: Ochrana zemědelské půdy před erozí. Metodiky pro zavádění výsledků výzkumu do zemědelské praxe), Institute of Scientific and Technical Information for Agriculture, Prague, CZ.

Pascale, S. - Lucarini, V. - Feng, X. - Porporato, A. - Ul Hasson, S. (2016) *Projected changes of rainfall seasonality and dry spells in a high greenhouse gas emissions scenario.* Climate Dynamics, Vol. 46, Nos. 3–4, pp. 1331–1350. ISSN 0930-7575. doi:10.1007/s00382-015-2648-4

Pecho, J. - Markovič, L. - Faško, P. - Bochníček, O. (2019) *Spatial and temporal variability and changes in maximum 2-days precipitation totals in Slovakia over the period 1951-2017.* Geophysical Research Abstract. Vol. 21, p. 1

Singh, P. K. - Mishra, S. K. - Berndtsson, R. - Jain M. K. - Pandey, R. P. (2015) *Development of a Modified SMA Based MSCS-CN Model for Runoff Estimation*. Water Resources Management Vol. 29, No. 11, pp. 4111–4127.

Soltani, S. - Helfi, R. - Almasi, P. - Modarres, R. (2017) *Regionalization of Rainfall Intensity-Duration-Frequency using a Simple Scaling Model.* Water Resources Management. Vol. 31, No. 13, pp. 4253–4273. ISSN 0920-4741. doi:10.1007/s11269-017-1744-0

Soriano, E. - Mediero, L. - Garijo, C. (2020) *Quantification of Expected Changes in Peak Flow Quantiles in Climate Change by Combining Continuous Hydrological Modelling with the Modified Curve Number Method*. Water Resources Management, Vol. 34, No.14, pp. 4381–4397.

Soulis, K. X. - Valiantzas, J. D. (2012) *SCS-CN parameter determination using rainfall-runoff data in heterogeneous watersheds-the two-CN system approach.* Hydrology and Earth System Sciences Vol. 16, No. 3, pp. 1001–1015.

Svoboda, V. - Hanel, M. - Máca, P. - Kyselý, J. (2016) *Projected changes of rainfall event characteristics for the Czech Republic.* J. Hydrol. Hydromech. Vol. 64, No. 4, pp. 415–425.

Štefunková, Z. - Hlavčová, K. - Labat, M. M. (2019) *Assessment of the Impact of Changes in Deforestation under the Effect of Severe Windstorms on Runoff Conditions in Small River Basins*, Slovak Journal of Civil Engineering, Vol. 27, No. 3, pp. 37–43, 2019.

Tebaldi, C. - Hayhoe, K. - Arblaster, J. M. - Meehl, G. A. (2006) *Going to the extremes: An intercomparison of model-simulated historical and future changes in extreme events*, Springer, The Netherlands. doi:10.1007/s10584-006-9051-4

Tedela, N. H. - Mccutcheon, S. C. - Rasmussen, T. C. - Hawkins, R. H. - Swank, W. T. - Campbell, J. L. - Adams, M. B. - Jackson, C. R. - Tollner, E. W. (2012) *Runoff Curve Numbers for 10 Small Forested Watersheds in the Mountains of the Eastern United States*. Journal of Hydrologic Engineering, Vol. 17, No. 11, pp. 1188–1198.

Trenberth, K. - Dai, E. A. - RASMUSSEN, R. M. - PARSONS, D. B. (2003) *The changing character of precipitation* [online], Sep. 2003. doi:10.1175/BAMS-84-9-1205

USDA–NRCS (1954) *Estimation of Direct Runoff from Storm Rainfall*, National Engineering Handbook, Part 630 – Hydrology, U. S. Dept. of Agriculture - Soil Conservation Service, Washington, DC.

USDA–NRCS (1986) *Urban Hydrology for Small Watersheds, Technical Release 55* [online]. U. S. Dept. of Agriculture - Natural Resources Conservation Service, Engineering Division, Washington, DC, 164 pp.

USDA–NRCS (1989) *Engineering Hydrology Training Series. Module 104 - Runoff Curve Number Computations, Study Guide*. 2, U. S. Dept. of Agriculture - Soil Conservation Service, Washington, DC.

USDA–NRCS (2004) *Estimation of Direct Runoff from Storm Rainfall*, National Engineering Handbook, Part 630 – Hydrology, U. S. Dept. of Agriculture - Natural Resources Conservation Service, Washington, DC, pp. 10-1 – 10-22.

Verma, R. K. - Verma, S. - Sharma, N. K. - Mishra, S. K. - Pandey, A. (2021) *Improved SCS-CN Model Incorporating Storm Duration and Rainfall-based Initial Abstraction for Runoff Estimation*. Preprints 2021, 2021040352

Vojtek, M., Vojteková, J. (2016) *GIS-based Approach to Estimate Surface Runoff in Small Catchments: A Case Study*. Quaestiones Geographicae, Vol. 35, No. 3, pp. 97–116.

Warner, R. C. - Agouridis, C. T. - Vingralek, P. T. - Fogle, A. W. (2010) *Reclaimed Mineland Curve Number Response to Temporal Distribution of Rainfall*. JAWRA Journal of the American Water Resources Association, Vol. 46, No. 4, pp. 724–732.

Yu, P. S.H - Yang, T. CH. - Lin, CH.-SH. (2004) *Regional rainfall intensity formulas based on scaling property of rainfall*. Journal of Hydrology, Vol. 295, Nos. 1–4, pp. 108–123.

ZBGIS®, The Geodesy, Cartography and Cadaster Institute, *Map Client*, Authority of the Slovak Republic, Geodetic and Cartographic Institute Bratislava [online], [accessed 17 Feb. 2020].

Zope, P. E. - Eldho T. I. - Jothiprakash, V. (2016) *Development of Rainfall Intensity Duration Frequency Curves for Mumbai City, India.* Journal of Water Resource and Protection, Vol. 08, No. 07, pp. 756–765. ISSN 1945-3094. doi:10.4236/jwarp.2016.87061